WIFFEN

DOE/ET-0058/2

Welds p.47
INCO 600 p.62

Alloy Development for Irradiation Performance

Quarterly Progress Report

APRIL-JUNE 78 ~~January-March 1979~~

May 1979

U.S. Department of Energy
Assistant Secretary for Energy Technology
Office of Fusion Energy

DOE/ET-0058/2
uc-20. 20c

Alloy Development for Irradiation Performance

Quarterly Progress Report
January-March, 1978

May 1979

U.S. Department of Energy
Assistant Secretary for Energy Technology
Office of Fusion Energy
Washington, DC 20545

Available from:

National Technical Information Service (NTIS)
U.S. Department of Commerce
5285 Port Royal Road
Springfield, Virginia 22161

Price: Printed Copy: $ 3.00
Microfiche: $ 3.00

FOREWORD

This report is the second in a series of Quarterly Technical Progress Reports on *Alloy Development* for *Irradiation Performance* (ADIP), which is one element of the Fusion Reactor Materials Program, conducted in support of the Magnetic Fusion Energy Program of the U.S. Department of Energy. Other elements of Materials Program are:

- *Damage Analysis and Fundamental Studies (DAFS)*
- *Plasma-Muterials Interaction (PMI)*
- *Special-Purpose Materials (SPM)*

The ADIP program element is a national effort composed of contributions from a number of national laboratories and other government laboratories, universities, and industrial laboratories. It was organized by the Materials and Radiation Effects Branch, Office of Fusion Energy, DOE, and a Task Group on *Alloy Development* for *Irradiation Performance,* which operates under the auspices of that branch. The purpose of this series of reports is to provide a working technical record of that effort for the use of the program participants, for the fusion energy program in general, and for the Department of Energy.

This report is organized along topical lines in parallel to a Program Plan of the same title (to be published) *so* that activities and accomplishments may be followed readily relative to that Program Plan. Thus, the work of a given laboratory may appear throughout the report. Chapters 1, **2**, 7, and 8 review activities on analysis and evaluation, test methods development, status of irradiation experiments, and corrosion testing and hydrogen permeation studies, respectively. These activities relate to each of the alloy development paths. Chapters **3**, *4*, *5*, and *6* present the ongoing work on each alloy development path. The Table of Contents is annotated for the convenience of the reader.

This report has been compiled and edited under the guidance of the Chairman of the Task Group on *Alloy Development* for *Irradiation Performance*, *E. E. Bloom,* Oak Ridge National Laboratory, and his efforts, those of the supporting staff of ORNL and the many persons who made technical contributions are gratefully acknowledged. T. C. Reuther, Materials and Radiation Effects Branch, is the Department of Energy counterpart to the Task Group Chairman and has responsibility for the ADIP Program within DOE.

Klaus M. Zwilsky, Chief
Materials and Radiations Effects Branch
Office of Fusion Energy

HIGHLIGHTS

An important consideration in the use of mixed-spectrum fission reactors in the development of alloys for use in fusion reactors is the ability to reproduce the helium-to-displacement production ratio of a fusion reactor in alloys that contain nickel. This is accomplished by a two-step reaction of thermal neutrons with ^{58}Ni giving ^{56}Fe and an α particle. Since the number of atomic displacements (dpa) is proportional to the fast fluence and the helium content is proportional to the thermal fluence raised to about the 1.7 power, the He/dpa ratio matches a fusion reactor at only one time. This difficulty can be overcome by adjusting the fast and thermal neutron fluxes in the irradiation experiment (i.e., spectral tailoring). Calculations were performed to determine the relative changes in thermal and fast neutron flux needed to obtain the He/dpa ratio of a fusion spectrum. Three-dimensional neutron diffusion calculations of the ORR core show that the spectral changes required in the early portion of the experiment are easily obtained.

Fatigue crack growth is an important material property for any fusion reactor that operates cyclically. The effects of irradiation on crack growth have in the past been determined only in postirradiation tests. However, differences may exist between behavior exhibited during and after irradiation. Space, heating, and load limitations prevent the use of standard fatigue crack growth specimens for in-reactor measurements. Miniature specimens are presently being developed. The results to date have indicated that this specimen design (1) produces fatigue crack growth rate data that are in excellent agreement with results for larger, nonwelded designs and (2) is suited for both in-reactor and postirradiation testing.

Swelling and postirradiation tensile properties of Inconel 600 have been determined as a function of temperature at damage levels of 4 to 9 dpa and 600 to 1800 at. ppm He. Swelling was weakly dependent on temperature below 600°C, increased rapidly above 600°C, and was much higher than expected from fast reactor or ion irradiations. Swelling was similar for cold-worked

and annealed structures. Fractures were transgranular at 300 and 400°C and intergranular at 600 and 700°C. As concerns swelling and tensile properties, Inconel 600 has no advantage over type 316 stainless steel.

A large data base has been compiled on niobium alloys; however, the data base for any one alloy is limited. While a large amount of data exist on creep and creep rupture, most of the data are at higher temperatures and shorter times than those required for fusion devices. Data on fatigue behavior are meager, primarily because past applications were limited by creep and/or oxidation. It was found, however, that no part of the existing data base shows that niobium base alloys are deficient for fusion applications.

Corrosion of type 316 stainless steel in lithium has been measured at 600°C for times to 5000 h. The rate decreased with time and at 5000 h was equivalent to about 22 μm/year (0.9 mil/year). Capsule tests indicate that this rate could be further reduced by additions to the lithium of aluminum or silicon, which form continuous reaction layers on the stainless steel surface. Corrosion of type 316 stainless steel by lithium at temperatures below 600°C does not appear to be a major problem.

CONTENTS

1. ANALYSIS AND EVALUATION STUDIES

The designs for power-producing fusion reactors are in a very embryonic and rapidly changing state. Requirements for materials performance are thus not well defined. However, regardless of the final designs, the environment will clearly be extremely demanding on materials in regions of high neutron flux. One cannot identify a class of alloys on which the development efforts should focus — thus the parallel paths of the Alloy Development Program. The combination of reactor designs that are evolving and the necessity for including alloys with widely different physical, chemical, and mechanical properties in the program could lead to an impossibly large number of potential problems and possible solutions. Analysis and evalution studies are an essential part of the Alloy Development Program in order to translate fusion reactor performance goals into material property requirements and to identify crucial and generic problems on which development activities should be focused. As the Alloy Development Program proceeds and a better understanding of the behavior of materials in potential fusion reactor environments is attained, these studies will also identify problems that will necessitate design solutions.

1.1 RESIDUAL RADIOACTIVITY OF SEVERAL COMMERCIAL TITANIUM ALLOYS -

J. W. Davis (McDonnell Douglas), G. L. Kulcinski (University of Wisconsin), and T. Y. Sung (EBASCO).

1.1.1 ADIP Task

Task Number I.A.l.l - Select initial representative designs, obtain property data, establish analysis procedures, and complete initial analyses.

1.1.2 Objective

To examine and compare residual radioactivity of several titanium alloys and determine which compositions offer potential for reprocessing.

1.1.3 Summary

This study examines the impact of small amounts of alloying elements on the reuse potential of titanium. The results of this study reveals that the use of molybdenum, even in concentrations as low as 0.8 w/o, makes the radioactivity in titanium comparable to the long term radioactivity in 316 SS and therefore complicates the reprocessing of titanium alloys. A possible alternate would be tin which can also enhance creep strength. Aluminum has much the same effect as molybdenum on the long term radioactivity, however, the level of radioactivity is 10^3 times lower. Therefore aluminum containing alloys could be reprocessed with modest shielding but the aluminum content should be kept at 1-2 w/o. Even though none of the current high strength titanium alloys fulfill the goal of low long term radioactivity, there are some alloys such as Ti-6Al-4V and Ti-15-3 that are close. Based on strength and radioactivity, an attractive titanium alloy composition could be Ti-(1-2) w/o Al-(10-14) w/o Sn-(0.1-0.3) w/o Si.

1.1.4 Progress and Status

One of the major advantages of titanium is its short lived radioactivity, biological hazard potential (BHP), and afterheat. However, it is rarely the case that a pure element can be used for a structural material and most often, an alloy is required. The basic question then

arises - how do the common alloying elements of titanium affect its desireable short term radioactivity? In the study reported in the last quarterly, the radioactivity of the titanium alloying elements Si, Al, V, Cr, Mo, Zr, Mn, and Sn were examined to answer this question.(1) The results of this study showed that if titanium is to be capable of being reprocessed in < 50 years then it should be alloyed with any of the following elements: (listed in order of increasing desireability) Mn, Cr, V, Sn, and Si. With the exception of Ti-8Mn, there does appear to be commercial or developmental alloy composed solely of these elements. There are some alloys that are close to an "ideal" composition from a radioactivity standpoint but the majority of them rely on the addition of aluminum or zirconium for strength and phase stability both of which tend to increase radioactivity. Therefore, it is instructive to see how the addition of these two elements will impact the overall radioactivity since their concentrations are usually < 6 w/o in the alloys. To accomplish this 4 developmental/commercial alloys were selected for evaluations and the results compared to Ti-6Al-4V which has been previously studied.(2) The alloys selected along with their compositions are presented in Table 1.1.1. The Ti-8Mn alloy is a medium strength alloy that was developed in the mid-1950's and is used on the F-4 series of aircraft. It was developed for applications in the 100-300°C temperature range. However, because of a tendency towards stress corrosion cracking and a susceptibility to embrittlement from a Ti-Mn intermetallic compound, the alloy has gradually been replaced by the Ti-6Al-4V alloy. The Ti-6Al-4V, Ti-6242S, and Ti-5621s alloys are currently included in the ADIP path C scoping studies and the rationale for their selection and their potential for fusion reactor applications has been presented elsewhere.(3) The Ti-15-3 alloy also is described in Reference 3 and is included in a recent EBR-II irradiation creep experiment.(4)

The radioactivity of the various titanium alloys was determined by using the blanket model described in Reference (2) along with the cylindrical calculations (P_3S_8) and the computer codes developed by Sung.(5) The same procedure was used to calculate the radioactivity of the other candidate structural materials shown in Figure 1.1.1. These a calculations are based on a reactor with a thermal power level of 5000 MW and a neutron wall loading of 1.25 MW/m^2.

Table 1.1.1 Composition of Titanium Alloys Used in Radioactivity Study

Ti-8Mn	α + 0	Ti-8Mn	Ti-7Hn
Ti-6-4	α + β	Ti-6Al-4V	Ti-10.2Al-3.6V
Ti-6242s	α	Ti-6Al-2Sn-4Zr-2Mo-0.09Si	Ti-10.6Al-0.8Sn-2.1Zr-0.99Mo-0.15Si
Ti-5621S	α	Ti-5Al-6Sn-2Zr-0.8Mo-0.25Si	Ti-9Al-2.5Sn-1.1Zr-0.4Mo-0.43Si
Ti-15-3	β	Ti-15V-3Cr-3Sn-3Al	Ti-14.2V-2.7Cr-1.2Sn-5.4Al

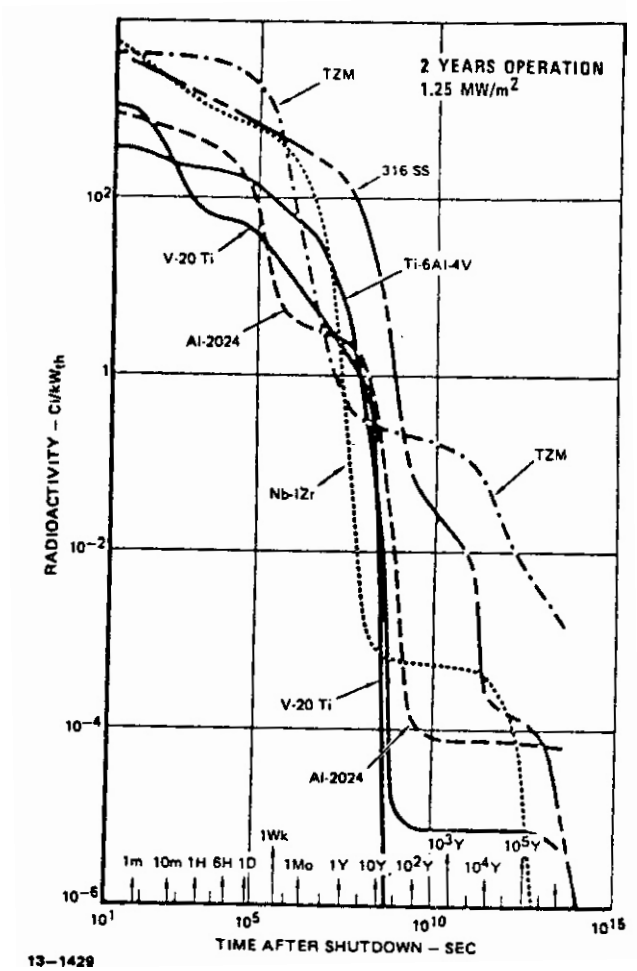

Figure 1.1.1 Radioactivity of Several Candidate fusion reactor Structural Material

The radioactivity of the titanium alloy Ti-6Al-4V in comparison to the other structural materials is shown in Figure **1.1.1.** This figure shows that the radioactivity of the titanium alloy is essentially about the same as the 2024 aluminum alloy and the V-20Ti vanadium alloy for a short time after shutdown. For intermediate times (roughly 5 to 30 years) the radioactivity is essentially the same as the vanadium alloys. However, after about 50 years there is essentially a leveling off of the decay rate and further decreases in radioactivity are essentially controlled by the Al^{26} isotope. A comparison of Ti-6Al-4V with the other titanium alloys is shown in Figure 1.1.2. This figure shows that alloys that contain molybdenum drop by a factor of 10^5 within 10 years after shutdown but then remain at that level for several thousand years. In addition there does not appear to be any significant difference (less than a factor of 2) in the long term radioactivity between Ti-6242s which contains 2 w/o molybdenum and Ti-5621s which contains 0.8 w/o molybdenum.

The isotopes that are responsible for the residual activity are graphically displayed in Figure 1.1.3 for the Ti-6242s alloy. This figure reveals that approximately 75% of the activity of this alloy decays in the first month after shutdown. This leaves Sc^{46} to dominate the activity for the next few years. After that period, the Mo^{93} isotope and its daughter product, Nb^{93m}, control the activity for the next 10,000 years. Finally the Tc^{99} and the Al^{26} isotopes dominate the activity out to a million years or so.

The difference in radioactivity between molybdenum containing alloys and those that do not, can also be seen in Figure 1.1.2. This figure shows that for the alloys that do not contain molybdenum, (Ti-6Al-4V, Ti-15-3, and Ti-8Mn) the induced activities are about the same as those that contain molybdenum for the first year of decay. After the first year the radioactivity rapidly drops for all the alloys; however, for the alloys without molybdenum the radioactivity is well below the molybdenum containing alloys. For the alloys that contain aluminum (Ti-6Al-4V and Ti-15-3) the activity is reduced by a factor of 10^8 in 30 years which is a factor of 10^3 below Ti-62425 and Ti-5621s. Beyond this period the radioactive decay levels out as a result of the Al^{26} ($t_{\frac{1}{2}} \approx$ 700,000 years) isotope.

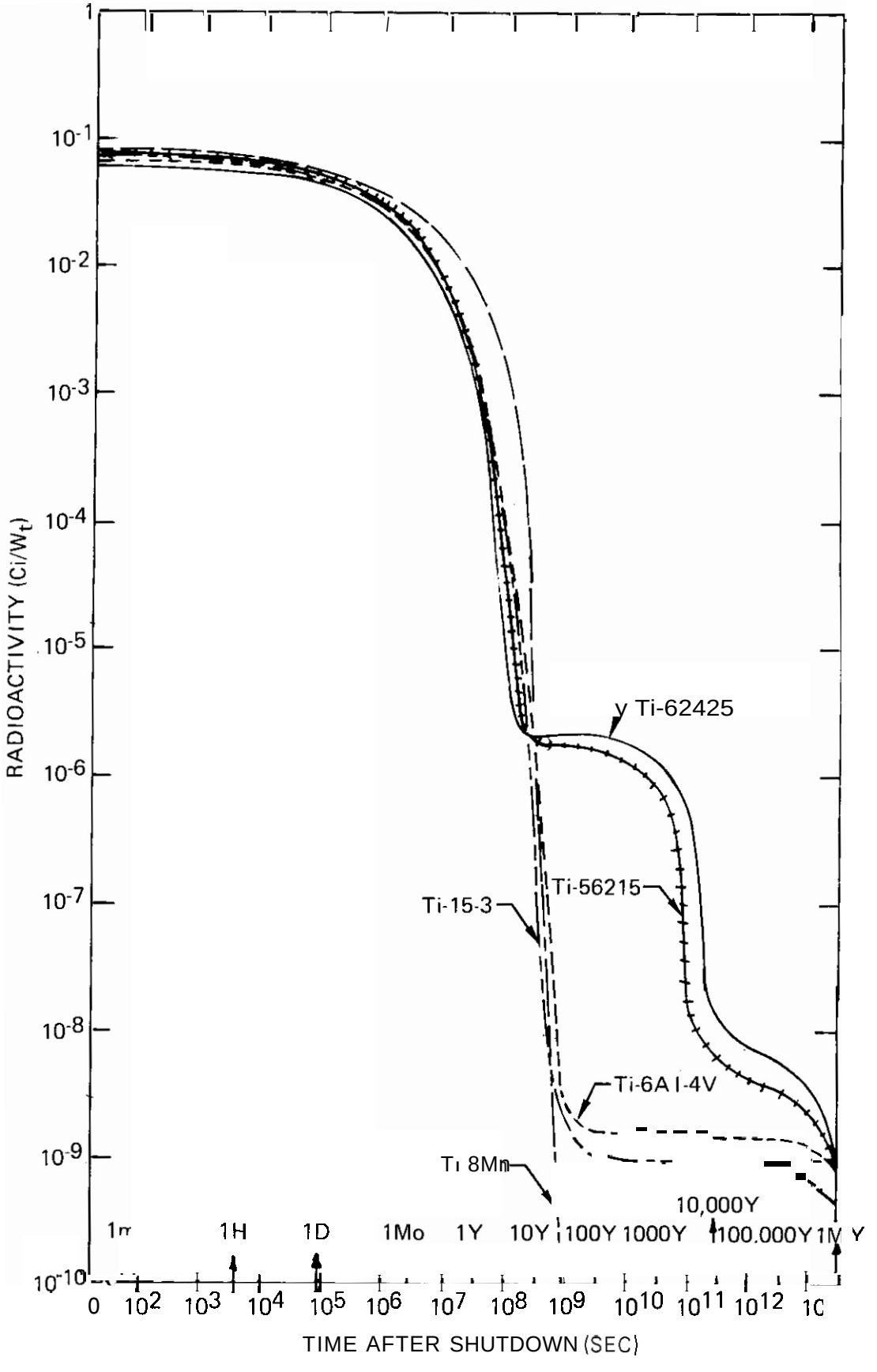

Figure 1.1.2 Radioactivity of Several Candidate Fusion Reactor Structural Materials

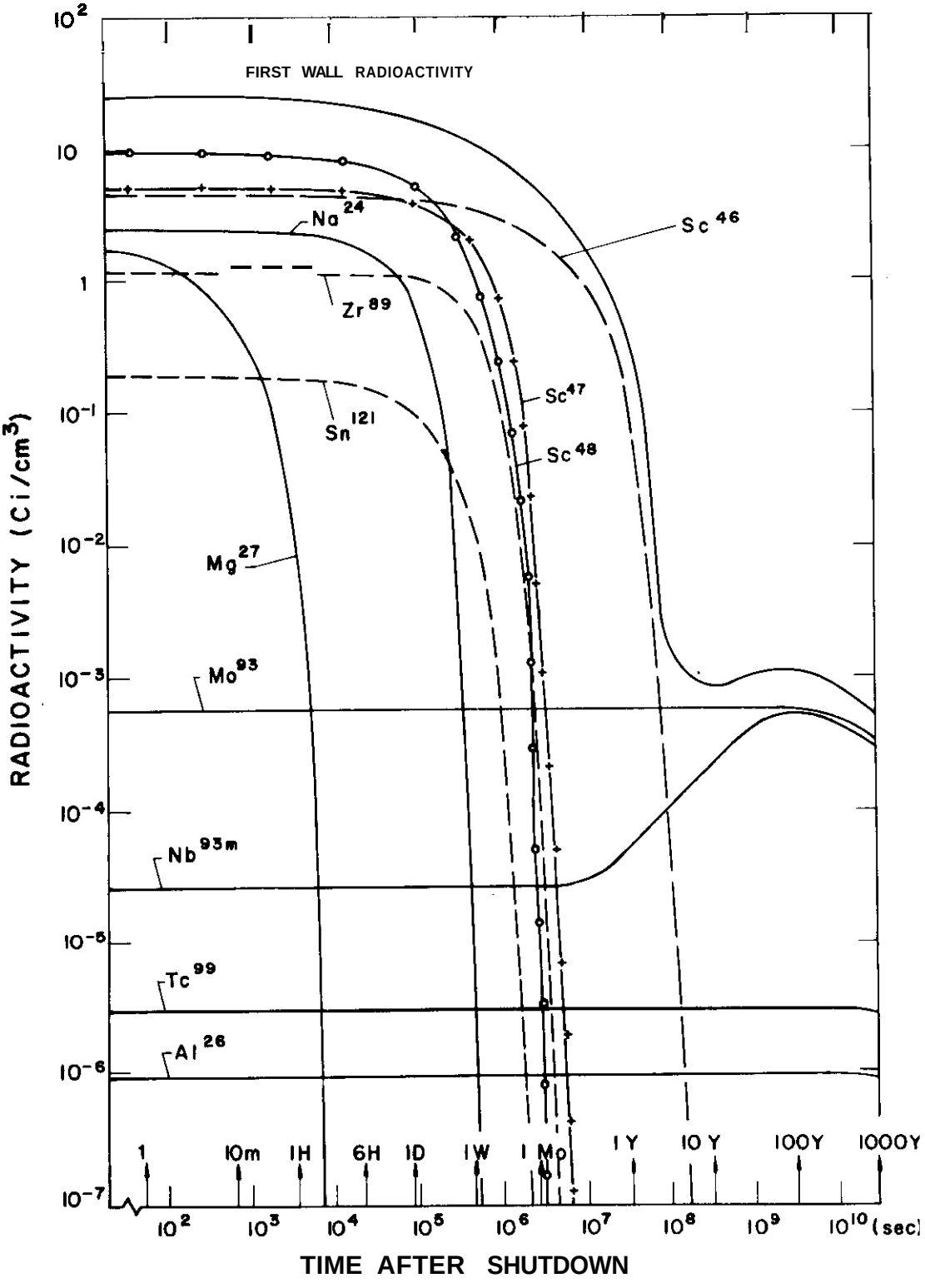

Figure 1.1.3 Radioactive decay of Ti—6242s

The impact of lowering the aluminum concentration can be seen by comparing the Ti-15-3 alloy which has 3 w/o Al and Ti-6A1-4V which has 6 w/o Al. As in the case of the molybdenum addition, cutting the aluminum addition in half results in a lowering of the long term radioactivity by roughly a factor of 2.

The isotopes that are responsible for the residual activity of Ti-15-3 are shown in Figure 1.1.4. This figure reveals that the short term radioactivity is from Sc^{48} ($t_{\frac{1}{2}}$ = 1.8 days), Sc^{47} ($t_{\frac{1}{2}}$ = 3.4 days), and Sc^{46} ($t_{\frac{1}{2}}$ = 83.9 days) at shutdown. However, after 1 year of decay, Sc^{46} and Ca^{45} ($t_{\frac{1}{2}}$ = 165 days) dominate the radioactivity until their roles are replaced by V^{49} ($t_{\frac{1}{2}}$ = 330 days) after 3 years. Beyond 30 years, Al^{26} ($t_{\frac{1}{2}}$ = 700,000 years) determines the activity.

The impact of removing aluminum from the titanium alloy can be seen in the case of the Ti-8Mn alloy. After about 1 month of decay the radioactivity is essentially controlled by Sc^{46}, Ca^{45}, and Mn^{54} ($t_{\frac{1}{2}}$ = 300 days). This level of radioactivity is reduced by a factor of 10^8 in 30 years and has decayed to insignificant levels in 50 years, Therefore, from a radioactivity standpoint the Ti-8Mn would be preferred followed by Ti-15-3 and Ti-6Al-4V.

The biological hazard potential (BHP) of these alloys is shown in Figure 1.1.5. Again, it is seen that molybdenum containing alloys undergo a 10^5 to 10^6 reduction of BHP in the first year after shutdown, but remain there for the next several thousand years. Aluminum containing alloys are a factor of 10 or more better while the Ti-8Mn alloy drops 8 orders of magnitude in the first 50 years and the BHP level is insignificant thereafter.

1.1.5 Conclusion

Based on the results of this study the following conclusions can be drawn.

- The use of molybdenum as an alloying element in titanium, even in concentrations as low as 0.8 w/o, makes those alloys comparable to 316 SS for long term radioactivity and therefore they have little advantage in the area of waste disposal. However, the

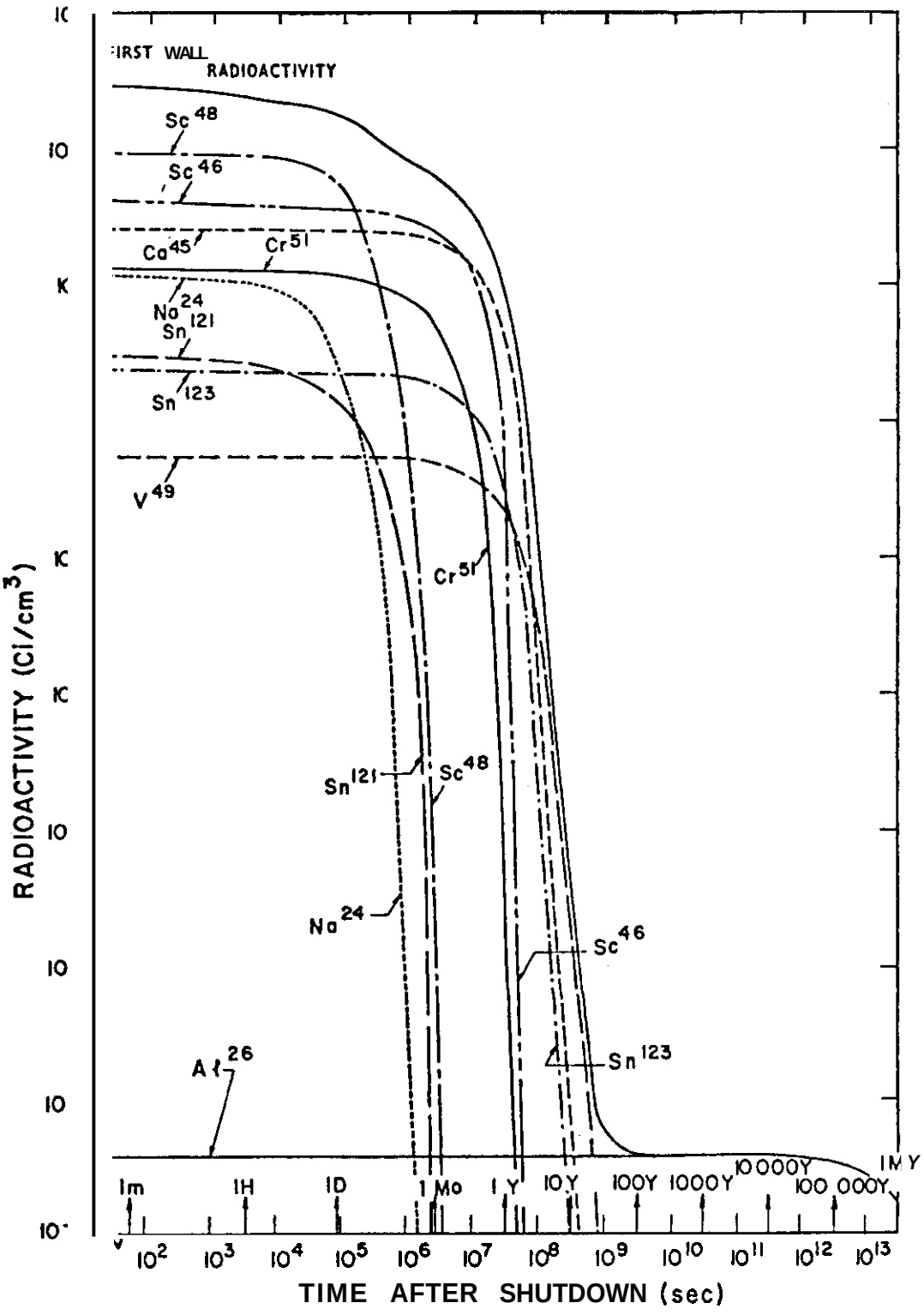

Figure 1.1.4 Radioactive decay of Ti--15—3

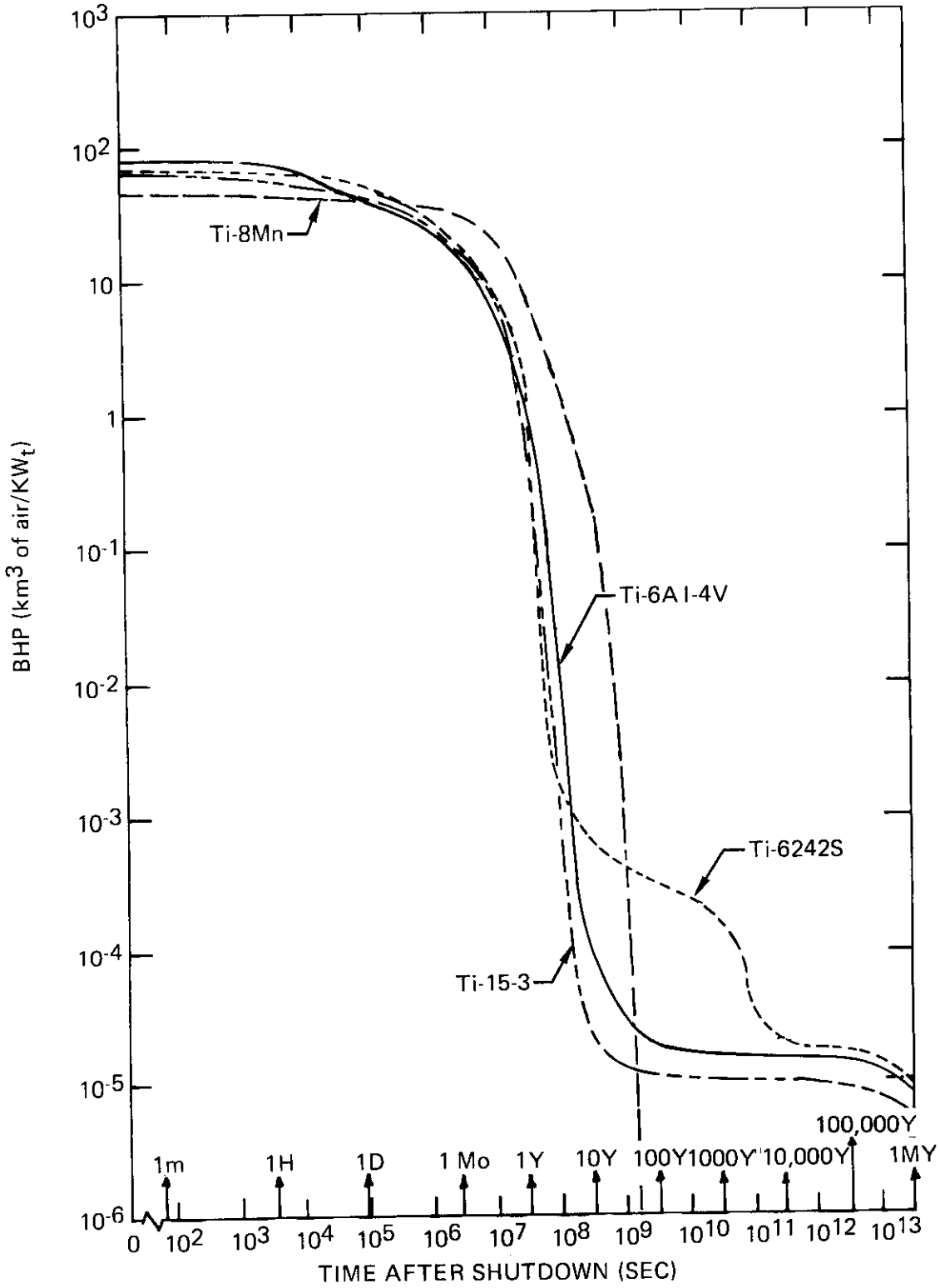

Figure 1.1.5 Biological Hazard Potential of Several Titanium Alloys

addition of molybdenum essentially enhances both room and elevated tensile strength and also provides some phase stability. Therefore, elimination of molybdenum (and other refractory metals, such as, Ta, and Nb) will result in about a 20% reduction of tensile properties. The radioactivity of these alloys could be reduced by substituting tin for the molybdenum. Tin will not have the same impact on the tensile properties as molybdenum does but it is a potent creep strengthener and should result in a more creep resistant alloy than the ones containing molybdenum.

- The use of aluminum as an alloying element in titanium results in a slightly lower long lived radioactivity when compared to "normal" aluminum alloys. The radioactivity of this class of alloys is low enough that they could be recycled after 30 years of storage with modest shielding. The lowering of the aluminum content in Ti-15-3 results in a decrease in radioactivity by a factor of 2 from that of Ti-6Al-4V. The Ti-15-3 alloy more closely approximates an "ideal" composition from a reuse standpoint, however, modifications would have to be made to improve its elevated temperature properties and since it is a beta alloy, its phase stability. If aluminum is to be used in titanium, its concentration should essentially be kept to 1-2 w/o for recycling purposes.
- The use of tin, chromium, vanadium, and silicon in titanium essentially has little effect on its long term radioactive properties. Such alloy systems could probably be handled and reprocessed within 10 to 30 years after shutdown.
- The use of zirconium in titanium would increase the storage time before reprocessing to approximately 300 years or longer.
- The use of manganese, increases the long term radioactivity slightly but would not prevent the reuse in 30 years. However, since it has a tendency to embrittle titanium, it is not recommended.
- Based on strength and radioactivity a possible titanium alloy composition that could be reprocess could be Ti-(1-2) w/o A1-(10-14) w/o Sn-(0.1-0.3) w/o Si.

1.1.6 References

1. S. Peterson, editor, Alloy Development for Irradiation Performance–Quarterly Progress Report for period ending March 31, 1978, pages 23–29.
2. J. W. Davis and G. L. Kulcinski, Assessment of Titanium for Use in the First Wall/Blanket Structure of Fusion Power Reactors, Electric Power Research Institute, EPRI ER–836, April 1977.
3. S. Peterson, editor, Alloy Development for Irradiation Performance - Quarterly Progress Report for period ending March 31, 1978, pages 109–118.
4. S. Peterson, editor, Alloy Development for Irradiation Performance - Quarterly Progress Report for period ending June 30, 1978, Section 5.3.
5. T. Y. Sung, PhD Thesis, University of Wisconsin, 1977.

2. TEST MATRICES AND TEST METHODS DEVELOPMENT

An important part of the alloy development effort is the definition of test matrices and development of test methods. The alloy development strategy will proceed through stages requiring tests of generally increasing difficulty and complexity.

1. Scoping tests will be used to make relative judgments between materials and metallurgical conditions and to identify critical properties. Such tests, which will be used where large numbers of variables are involved, must be rapid, simple, and decisive.

2. Developmental tests will be used for optimization of the Prime Candidate Alloys. They will be broader and more extensive than the scoping tests. In-reactor testing will be an important part of this work.

3. Engineering property tests will be devised to provide the broad data base needed for reactor design.

2.1 DESIGN OF MATERIALS IRRADIATION EXPERIMENT FOR SPECTRAL TAILORING — T. A. Gabriel, E. J. Allen, A. F. Zulliger, J. W. Woods, and E. E. Bloom (ORNL)

2.1.1 ADIP Task

ADIP Task I,A,2. Define test matrices and test procedures.

2.1.2 Objective

In order to reproduce in real time in fission reactors the He/dpa ratio expected near or at the first wall in fusion reactors for stainless steel and nickel-base alloys, it is necessary to vary the thermal-to-fast neutron flux ratio within the experimental locations since the helium and dpa production will be dominated by the thermal and fast fluxes, respectively. The objective of this work is to determine the degree of spectral tailoring required and to design experimental capsules that will produce the needed changes.

2.1.3 Summary

For stainless steel and nickel-base alloys the He/dpa ratio expected near or at the first wall of a fusion reactor can be reproduced within reasonable limits in real time in fission reactors such as ORR because of the helium production characteristics of nickel ($^{58}Ni + n_{th} \rightarrow {}^{59}Ni$; $^{59}Ni + n_{th} \rightarrow {}^{56}Fe + a$).[1] This can be accomplished by continuous modification of the thermal-to-fast neutron flux ratio since the helium production will be dominated by the thermal flux and the fast flux will determine the dpa.[1-3] This report summarizes some of the neutronic calculations that are being carried out to determine (1) the amount of change as a function of time necessary in the thermal-to-fast flux ratio and (2) the design of the experimental capsules that will produce the needed changes.

2.1.4 Progress and Status

The results of the preliminary calculations in which the ORR is to be used to obtain in real time the same He-to-dpa ratio in stainless steel as expected in the first wall of a fusion reactor are shown in Fig. 2.1.1.

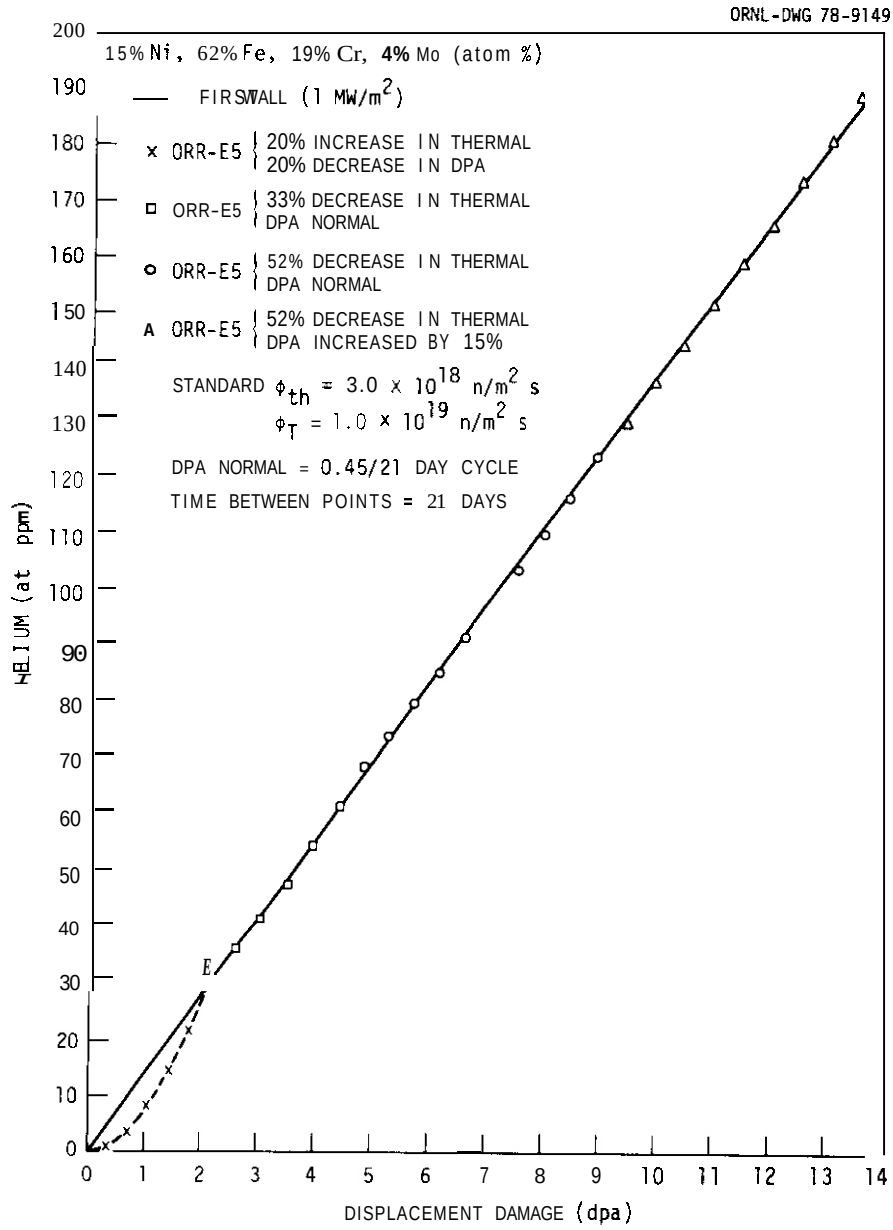

Fig. 2.1.1. Helium vs Displacement Production as Expected on the First Wall of a Fusion Reactor and What Can be Obtained in the ORR.

The solid straight line represents the helium and displacement production expected at the first wall of a fusion reactor. Approximately 10 dpa and 140 at. ppm He per year will be obtained for a 1 MW/m^2 wall loading. To obtain this level of damage in ORR will require about 1.3 years of irradiation. The points represent calculated damage obtained by use of a representative ORR neutron spectrum, but with variations of the thermal and fast fluxes. Initially the thermal flux is increased by *20%* and the dpa production rate is decreased by *20%.* A decrease in dpa production rate means a corresponding decrease (not necessarily *20%)* in the fast flux. Following this initial increase in the thermal flux, the remainder of the time of irradiation requires various reductions in the thermal flux and various increases in the fast flux.

To obtain a better understanding of how the thermal-to-fast flux ratio can be varied in ORR, two preliminary 3-D neutron-diffusion calculations using the VENTURE[4] computer code were made of the ORR core configuration shown in Fig. 2.1.2. The materials irradiation experiments were modeled in core positions C3, C7, E3, and E7 with various core piece compositions. A typical graphite irradiation experiment was located in position E5. The model of the core piece used in the calculation is shown in Fig. 2.1.3. The compositions of the core pieces that were investigated are listed in Table 2.1.1. Given in Fig. *2.1.4* are the variations of the dpa and thermal flux as a function of the H_2O concentrations. Figure 2.1.4 shows that using a 50% H_2O, 50% Be core piece increases the thermal flux by about *20%* and decreases the dpa by about *20%.* These were the changes needed in Fig. 2.1.1 for the initial irradiation period.

Future calculations will be carried out to determine the best methods of reducing the thermal flux and increasing the fast flux required for irradiation experiments of longer duration.

2.1.5 Conclusion

The real time He/dpa production ratio expected near or at the first wall of a fusion reactor in stainless steel and nickel-bearing alloys can be duplicated by tailoring the neutron spectrum in the ORR. Preliminary calculations were carried out to determine how much variation in the thermal

ORNL-DWG 78-9150

POOL
W

A-1 Be	A-2 Be	A-3 210	A-4 180	A-5 195	A-6 165	A-7 225	A-8 Be	A-9 Be
B-1 Be	B-2 240	B-3 165	B-4 SR 110	B-5 150	B-6 SR 110	B-7 165	B-8 240	B-9 Be
Be	210	C3	120	135	120	C7	210	Be
D-1 Be	D-2 DUMMY HT	D-3 135	D-4 SR 140	D-5 120	D-6 SR 140	D-7 135	D-8 HT	D-9 Be
E-1	E-2	E-3	E 4	E-5	E-6 150	E-7 E7	E.8 195	E9 Be
F-1 Be	F-2 225	F-3 180	F-4	F-5 240	F-6 SR 80	F-7 180	F-8 225	F-9 Be
G-1 Be	G-2 Be	G-3 Be	G-4 Be	G-5 Be	G-6 Be	G-7 Be	G-8 Be	G-9 Be

S

N

E

FUEL ELEMENT LOADINGS IN GRAMS OF ^{235}U

Be - BERYLLIUM ELEMENT

HT - HYDRAULIC TUBE

SR - SHIM ROO

Fig. 2.1.2. ORR Core Configuration for Neutron Flux Calculations.

ORNL-DWG 78-9199

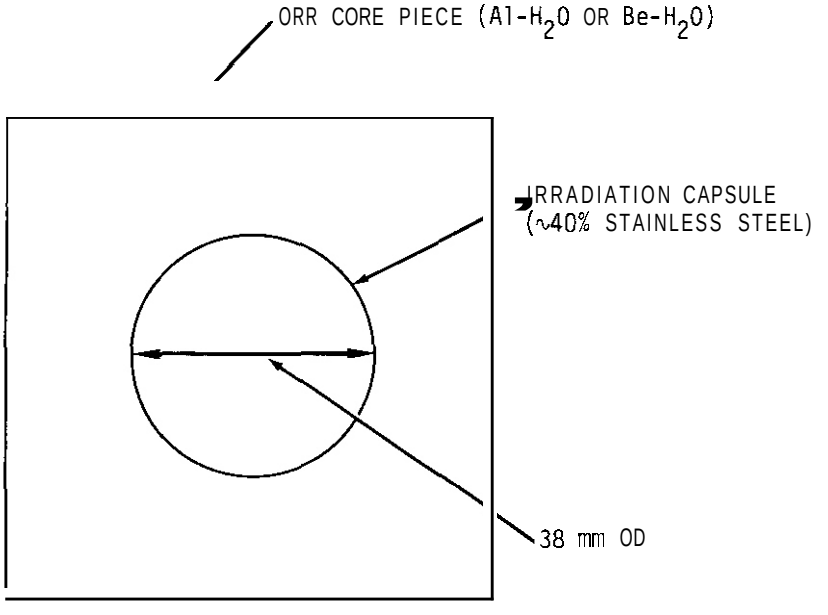

Fig. 2.1.3. Calculational Model of Materials Irradiation Experiment.

Table 2.1.1. Compositions of Core Pieces Used in Calculations

Core Position	Composition of Core Pieces, vol %					
	Calculation 1			Calculation 2		
	Al	Be	H_2O	Al	Be	H_2O
C3	50	0	50	25	0	100
C7	0	100	0	0	50	50
E3	100	0	0	75	0	25
E7	0	100	0	0	75	25

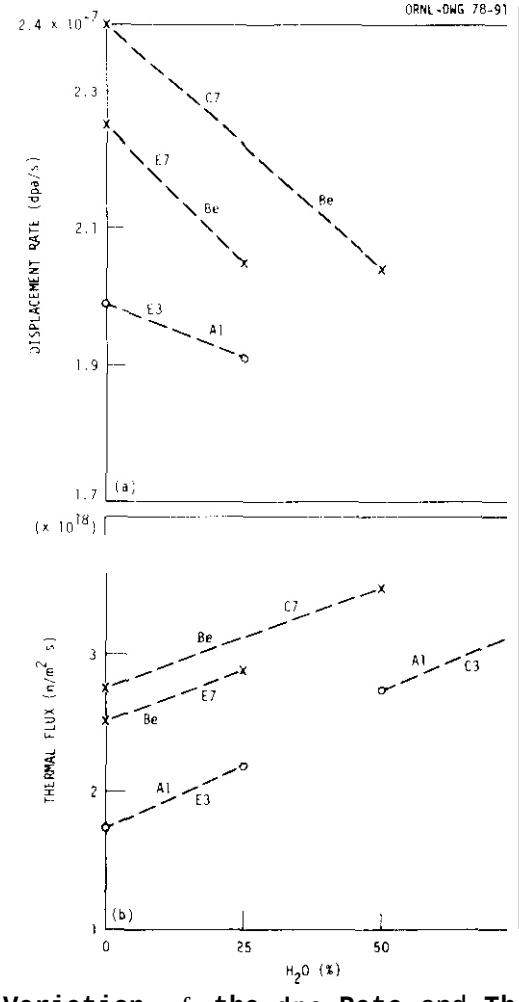

Fig. 2.1.4. **Variation of the dpa Rate and Thermal Flux as Functions of Core Piece Composition.**

and fast fluxes (dpa) was needed. Detailed neutronic transport calculations indicated that the necessary neutron flux modifications are possible.

2.1.6 References

1. T. A. Gabriel, B. L. Bishop, and F. W. Wiffen, *Calculated Irradiation Response of Materials Using Fission Reactor (HFIR, ORR, and EBR-II) Neutron Spectra*, ORNL/TM-6361 (in preparation).
2. T. A. Gabriel, J. D. Amburgey, and N. M. Greene, "Radiation Damage Calculation: Primary Knock-On Atom Spectrum, Displacement Rates, and Gas Production Rates," *Nucl. Sci. Eng.* 61: 21-32 (1976).
3. T. A. Gabriel and B. L. Bishop, *Sensitivity of Primary Knock-On Atom Spectra and Displacement per Atom Cross Sections to Different Secondary Neutron Energy and Angular Distributions and In-Group Weighting Schemes*, ORNL/TM-6108 (January 1978); to be published in Nuclear Science and Engineering.
4. D. R. Vondy, T. B. Fowler, and G. W. Cunningham, *VENTURE, A Code Block for Solving Multigroup Neutronics Problems Applying the Finite-Diffusion-Theory Approximation to Neutron Transport*, ORNL-5062 (October 1975).

2.2 HFIR IRRADIATION OF HOURGLASS FATIGUE SPECIMENS — M. L. Grossbeck and M. J. Kania (ORNL)

2.2.1 ADIP Task

ADIP Task I.A.2, Define Test Matrices and Test Procedures.

2.2.2 Objective

The purpose of this project was to develop a method to irradiate tension-compression fatigue specimens in the High Flux Isotope Reactor (HFIR).

2.2.3 Summary

An irradiation capsule similar to that used for tensile specimens[1] has been designed to irradiate fatigue specimens at 300 and 500°C in HFIR. Five capsules were fabricated, two are undergoing irradiation, and three have completed irradiation. The first capsule has now been disassembled and the specimens removed. No capsule failures have occurred, and no significant problems have been encountered.

2.2.4 Progress and Status

2.2.4.1 Introduction

The fusion reactor environment may be reasonably well simulated by the HFIR for nickel-containing alloys since its mixed spectrum produces both displacements and helium through a two-step thermal neutron absorption reaction in nickel.[1] Tensile properties have been previously determined for type 316 stainless steel irradiated in a similar environment.[2] Since tokamak fusion reactors will operate in a cyclic mode, it is necessary to determine fatigue properties to complement the simulated fusion environment tensile data and io develop a simulated fusion irradiation fatigue test program to compare candidate first-wall alloys.

Since tokamak designs are still in a state of flux, a somewhat broad temperature range was selected. Irradiations at 300, 400, 500, and 600°C are planned, with initial emphasis on 300 and 500°C.

2.2.4.2 Radiation Environment

The HFIR is an enriched-uranium-fueled reactor with a large central flux trap to provide an intense thermal flux for isotope production. However, it has six positions at the periphery of the flux trap adjacent to the fuel region, peripheral target positions (PTP), where both thermal and fast fluxes exceed 10^{19} n/m^2 s. The capsules for this series of experiments were designed for and irradiated in PTP. Each capsule contained ten fatigue specimens. Calculated fluxes for the center of each specimen are shown in Table 2.2.1.

Helium levels for these specimens were calculated from chemical analysis data of stainless steels and nickel-base alloys that had been irradiated under similar conditions3 and appear in Table 2.2.1.

Table 2.2.1. Flux and Helium Concentrations for Each Specimen Position

Position	Flux, n/m^2 s			Helium, at. ppm	
	Thermal	>0.1 MeV	Total	5 Cycles	8 Cycles
Top 1	1.5×10^{19}	0.78×10^{19}	3.1×10^{19}	220	450
2	1.7	0.90	3.6	280	570
3	2.0	1.1	4.2	360	720
4	2.3	1.2	4.9	450	880
5	2.4	1.3	5.1	480	930
6	2.4	1.3	5.1	480	930
7	2.3	1.2	4.9	450	880
8	2.0	1.1	4.2	360	720
9	1.7	0.90	3.6	280	570
10	1.5	0.78	3.1	220	450

2.2.4.3 Capsule Design

2.2.4.3.1 Thermal Analysis. Specimens were arranged in tandem along the axis of the capsule in specially designed holders. The holder design provided a helium-filled gap between the specimen and the holder to impede the radial heat flow from the specimens to the 55°C reactor coolant water in order to achieve elevated irradiation temperatures (Fig. 2.2.1). By varying the size of the gas gap, specimen temperatures could he adjusted to design values, in this case 300 and 500°C. Computer iterations were performed until specimen gage section temperatures were within ±10°C of the design temperatures.

The PTP positions of HFIR contain no provisions for real-time temperature monitoring nor for a sweep gas system for temperature control. Therefore, one must rely on the postirradiation examination results or thermal modeling as an indicator of actual irradiation temperature. Thermal modeling was used to design each of the capsules discussed here. The HEATING3 Heat Conduction Program[4] was used to determine steady-state temperature distributions about a mathematical mockup of the capsule.

The HEATING3 program was designed to solve steady-state or transient heat conduction problems in up to three-dimensional Cartesian or cylindrical geometries. Material properties such as thermal conductivity, density, and specific heat may be considered as temperature dependent. Heat generation rates may he both position and time dependent, and boundary conditions may also he time dependent. This program considers all three heat transfer mechanisms — conduction, convection, and radiation — or any combination of the three that is applicable.

Initial constraints on the design were the exterior of the capsule (containment) and the fatigue specimen design. With these two designs fixed it was then necessary to devise a system of specimen holders that would maintain each specimen in a fixed position while providing a high-conductance path for heat to escape. The capsules contained three non-fuel materials: type 316 stainless steel, 6061-T6 aluminum, and stagnant helium backfull gas at a pressure near 0.1 MPa (1 atm). Heat generation was due only to the gamma heating of the stainless steel and aluminum. The gamma heating rates for aluminum[5] and stainless steel[6]

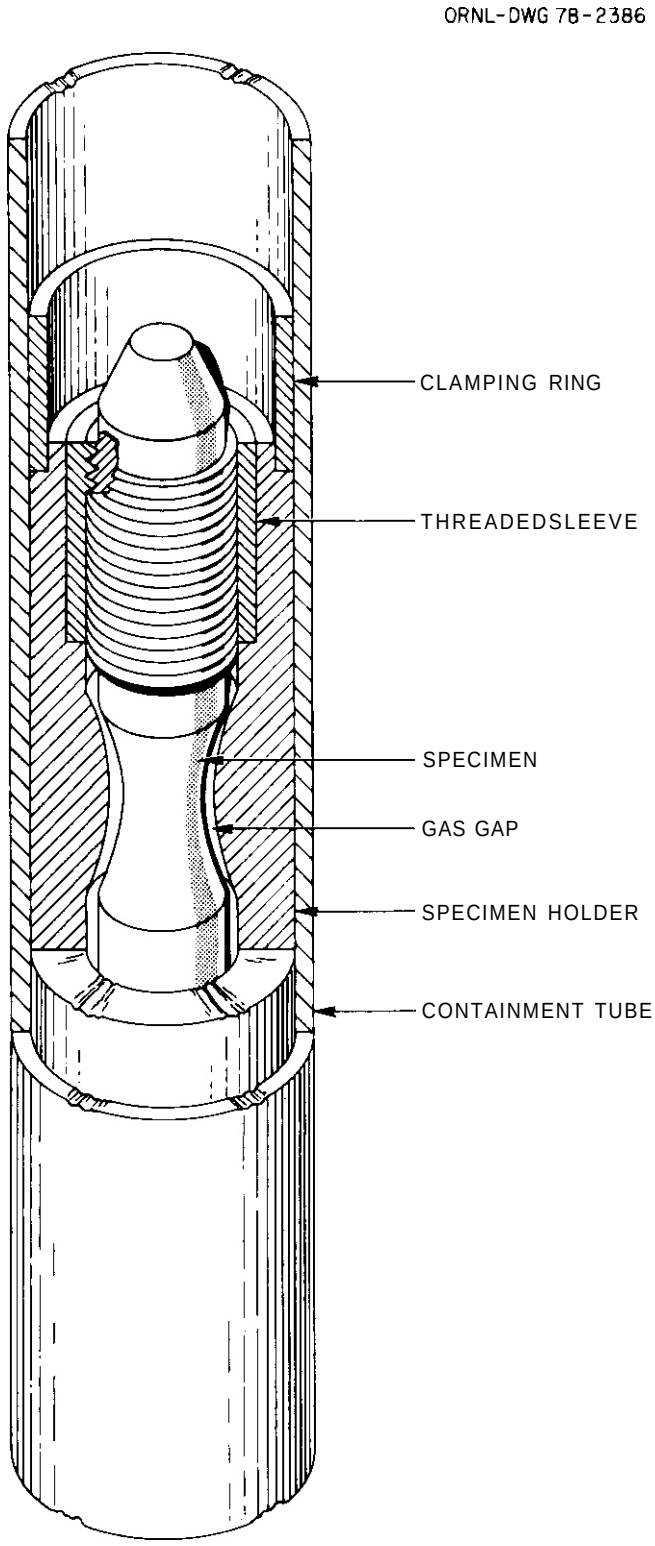

Fig. 2.2.1. Fatigue Specimen Positioned in Holder.

at a HFIR peripheral target position are shown in Table 2.2.2. The rates are spatially symmetric about the reactor horizontal midplane (HMP). Aluminum has a peak value near 35 W/g at the HMP and about 20 W/g 0.25 m from the HMP as determined from measurements in the core center at very low reactor power.[6] The gamma heating rate for stainless steel is somewhat higher, with a peak value at the HMP about 43 W/g. Both gamma heating rates for stainless steel and aluminum were multiplied by the respective densities, 7.92 and 2.70 Mg/m^3, to arrive at power densities (W/m^3) for each material. Helium gas did not contribute to the total heat generated within the capsule.

Specific specimen holder design was then determined by using an *R–Z* mockup of the capsule (actually half the capsule because of symmetric placement about the reactor HMP) and the HEATING3 program. The gamma flux in the HEIR core is symmetric about the reactor HMP. Each specimen position required special consideration because of the spatially dependent gamma heating rates. Temperature control was maintained by adjusting gas gaps along the specimen gage length and the corresponding holder length. The results of these design temperature calculations are shown in Table 2.2.3. The central gas gap dimensions from these calculations are given in Table 2.2.4. Holder dimensions were obtained and the results transferred to mechanical drawings for actual fabrication of the components. Figure 2.2.2 is representative of the calculated temperature profiles along a tensile specimen in the 300°C capsule.

2.2.4.3.2 Structural. The containment capsule was the same as used in previous HFIR irradiations of structural materials.[1,2] The capsule consists of a 12.7-mm-OD 6061-T6 aluminum tube with end fixtures to be accommodated by the HFIR PTP position. A shroud tube of 17.8 mm OD was welded over the containment tube to provide high-velocity coolant flow around the capsule. The overall length of the capsule was 624.7 mm. A small section of 1100 aluminum was welded into the capsule near the bottom to provide a pressure relief in case a leak in the capsule should result in internal steam pressure. Communication was provided between the blowout section and all parts of the capsule. An x-radiograph showing the general features appears in Fig. 2.2.3.

Table 2.2.2. Gamma Heating Rates for Aluminum and Stainless Steel in an HFIR PTP

Specimen Position	Heating Rate, W/g	
	Aluminum	Stainless Steel
1	21	26
2	24	30
3	28	34
4	31	38
5	34	41
6	34	41
7	31	38
8	28	34
9	24	30
10	21	26

Table 2.2.3. Average Gage-Length Temperature for 300 and 500°C Designed Irradiation Capsules

Capsule Placement from HMP	Temperature, °C	
	300°C Capsule	500°C Capsule
1	292	491
2	291	493
3	308	496
4	310	495
5	303	492

Table 2.2.4. Thickness of Central Gas Gap Surrounding Specimen Gage Section

Specimen Position	Gas Gap, mm	
	300°C	500°C
1	0.38	1.02
2	0.38	0.76
3	0.33	0.64
4	0.46	0.51
5	0.41	0.51
6	0.41	0.51
7	0.46	0.51
8	0.33	0.64
9	0.38	0.76
10	0.38	1.02

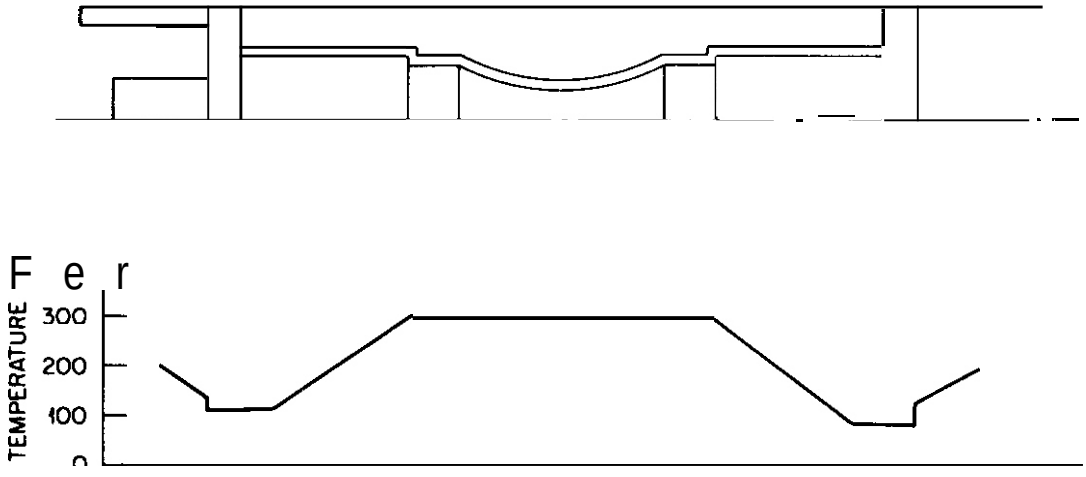

Fig. 2.2.2. Irradiation Temperature Profile of Fatigue Specimen.

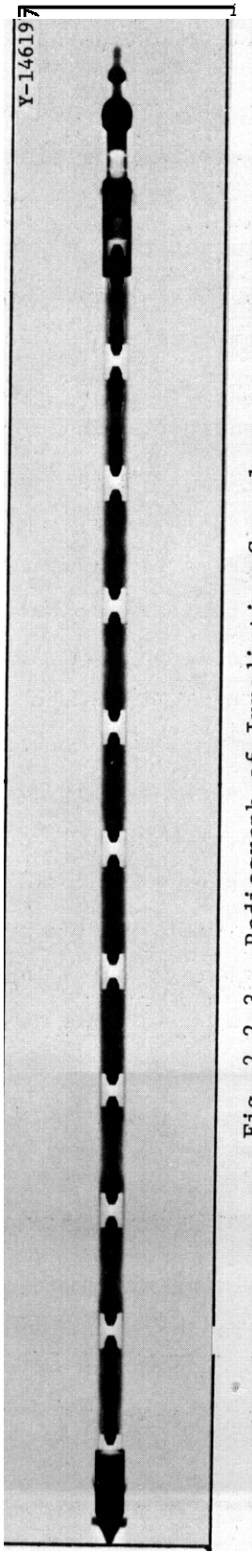

Fig. 2.2.3. Radiograph of Irradiation Capsule.

Each specimen holder was machined from 6061-T6 aluminum and divided into halves longitudinally. The specimen was then threaded into sleeves on each end and precisely centered, and the two halves of the holder were tightly fitted together. A clamping ring on each end held the two halves together (Fig. 2.2.1).

For the four positions closest to the ends of the capsule, threaded sleeves 3.18 mm long were employed. However, the positions closer to core midplane required 10.06-mm sleeves to conduct a greater heat flow.

2.2.4.3.3 Temperature Monitors. Since there is no provision for continuously recording instrumentation in HFIR, temperature monitors for postirradiation examination were installed. Both SiC and low-melting materials were used in this series of experiments.

Silicon carbide is known to increase lattice parameter and macrodimensions upon exposure to radiation.[7] The lattice parameter saturates at a fluence of 3 to 6 $\times 10^{24}$ n/m^2, with the final value dependent upon temperature. Two SiC monitors were placed in each irradiation capsule in 1.59-mm-diam holes as shown in Fig. 2.2.4. The monitors from HFIR-CTR-20 are being examined.

Metals and eutectic alloys have been selected on the basis of melting temperature as well as neutron absorption cross section. Care was taken to select elements that do not transmute to other elements at a significant rate, resulting in a change in composition with a consequent change in melting temperatures. The materials selected are shown in Table 2.2.5.

The materials were ground into coarse powders and packed into small stainless steel capsules 1.59 mm in diameter and of appropriate lengths to fit the holes shown in Fig. 2.2.4. The capsules were flushed with helium and sealed by laser welding end plugs into them. The temperature monitor capsules were then x-radiographed to reveal the premelting condition of the powder, as shown in Fig. 2.2.5.

Because diffusion at temperatures near the melting temperature may round the particle corners, sample capsules of each material were maintained in furnaces within 15°C of their melting temperatures for the

ORNL-DWG 78-9146

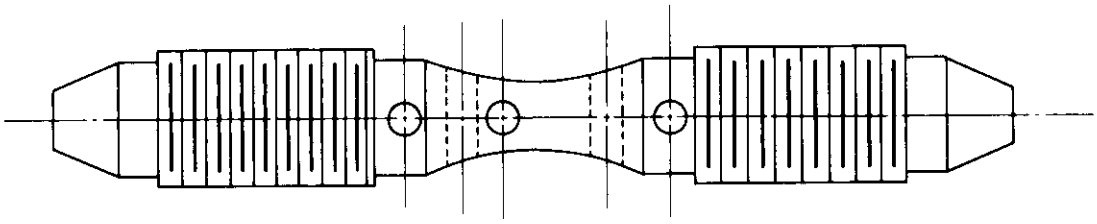

Fig. 2.2.4. Fatigue Specimen with Holes for Temperature Monitor.

Table 2.2.5. Temperature Monitor Materials

For 300°C Capsules		For 500°C Capsules	
Material	Melting Temperature (°C)	Material	Melting Temperature (°C)
Se	215	Zn	420
Pb—5 wt % Pt	290	Cu—31 wt % Mg	485
Pb	327	Mg—24 wt % Ni	507
Zn—5 wt % Al	382	Al—33 wt % Cu	548
		Al—12 wt % Si	577

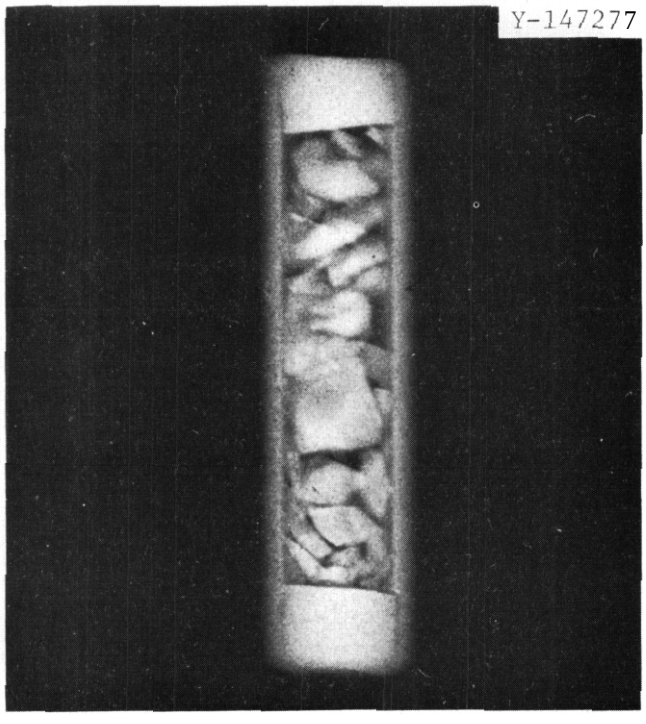

Fig. 2.2.5. Radiograph of Temperature Monitor Containing Selenium.

duration of five HFIR cycles. With the exception of one sample, which clearly melted, probably from an accidental temperature excursion, no evidence of surface rounding was observed.

A device has been constructed to remove the monitor capsules from the fatigue specimens remotely during hot cell disassembly. All monitors from HFIR-CTR-20 have been removed and radiographed.

2.2.4.4 Postirradiation Disassembly

Experiment HFIR-CTR-20 was removed from the reactor on January 11, 1978, and disassembled. Since this was the first fatigue experiment of this series, its disassembly has provided experience that will prove valuable for working with the other capsules of this series. Because of its value to future experiments, each major disassembly operation was documented with photographs, and a rather detailed description of the procedure is included. The capsule as removed appears in Fig. 2.2.6(a).

Figure 2.2.6(b) shows the capsule as it appeared after removal of the outer shroud. The surface is covered with a gray oxide, generally

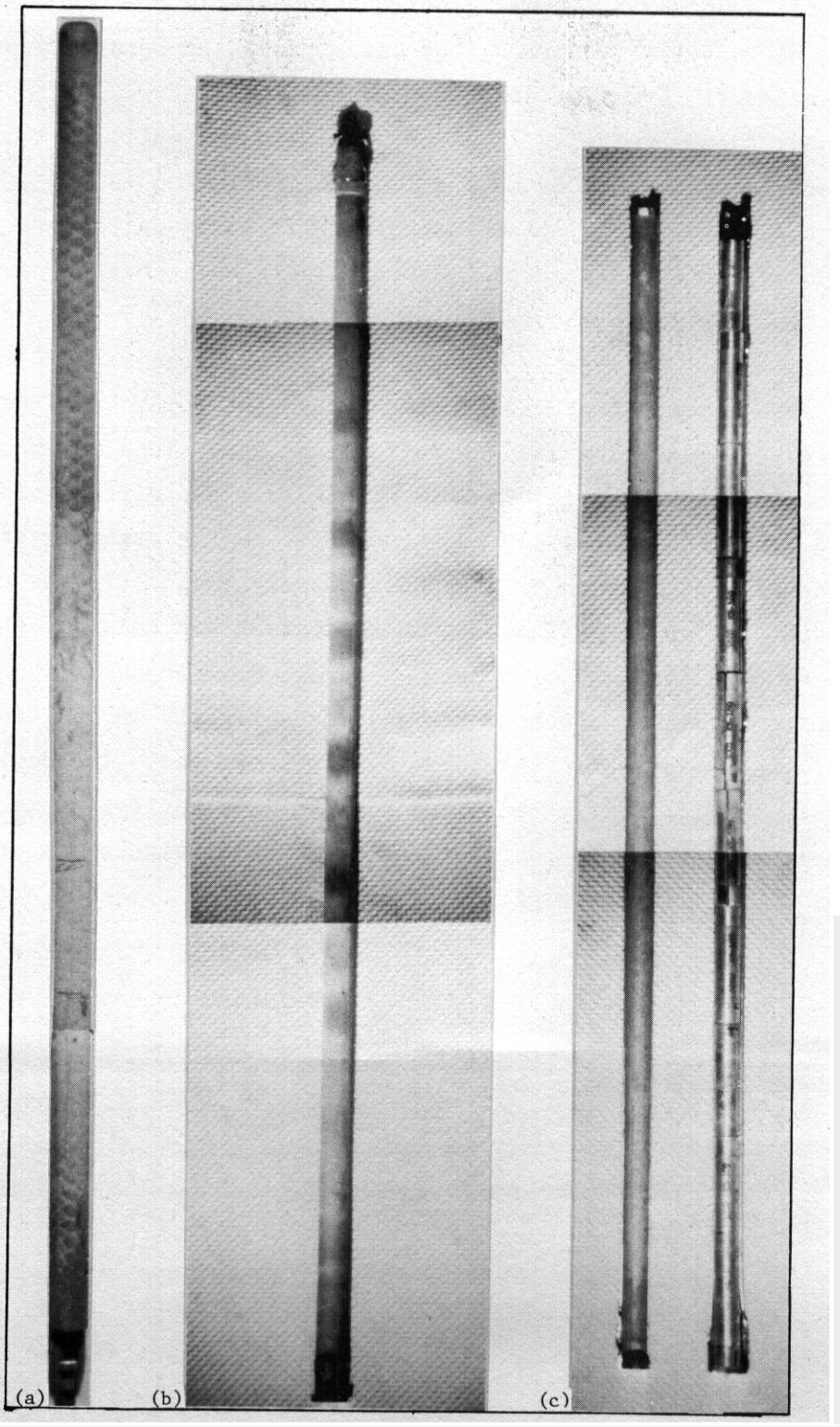

Fig. 2.2.6. Capsule HFIR-CTR-20 (a) as it Appeared when Removed from the Reactor, (b) with Outer Shroud Removed, and (c) Opened Revealing Specimen Holders.

adherent but disrupted in places. The containment capsule had what appeared to be a suspicious crack, but later proved to be a only a crack in the oxide layer. Examination of the capsule wall showed it to be structurally sound, the oxide being thin compared with the wall thickness.

The capsule was opened by making two longitudinal cuts and separating the halves. The opened capsule, with specimen holders visible, appears in Fig. 2.2.6(c). A few holders and retainer rings show inconsequential shallow saw cuts.

It is important to examine the position of the specimens in the holders to make certain that the specimens have not rotated in the threaded sleeves, resulting in a nonuniform gas gap. This was known to have happened to two specimens in HFIR-CTR-20 from a preirradiation radiograph. The problem has now been corrected in the assembly procedure. Since an x-radiograph of a capsule so very radioactive is not possible with our facilities, a neutron radiograph was considered but eliminated by high cost.

We constructed a jig to hold the specimens tightly in position in one half of the holder while the other half was removed. The device, which appears in Fig. 2.2.7, performed very satisfactorily. A representative specimen is shown in position in three consecutive steps of removal in Fig. 2.2.8. The thin slit that appears in the threaded sleeve

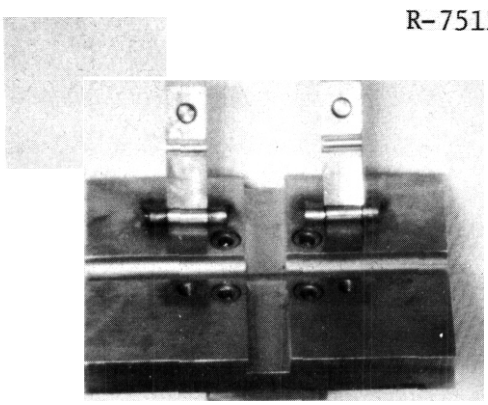

Fig. 2.2.7. Device for Holding Specimen in Position While Separating Halves of Holder.

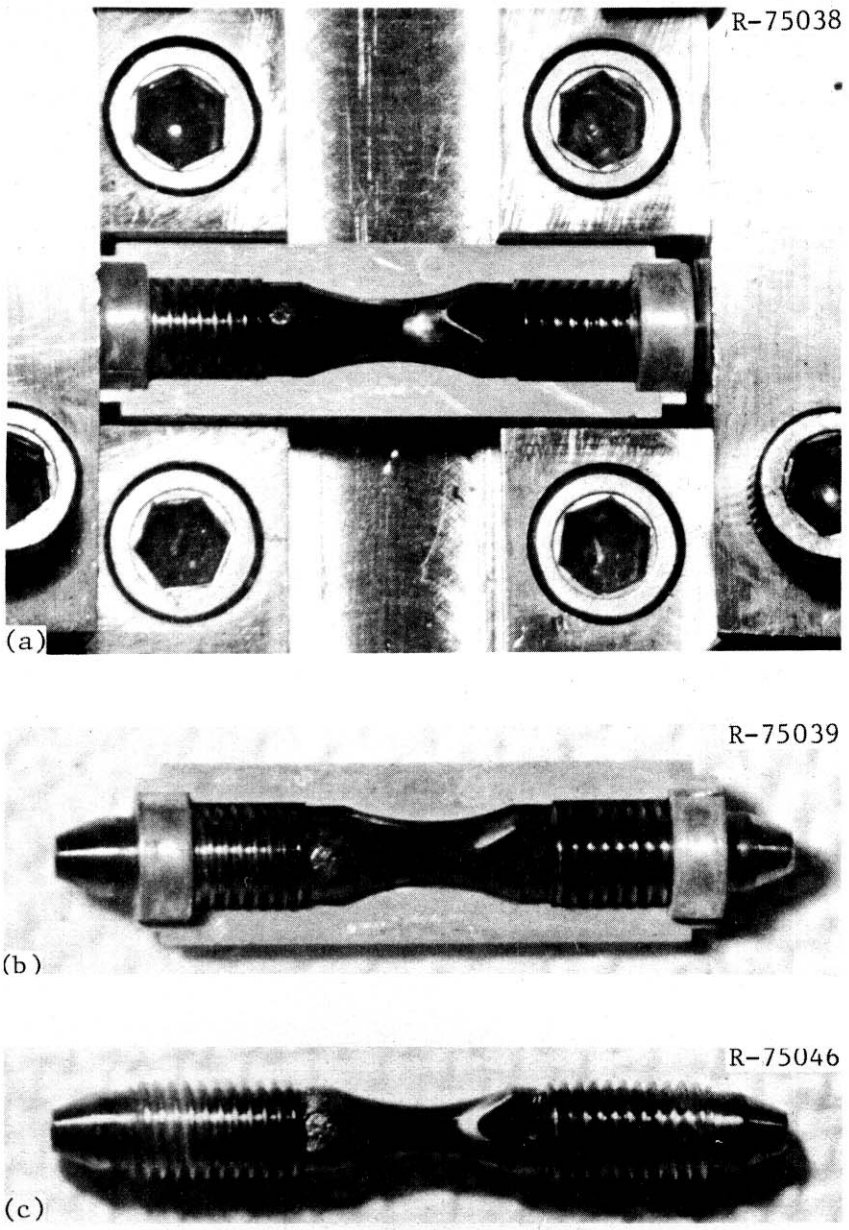

Fig. 2.2.8. Irradiated Fatigue Specimen Containing Two Temperature Monitors. (a) In disassembly device. (b) In holder with upper half removed. (c) Removed from holder.

was made to facilitate removal. Two temperature monitors can be seen in the specimen in a position that does not interfere with fatigue testing. The gage section appears uniform in brightness; actually it is a uniform gold color, indicating a uniform irradiation temperature. The specimens that had shifted in their holders were blue on one end and gold on the other. The specimen with temperature monitors in the center also appeared blue, indicating that perhaps the presence of the monitors perturbed the gamma heating rate sufficiently to depress the temperature. Future experiments will not have temperature monitors in the center of the specimen gage section.

The disassembly proceeded smoothly; all components were removed without excessive force. The same techniques will be used on the remaining fatigue capsules.

2.2.5 Conclusions

An irradiation capsule for miniature hourglass fatigue specimens has been developed and tested. It appears to have been very successful, although a final evaluation awaits examination of the temperature monitors. Disassembly proceeded as expected with no unusual occurrences. The temperature monitor technique employing coarse powders and x-radiography is also a new and promising method.

2.2.6 References

1. F. W. Wiffen and E. E. Bloom, "Effect of High Helium Content on Stainless Steel Swelling," *Nucl. Technol.* 25: 113–23 (1975).
2. E. E. Bloom and F. W. Wiffen, "The Effects of Large Concentrations of Helium on the Mechanical Properties of Neutron-Irradiated Stainless Steel," *J. Nucl. Mater.* 58: 171–84 (1975).
3. F. W. Wiffen, E. J. Allen, H. Farrar, E. E. Bloom, T. A. Gabriel, H. T. Kerr, and F. G. Perey, "The Production Rate of Helium During Irradiation of Nickel in Thermal Spectrum Fission Reactors," paper to be presented at the First Topical Meeting on Fusion Reactor Materials, Jan. 29–31, 1979, Miami Beach, Florida.

4. W. D. Turner and M. Siman-Tov, *HEATING3 — An IBM 360 Heat Conduction* Program, ORNL/TM-3208 (February 1971).
5. Personal communication, B. H. Montgomery to M. J. Kania, August 1974.
6. Personal communication, H. T. Kerr to M. J. Kania, August 1976.
7. J. E. Palentine, "The Development of Silicon Carbide as a Routine Irradiation Temperature Monitor, and Its Calibration in a Thermal Reactor," *J. Nucl. Mater. 61:* 243-53 (1976).

2.3 DEVELOPMENT OF SMALL FATIGUE-CRACK GROWTH SPECIMENS FOR IN-REACTOR AND POSTIRRADIATION TESTING - L. A. James, R. E. Bauer and J. L. Straalsund (Hanford Engineering Development Laboratory)

2.3.1 ADIP Task

Task Number 1.B.1.1, Specimen and Test Method Development

2.3.2 Objective

The objective of this program is to establish the effects of Magnetic Fusion Reactor (MFR) environments on the mechanical properties of MFR materials. The specific objective of the work described in this report is to develop specimen designs and will allow one to determine if any major differences exist between high cycle fatigue-crack growth properties measured during (in-situ) and after (postirradiation) irradiation.

Due to the cyclic nature of the first wall environment for most MFR designs, it is anticipated that figure-crack growth will be an important consideration in DMFE alloy development activities. The most convenient means of assessing this property for a wide range of alloys is through the use of postirradiation techniques. However, significant differences may exist between the behavior observed in a postirradiation test and that exhibited by the material during irradiation. For example, fatigue-crack growth during irradiation may be retarded if irradiation creep processes relax the residual stresses at the tip of the crack, or blunt the crack tip. Other mechanisms could be advanced which result in enhanced growth rates. Thus, exploratory tests are needed to determine if major differences exist between in-situ and postirradiation fatigue-crack growth rates.

2.3.3 Summary

Miniature fatigue-crack growth specimens have been developed which will allow in-reactor and postirradiation tests to be conducted efficiently, minimizing both irradiation space and temperature differential (due to gamma heating) considerations. The specimen developed for postirradiation testing utilizes a small (approximately 12.7 x 25.4 x 0.46 mm) central section which is irradiated to the desired fluence. Following irradiation,

end tabs are then welded onto the irradiated central section thereby creating a center-cracked fatigue specimen of relatively standard design except for its reduced dimensions and welded central section.

The results *to* date have indicated that this specimen design produces fatigue-crack growth rate data which is in excellent agreement with results for larger, non-welded designs, and is suited for both in-reactor and postirradiation testing.

2.3.4 Progress and Status

Fatigue-crack growth rate tests on unirradiated materials generally employ relatively large specimens. This is because, for a given crack length measuring system, better relative accuracy is achieved with larger specimens. Consequently, there has been little motivation to develop miniaturized specimens. Postirradiation fatigue-crack growth tests have been conducted on austenitic stainless steels,[1,2] but here again the volumes have been relatively large. Shahinian, et al.,[1] irradiated blocks of material approximately 55.9 x 63.5 x 12.7 mm (2.2 x 2.5 x 0.5 in) and welded on specimen extensions following irradiation, and Kussmaul, et al.,[3] welded irradiated cylindrical sections *48* mm diameter x 66 mm thick (1.89 in dia x 2.60 in thick) into the center of large fracture toughness specimens. In both of these cases, the investigators were able *to* show that the welds were sufficiently remote so as not to influence the test results.

A number of questions arise in the design of a miniaturized specimen utilizing welded-in inserts: (1) Are crack growth properties thickness-dependent, or are buckling problems encountered when testing thin sections? (2) Can acceptable relative accuracy be achieved with narrow specimens? (3) Can the length of the specimen be reduced below the usual length/width ratio of about 4:1 ? *(4)* will the proximity of the weld on relatively small welded inserts influence the fatigue-crack growth rates?

The answer to the first question was addressed in Reference *4* which found that center-cracked specimens as thin as 0.25 mm (0.01 in) gave results equivalent to those observed in heavier plate material. Buckling problems were minimized by employing a symmetrical specimen such as the center-cracked design.

The answers to the second, third and fourth questions were the ojbective of the present work. A series of specimen designs (Types 1-3 in Figure 1) were fabricated from the same heat of annealed Type 304 SS and tested at room temperature. The material was 0.46 mm (0.018 in) thick in all cases. Types 1a and 1b had widths 25.4 mm (1.0 in) and 50.8 mm (2.0 in), respectively, and both types were about 203 mm (8 in) long. Types 2 and 3 utilized a welded-in center section 25.4 mm (1.0 in) wide, 12.7 mm (0.5 in) long, and 0.46 mm (0.018 in) thick. Type 2 had a more conventional length/width ratio, while Type 3 had a reduced length in order to conserve space for in-reactor testing.

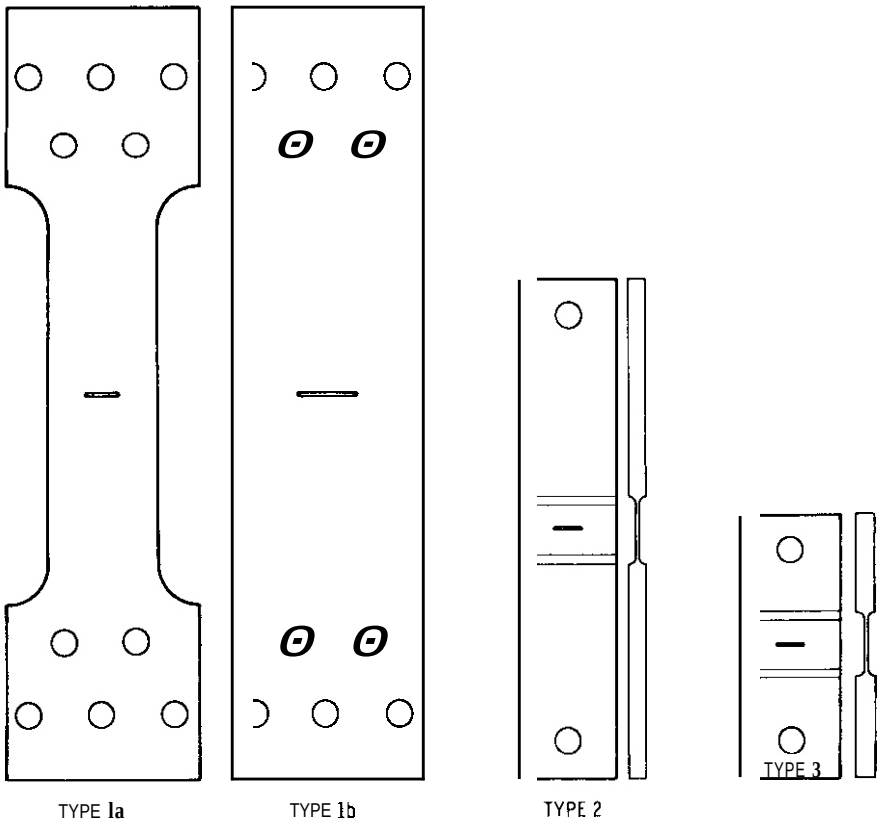

Figure 1. Specimen designs employed in specimen development.

The results, plotted in Figure 2, show that all four specimen types yielded essentially eqivalent results, and that the results also agreed well with data for ten different specimen designs for annealed Type 304 SS plate material from Reference 5. In addition, the present results generally fall within a scatter factor of 2 on da/dN, which is considered normal for intralaboratory tests on a single heat of material.[6] No apparent effect of specimen thickness, width or length/width ratio is observable, nor does the relatively close proximity of the weld seem to influence the cracking behavior. Therefore, the design illustrated by Type 3 appears to meet the test objectives of providing accurate reliable data while minimizing irradiation volumes, and is the tentative choice for both in-reactor as well as postirradiation testing. Additional specimens will be tested to increase the statistical confidence in the above conclusions.

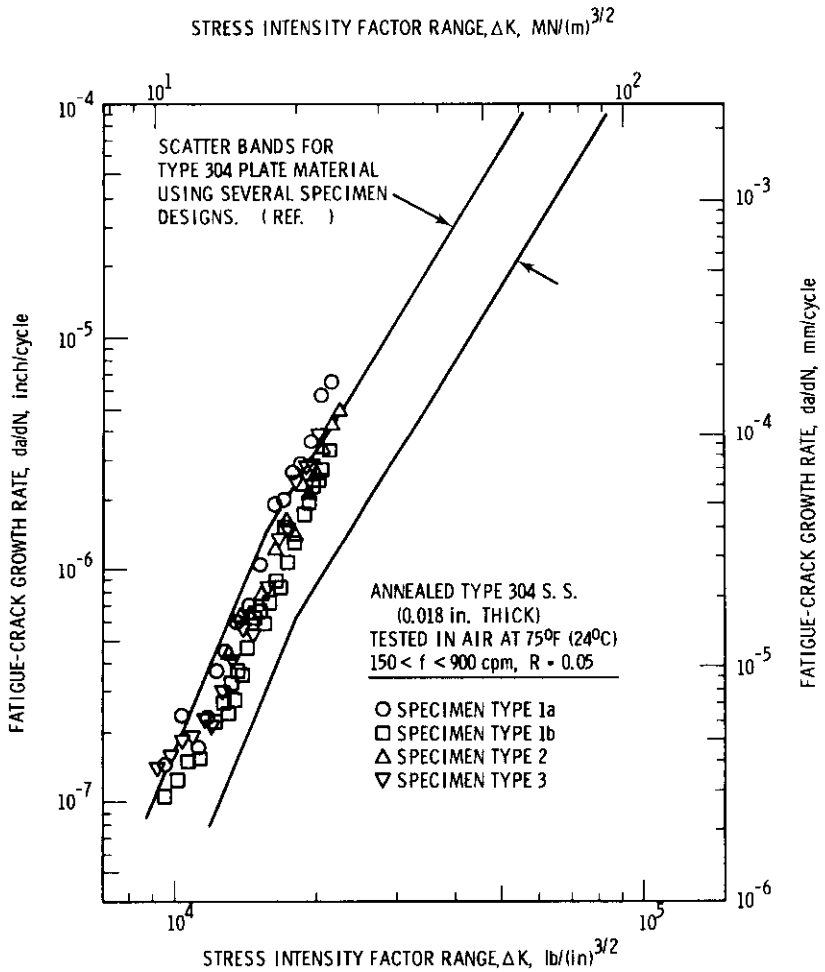

Figure 2. Comparison of fatigue-crack growth rate results for different specimen designs.

2.3.5 Expected Accomplishments

Additional testing of specimen Types 1a, 1b and 3 will be done during the next reporting period.

2.3.6 References

1. P. Shahinian, H. E. Watson, and H. H. Smith, "Effect of Neutron Irradiation on Fatigue Crack Propagation in Types 304 and 316 Stainless Steels at High Temperatures," *Effects of Radiation on Substructure and Mechanical Properties of Metals and Alloys,* ASTM STP-529, pp 493-508, (1973).
2. L. A. James, "The Effect of Fast Neutron Irradiation Upon the Fatigue-Crack Propagation Behavior of Two Austenitic Stainless Steels," *Journal of Nuclear Materials,* Volume 59, pp 183-191 (1976).
3. K. Kussmaul, H. Uetz, and M. Kuri, "Production of Compound Fracture Toughness Specimens to Enable a Large CT Specimen to be Made from a Small Sample Volume," *International Journal of Pressure Vessels and Piping,* Vol. 5, pp 149-156 (1977).
4. L. A. James, E. K. Opperman, and J. L. Straalsund, "Mechanical Performance of MFE Materials," *HEDL Magnetic Fusion Energy Programs Progress Report, January-March 1977,* HEDL-TME 77-41, pp 15-19 (1977).
5. L. A. James, "Fatigue-Crack Propagation in Austenitic Stainless Steels," *Atomic Energy Review,* Vol. 14, pp 37-86 (1976).
6. W. G. Clark and S. J. Hudak, "Variability in Fatigue Crack Growth Rate Testing," *Journal of Testing and Evaluation,* Vol. 3, pp 454-476 (1975).

3. PATH A ALLOY DEVELOPMENT — AUSTENITIC STAINLESS STEELS

Path A alloys are those alloys generally known as austenitic stainless steels. The most common U.S. designations are ALSI types 304, 316, 321, and 347. Primary considerations for selecting this class of allays for further development are:

1. state-of-the-art production and fabrication technology;
2. extensive data on the effects of neutron irradiation on properties, which show the potential of these alloys for MFR applications;
3. compatibility with proposed coolants and breeding fluids;
4. evidence that for MFR conditions (He, dpa, temperatures) the properties are sensitive to composition and microstructure — thus showing potential for further development.

The strategy for development of these alloys has two related objectives:

1. to determine for a reference alloy the effects of irradiation on those properties most important to fusion reactor design;
2. to develop a path A alloy that is optimized for fusion reactor applications.

The first objective will provide a data base for near-term reactor design and, most important, guidance as to which properties limit performance of this type alloy. Work on the reference alloy will provide direction for the actual alloy development efforts of the second objective. Type 316 stainless steel in the 20%-cold-worked condition appears to be the best choice as a reference alloy. It is the present reference cladding and duct alloy in the breeder reactor programs, and there are extensive data on the unirradiated mechanical properties, effects of heat treatment on properties, structure, and phase stability, and the effects of fast-neutron irradiation on properties. The present technology of astenitic stainless steels, including understanding of the physical and mechanical properties and irradiation response, is such that alloy development efforts can move to optimization for use in fusion reactor applications. A Prime Candidate Alloy (PCA) (Fe—16% Ni—14% Cr—2% Mo—2% Mn—0.5% Si—0.2% Ti—0.05% C) has been selected

by the ADIP task group. Efforts will now focus on optimizing the composition and microstructure of the PCA leading towards the selection of OPT-A1 (Program Plan designation of first optimized A alloy).

3.1 STATUS OF HELIUM-PREINJECTED ANNEALED AND 20%-COLD-WORKED TYPE 316 STAINLESS STEEL IRRADIATED IN EBR-II at 500 AND 625°C — P. J. Maziasz and J. A. Horak (ORNL)

3.1.1 ADIP Tasks

ADIP Tasks I.C.2, Microstructures and Swelling in Austenitic Alloys, and I.B.13, Tensile Properties of Austenitic Alloys.

3.1.2 Objective

The objective is to determine the effect of helium preinjection followed by irradiation to produce displacement damage in the microstructure and mechanical properties of type 316 stainless steel and compare these effects with those resulting from irradiation producing simultaneous helium and displacement damage to similar levels.

3.1.3 Summary

Sheet tensile specimens of annealed and 20%-cold-worked type 316 stainless steel have been preinjected with 80 and 200 at. ppm He by use of 60-MeV alpha particle irradiation at 20°C at the Oak Ridge Isochronous Cyclotron (ORIC). The samples were then irradiated at 500 and 625°C in the Experimental Breeder Reactor II (EBR-II) in experiment *X-264*, to neutron fluences up to 2.3 x 10^{26} n/m^2 (>0.1 MeV). Tensile property and microstructure response will be compared with that obtained in the same heat of type 316 stainless steel in the same preirradiation microstructural condition irradiated in the High Flux Isotope Reactor (HFIR) to neutron fluences producing similar helium and displacement damage levels simultaneously at nearly the same temperatures. This comparison will show whether or not preinjection followed by fast reactor irradiation is a valid simulation of producing helium and displacement damage simultaneously.

3.1.4 Progress and Status

Details of the helium implantation have been reported by Horak.[1] Briefly, small sheet tensile specimens of annealed (1 hr at 1050°C) and 20%-cold-worked type 316 stainless steel were irradiated with 60-MeV alpha particles at 20°C with the ORIC. The alpha beam was passed through a degrader to spread the incident energy to distribute the helium uniformly through the thickness of the specimen.

The specimens were irradiated in EBR-IT, Row 8, in experiment X-264, to neutron fluences up to 2.3 x 10^{26} n/m^2 (>0.1 MeV). An irradiation temperature of about 650°C was attained by locating the specimens near a heat pipe at approximately the same temperature. An irradiation temperature of 500°C was attained in gamma-heated capsules with gas gap temperature control, and the experimental assembly is shown in Fig. 3.1.1. The irradiation has been completed and the experiments disassembled. Recovery of the specimens from the sodium-filled capsule required special care because of the presence of refractory metals, which are prone to hydrogen pickup. Reacting sodium with water or alcohol liberates hydrogen. A technique employing spraying liquid anhydrous ammonia to dissolve the sodium and then converting it to Na_2O upon evaporation of the ammonia was developed and produced excellent results.

A test matrix for mechanical properties and microstructural examination is given in Table 3.1.1. In the case of 20%-cold-worked type 316 stainless steel irradiated at 500°C, only one sample was available at each condition, so priority was given to transmission electron microscopy (TEM) to determine the microstructural response for a complete TEM matrix. For comparison, 20%-cold-worked type 316 has been irradiated in HFIR to a neutron fluence of 8.75 x 10^{25} n/m^2 (>0.1 MeV) to produce 306 at. ppm He at 470 and 560°C. Data have also been reported[2,3] on the same material irradiated in HFIR at 580°C to a neutron fluence of 4.7 x 10^{25} n/m^2 (>0.1 MeV) to produce 85 at. ppm He. Comparison of the swelling, mechanical properties, and microstructure developed by the samples preinjected with helium and irradiated in EBR-II with uninjected samples irradiated in EBR-II and samples irradiated in HFIR will indicate whether or not preinjection is a valid simulation technique for fusion irradiation. The experiment

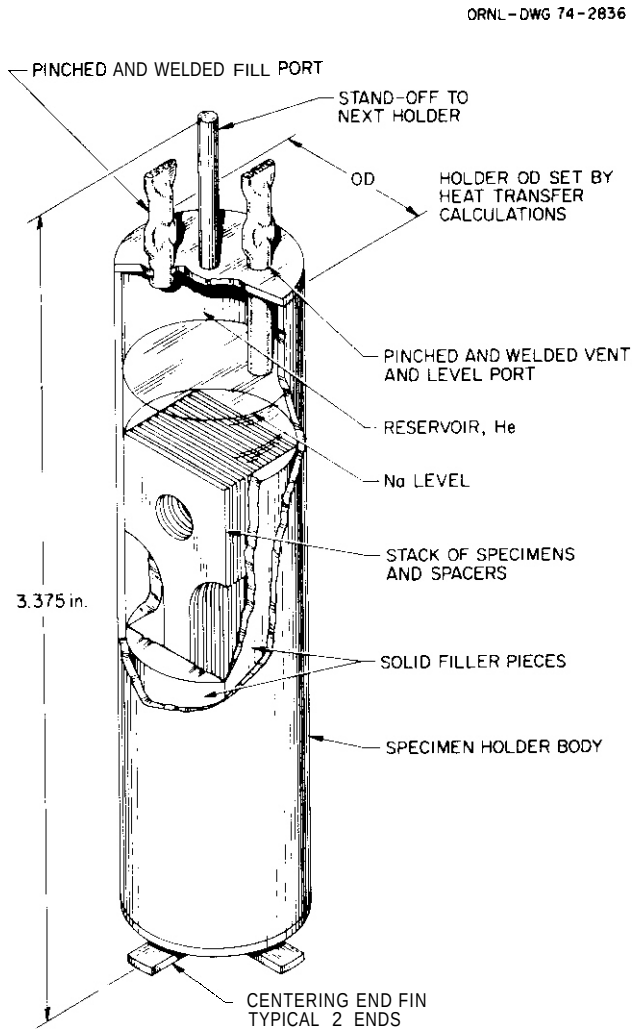

Fig. 3.1.1. Sodium-Filled Specimen Holder for EBR-II Irradiation of Sheet Specimens at 500°C. Type 316 stainless steel miniature sheet specimens were located in the space near the gage of the large specimens. The capsule height shown is 85.72 mm.

Table 3.1.1. Irradiation Conditions and Planned Test Matrix for Type 316 Stainless Steel Irradiated in Experiment X-264 in Row 8 of EBR-II

Alloy Condition	Irradiation Temperature (°C)	Preinjected Helium Level (at. ppm)	Examination[a]
Annealed (1 h at 1050°C)	500	0	TT(500°C), TEM
		80	TT(500°C), TEM
	625	0	TT(625°C), TEM
		80	TT(625°C), TEM
20% cold worked	500	0	TEM
		80	TEM
	625	0	TT(625°C), TEM
		80	TT(625°C), TEM
		200	TT(625°C), TEM

[a]TT = Tensile Test, TEM = Transmission Electron Microscopy.

should help to elucidate the role of helium in development of the damage structure and the resulting properties associated with this damage structure.

3.1.5 Conclusions and Future Work

Future work will include testing the samples as mentioned above. An identical set of samples will be examined by TEM, and the cavity structure, dislocation structure, and precipitation response will be examined. The mechanical properties will be correlated with the microstructure to understand how helium influences this response.

3.1.6 References

1. J. A. Horak, "Helium Implantation in Potential CTR Structural Materials," *Controlled Thermonuclear Materials Technology Annu. Prog. Rep. June 30, 1975,* ORNL-5082, p. 40.
2. P. J. Maziasz and E. E. Bloom, "Comparison of Titanium-Modified and Standard Type 316 Stainless Steel Irradiated in HFIR — Swelling and Microstructure," *ADIP Quart. Prog. Rep. March 31, 1978,* DOE/ET-0058/1(78), pp. 40–53.

3. P. J. Maziasz and E. E. Bloom, "Mechanical Properties of Type 316 and Titanium-Modified Type 316 Stainless Steel Irradiated in HFIR," *ADIP Quart. Prog. Rep. March 31, 1978,* DOE/ET-0058/1(78), pp. 54–62.

3.2 INFLUENCE OF IRRADIATION ON THE PROPERTIES OF PATH A ALLOY WELDMENTS — F. W. Wiffen, D. P. Edmonds, and J. F. King (ORNL)

3.2.1 ADIP Task

ADIP Task I.B.13, Tensile Properties of Austenitic Alloys.

3.2.2 Objective

This work scopes the response of welds and weld-affected zones to irradiation over a range of temperatures and fluences. Welds with type 316 or 16-8-2 stainless steel filler metal joining 20%-cold-worked type 316 base metal are being irradiated in the ORR and HFIR. Tensile tests on the irradiated specimens to determine the effects of irradiation on the mechanical properties will be supplemented by fractography, metallography, and microscopy.

3.2.3 Summary

Irradiation of weld-containing samples at about 55°C to fluences producing 4 to 11 dpa and 100 to 340 at. ppm He resulted in large strength increases in tensile tests at about 35°C but had little effect on the ductility. The ductility was lower in tests at 300 and 700°C. The strength of 16-8-2 welded specimens remained lower than the strength of the 20%-cold-worked base metal, with all tested samples failing in the weld zone.

Fractures in tests at 35°C were of the cup-and-cone geometry, with surfaces covered with ductile dimples. The sample tested at 300°C had failed on a single shear plane, again with ductile dimples covering the fracture surface. The sample tested at 700°C had failed by intergranular separation, indicative of helium embrittlement at this temperature.

3.2.4 Progress and Status

Five rod samples made from 20%-cold-worked type 316 stainless steel welded with 16-8-2 filler metal were included in experiment HFIR-CTR-16, designed to investigate irradiation effects at about 55°C, the

lower bound operating temperature for a separately cooled fusion reactor first wall. After irradiation these samples were tensile tested in air.

Location of fracture positions on post-test photomacrographs and comparison with weld locations determined by ferrite zone locations before irradiation showed that all weld specimens tested had failed within the weld metal. (The sample tested at 700°C failed very close to the weld-base metal interface). Mechanical properties of these specimens were reported in the last quarterly[1] and are repeated in Table 3.2.1 for reference.

Fracture surfaces of these tested samples have been examined by scanning electron microscopy to determine the failure mode. All the samples tested at 35°C, unirradiated and irradiated, showed fully ductile fracture surfaces. These all had failed in the "cup and cone" morphology. The central part of the fracture was approximately perpendicular to the tensile axis, and was covered with roughly equiaxed ductile dimples. The shear lips on these fractures were inclined at an angle to both the central part of the failure and the tensile axis. These surfaces too showed the dimples characteristic of ductile fracture. An overall view of the sample irradiated at about 55°C, to produce 8.7 dpa and 250 at. ppm He, and then tested at 35°C is shown in Fig. 3.2.1(a). This sample had failed after 5.8% uniform elongation and 11.8% total elongation. Reduction of area at the fracture was about 73%. Figures 3.2.2(a) and 3.2.3(a) show the fracture surface at *two* different magnifications.

The irradiated sample tested at 300°C had failed after 3.1% uniform elongation and 6.7% total elongation. This sample had failed on a single shear plane, which made an angle near 45" with the tensile axis. Figures 3.2.1(b) and 3.2.2(b) show the general appearance of this fracture, and Fig. 3.2.3(b) shows a higher magnification view. The entire fracture surface is covered with shallow dimples characteristic of ductile shear failure. Reduction of area at the fracture was approximately 34%.

The weld irradiated at 55°C and tensile tested at 700°C showed much less ductility. Uniform elongation was 1.4%, total elongation,

Table 3.2.1. Tensile Properties and Fracture Model of Welds Made With 16-8-2 Filler Metal Joining Type 316 Stainless Steel Base Metal

Irradiation Parameters[a]		Test Temperature (°C)	Strength, MPa		Elongation, %		Approximate Reduction of Area (%)	Fracture Made
(dpa)	Helium (at. ppm)		0.2% Yield	Ultimate	Uniform	Total		
0		~35	354	547	14.0	19.0	77	All ductile fracture, dimple rupture on classical cup and cone geometry
0		~35	333	510	12.9	16.5	80	
~4.5	100	~35	680	735	6.8	12.0	66	
8.7	250	~35	701	739	5.8	11.8	73	
10.8	340	~35	727	759	7.2	13.0	69	
10.8	340	300	565	598	3.1	6.7	34	Ductile fracture on about 45° shear plane
5.5	130	700	216	247	1.4	1.7	0	Intergranular separation.

[a] Irradiation temperature about 55°C.

1.7%. Figure 3.2.1(c) showed that the fracture had occurred without measurable necking, on a plane perpendicular to the stress axis. The fracture surfaces, Figs. 3.2.2(c) and 3.2.3(c), showed that the fracture had occurred totally by intergranular separation. The fracture surface does not show any indication of localized ductility.

3.2.5 Conclusions and Future Work

Irradiation of weld-containing samples at about 55°C to fluences producing 4 to 11 dpa and 100 to 340 at. ppm He resulted in large strength increases in tensile tests at about 35°C but had little effect on the ductility. The ductility was lower in tests at 300 and 700°C. The strength of 16-8-2 welded specimens remained lower than the strength of the 20%-cold-worked base metal, with all tested samples failing in the weld zone.

Fractures in tests at 35°C were of the cup-and-cone geometry, with surfaces covered with ductile dimples. The sample tested at 300°C had failed on a single shear plane, again with ductile dimples covering the fracture surface. The sample tested at 700°C had failed by intergranular separation, indicative of helium embrittlement at this temperature.

Similar specimens containing welds with 16-8-2 and type 316 stainless steel filler metal have been irradiated at temperatures in the

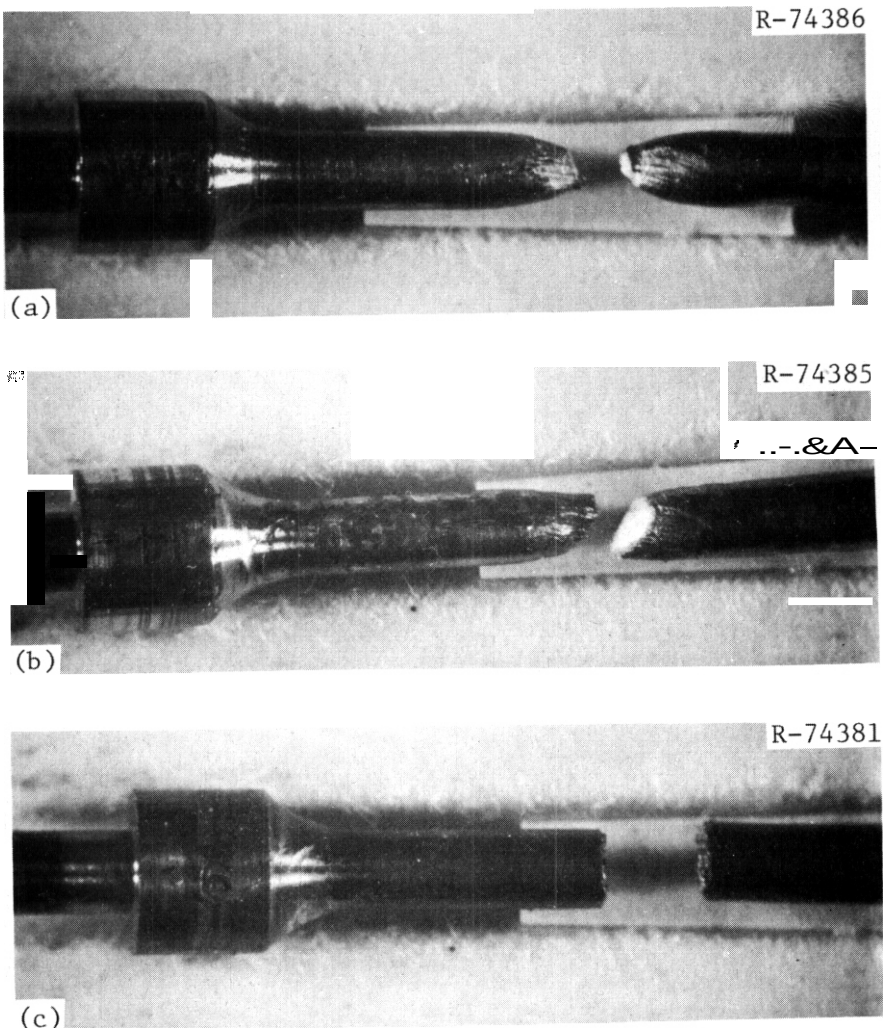

Fig. 3.2.1. Photomacrographs of Irradiated and Tested Stainless Steel Specimens Containing Sections of Welds Made with 16-8-2 Filler Metal. The samples were irradiated at about 55°C and tested at (a) about 35°C, (b) 300°C, and (c) 700°C.

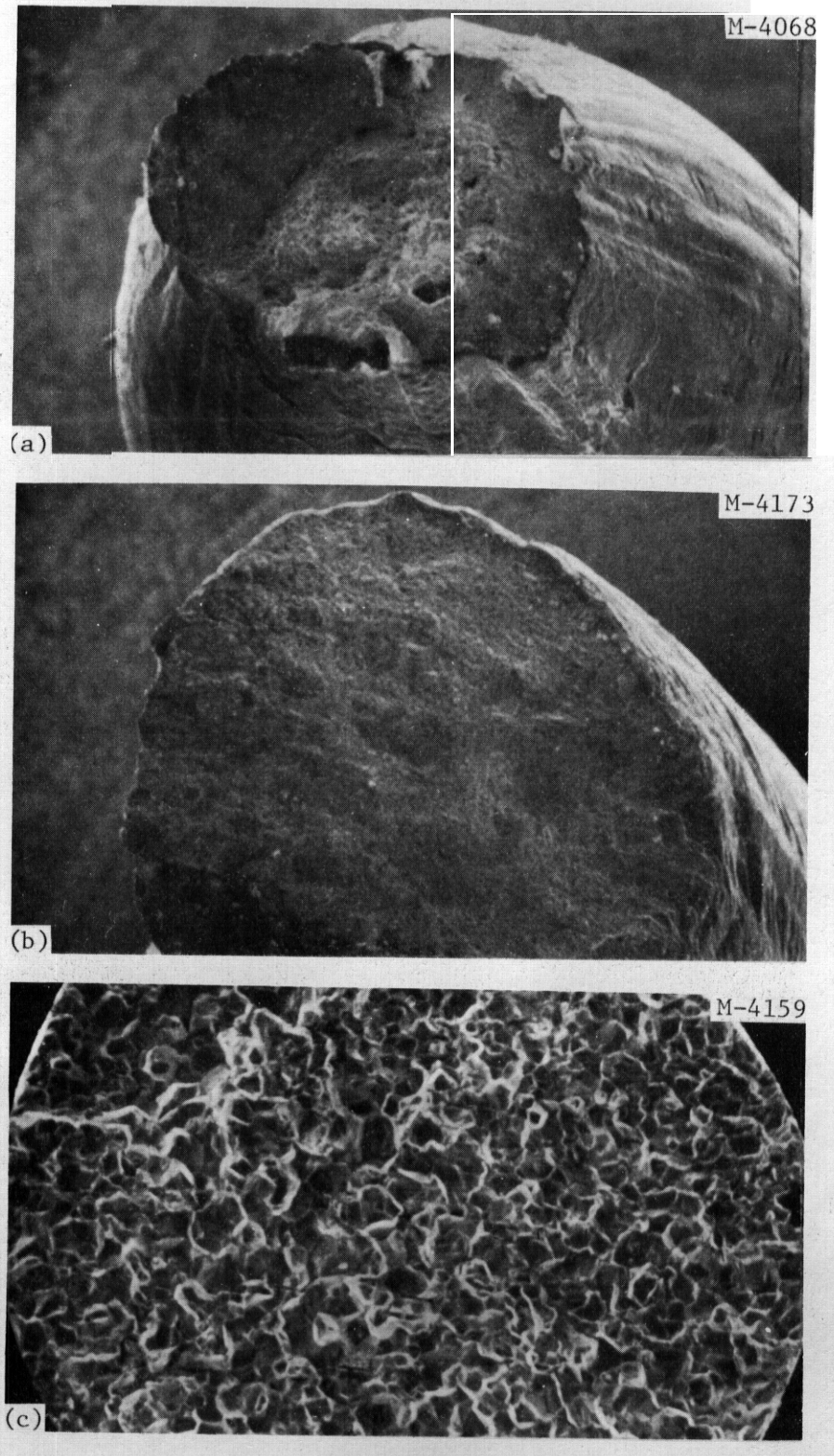

Fig. 3.2.2. Scanning Electron Micrographs of Fracture Surfaces of Welds Made with 16-8-2 Filler Metal. 50×. Samples were irradiated at about 55°C and tested at (a) about 35°C, (b) 300°C, and (c) 700°C.

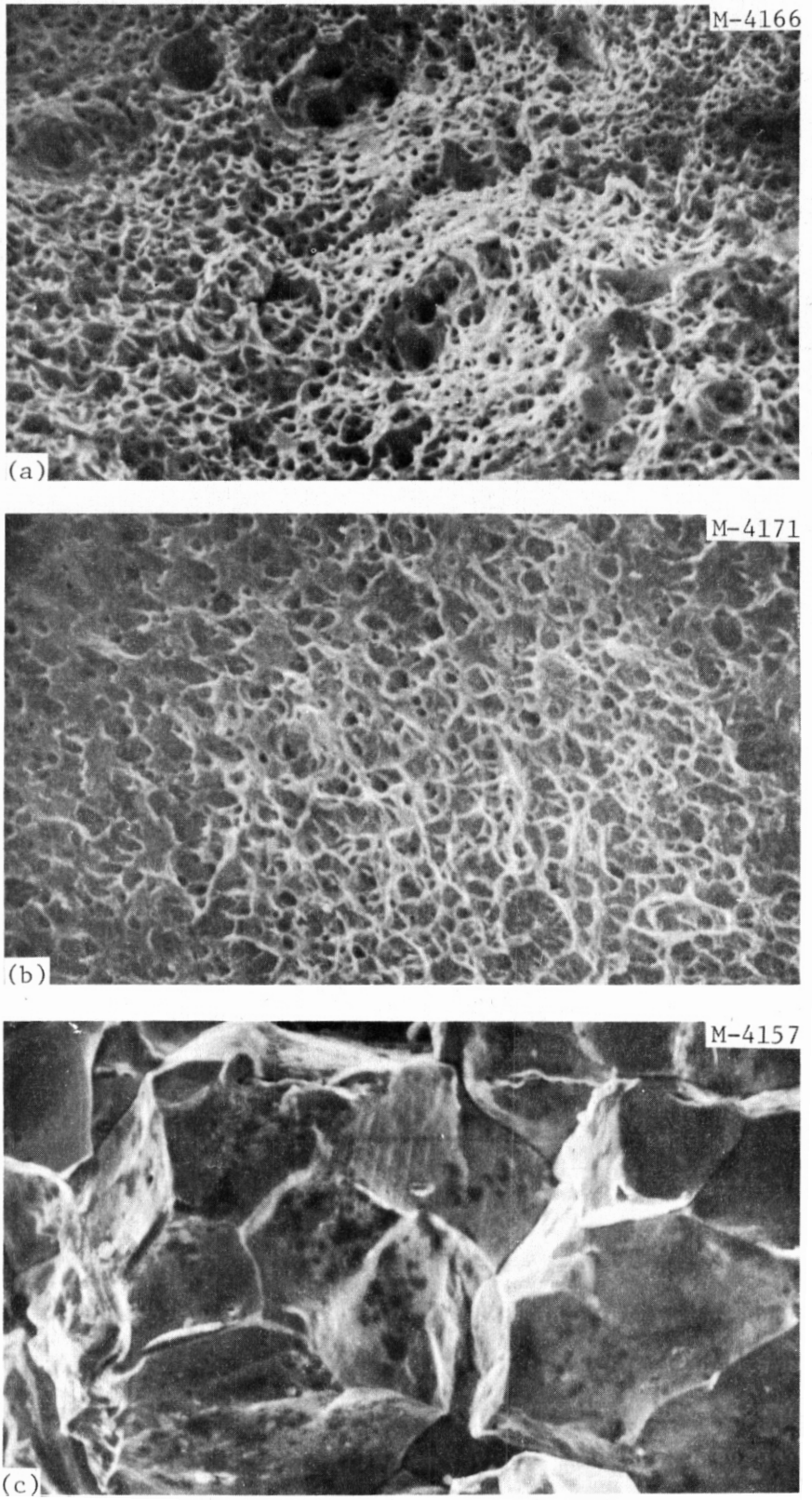

Fig. 3.2.3. Segments of the Same Fracture Surfaces as in Fig. 3.2.1. 500×.

range 280 to 620°C. These samples are being tensile tested. A related set of weld-containing and all-weld-metal sheet samples is under irradiation in ORR-MFE-1.

3.2.6 Reference

1. F. W. Wiffen, D. P. Edmonds, J. F. King, and J. A. Horak, "The Influence of Irradiation on the Properties of Path A Alloy Weldments," *ADIP Quart. Prog. Rep. March 31, 1977,* DOE/ET-0058/1(78), pp. 86–88.

3.3 STATUS OF FATIGUE TESTING FACILITY — K. C. Liu and M. L. Grossbeck (ORNL)

3.3.1 ADIP Task

Task I.B.l. Fatigue Crack Growth In Austenitic Alloys.

3.3.2 Objective

The objective of this effort is the development and application of a mechanical testing apparatus for use in testing irradiated specimens remotely in a radiation-shielded cell. The system is capable of performing a variety of mechanical property experiments in air or vacuum at elevated temperature under programmed loading histories.

3.3.3 Summary

The fatigue testing system has been completed and tested in the operating area outside the hot cell. Satisfactory performance has been demonstrated for a series of out-of-cell tests at elevated temperatures in vacuum. The system is being reassembled in the hot cell.

3.3.4 Progress and Status

An electro-hydraulic closed-loop controlled fatigue tester capable of testing irradiated samples at elevated temperatures in high vacuum has been installed in a hot cell. Figure 3.3.1 shows a general view of the testing facility; a part of the load frame and the load column assembly partially enclosed in a vacuum chamber are seen through the lead-glass window. The system is operated remotely by the electronic control console near the operating area outside the hot cell, also seen in Fig. 3.3.1.

The load frame is a four-column model with a 223 kN (50,000 lb) capacity. The machine has a hydraulic system capable of applying 58 kN (13,000 lb) to the load train at specimen strain rates ranging from 0.0001 to l/s comfortably exceeding all anticipated requirements for testing miniature irradiated specimens. The system is equipped with a function generator capable of providing sine, square wave, and ramp

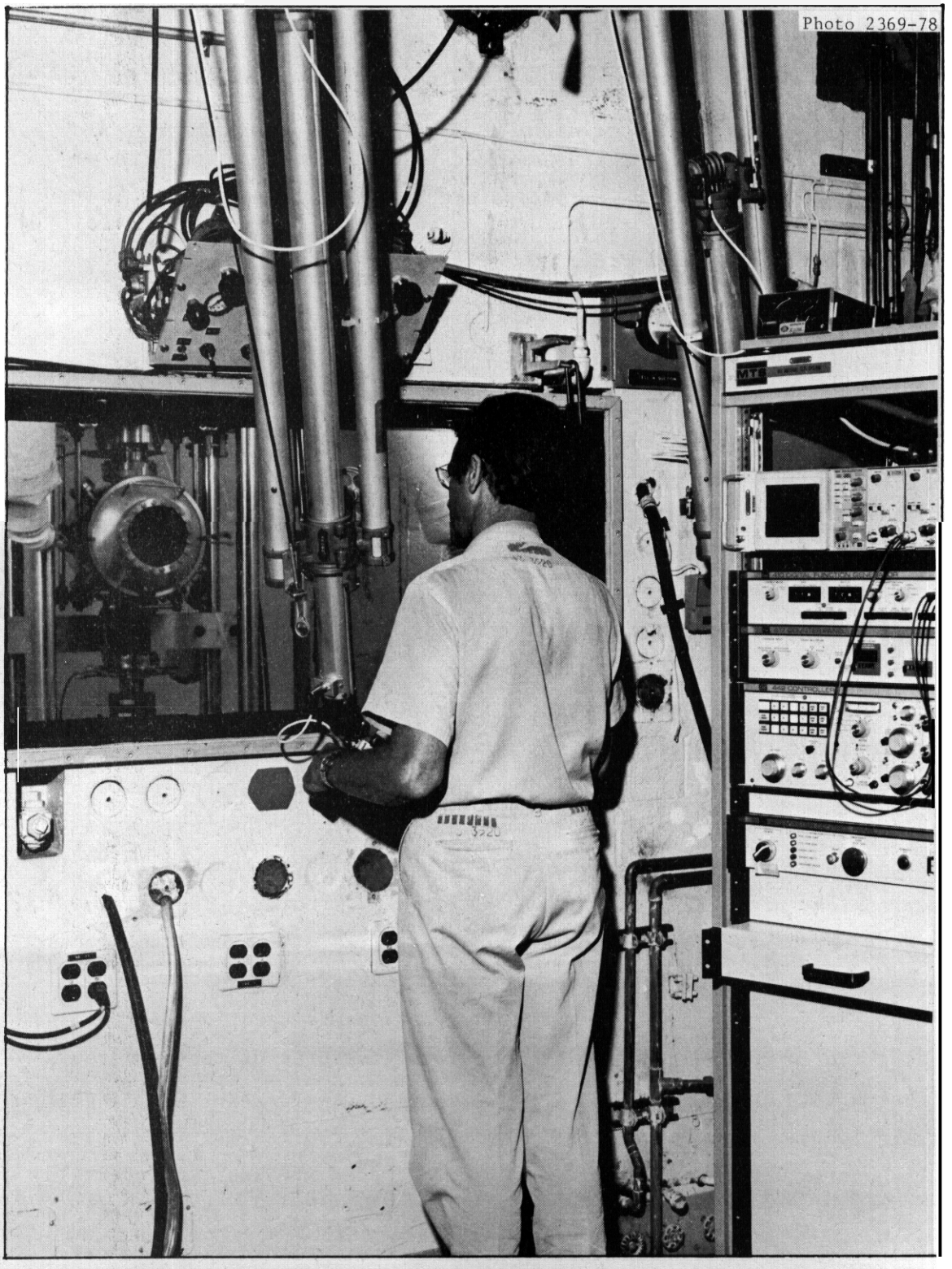

Fig. 3.3.1. General View of Fatigue Testing Facility.

functions combined with hold periods. Strain is measured by a high-temperature extensometer to enable strain controlled low cycle fatigue tests.

Elevated temperatures are achieved by induction heating with an rf generator provided with a temperature control system. Tests of the system have demonstrated its capability to heat the sample to any desired temperature within the range of consideration for fusion reactor materials.

The vacuum chamber is sealed to the hydraulic actuator rod by stainless steel bellows, so the chamber is completely bakeable. It is pumped by a 1.5 m^3/s turbomolecular pump. In preliminary tests, pressures down to 0.1 mPa have been achieved without a system bakeout. Since this vacuum is adequate for elevated-temperature testing of stainless steels, for ease of remote operation, a bakeout will not be used for stainless steels. However, if we want to test refractory metals and titanium, it is estimated that a pressure of 0.1 μPa can be attained after a system bakeout.

To evaluate system performance, a series of tests on miniature irradiation fatigue specimens was conducted in both air and vacuum. The tests were performed only to evaluate the testing system performance and not to characterize the materials tested. The tests were controlled by the axial strain, fully reversed in tension and compression, with the strain amplitudes from 0.2 to 2%. The axial strains were interpreted from the outputs of the diametral extensometer through the strain computer module in the test system. A symmetric triangular function beginning with compression was used in all the tests. To capture the essential behavioral features of the hysteresis stress-strain relationship at the early stage of cyclings, the stress-strain loops were recorded continuously only for a few initial cycles. Subsequently, the hysteresis loops were recorded at discrete intervals as necessary to observe the changes. Concurrently, the stress and strain were recorded separately by a strip chart recorder on a continuous time basis. Information between two recordings of the hysteresis loops was therefore supplemented.

None of the specimens buckled before failure by complete separation. Excellent performance of the test machine was demonstrated. The test data fell slightly below the average trend curves of BMI[1,2] and GE[3] test data. Direct comparisons cannot be made since our specimens were prepared from different heats and 20% cold worked. Nevertheless, the test data appeared to fall within the data scatter. Table 3.3.1 summarizes the results of six tests in vacuum. Test procedures used in these tests were essentially identical to those done in air. Again, tests were carried out to fatigue failure without buckling, except the last test, which was interrupted by a power failure. Vacuum test data fell above the average curve, as shown in Fig. 3.3.2 by a factor of about three to ten. This observation supports the argument that use of air fatigue data in estimating the lifetime of the fusion first wall may lead to an erroneous result.

Unlike out-of-cell testing, in-cell testing requires special tools and skills for remote handling of irradiated specimens and test preparation. These tools have been developed and fabricated. Several in-cell tests will be performed with unirradiated specimens before irradiated specimens are tested.

Table 3.3.1. Cyclic Fatigue Life of 20%-Cold-Worked Type 316 Stainless Steel Tested in Vacuum at 300°C at a Strain Rate of 0.004/s[a]

Specimen	Nominal Diameter (mm)	Axial Strain Amplitude (%)	Vacuum (mPa)	Number of Cycles to Failure N_f
G4	3.175	1.0	5.7	3015
G2	3.175	0.5	4.9	33144
A92	3.175	0.3	4.6	68218
A97	3.175	0.3	5.2	38608
A71	3.175	0.5	5.0	10007
A6	3.175	0.5	0.41	1290[b]

[a] Nominal specimen diameter 3.175 mm.

[b] Specimen damaged by disruption of power; test discontinued.

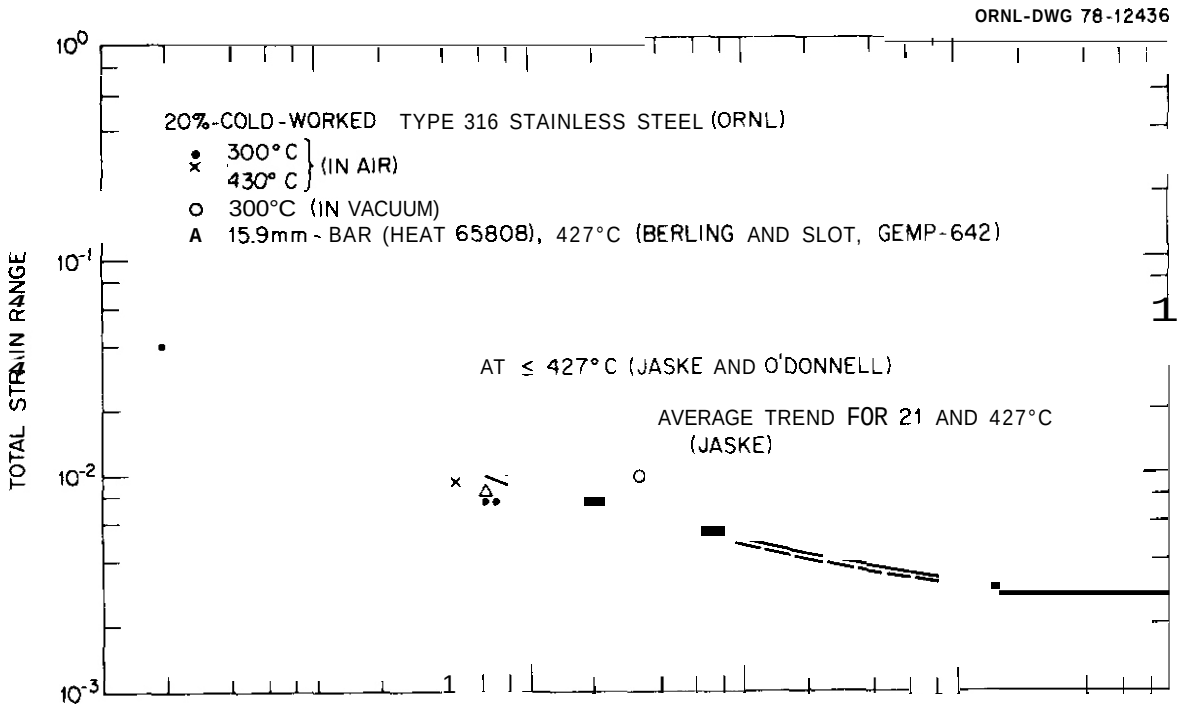

3.3.5 Conclusion

The electro-hydraulic fatigue testing system designed for use in testing irradiated specimens by remote operation has been installed in a radiation-shielded cell and is operational. Several in-cell tests will be done with unirradiated specimens before irradiated samples are tested. This will be a final checkout and also an opportunity for hot-cell operating personnel to become familiar with the operating procedures.

3.3.6 References

1. R. I. Jetter and F. V. Naugle, *Quarterly Technical Progress Report High-Temperature Piping Design Technology April-June 1977*, AI-ERDA-13206 (August 1977), p. 18.

2. C. E. Jaske and W. J. O'Donnell, "Fatigue Design Criteria for Pressure Vessel Alloys," Presented at the Energy Technology Conference and Exhibition, Houston, Texas, Sept. 18–22, 1977; ASME Paper 77-PVP-12, 1977.

3. J. T. Berling and T. Slot, *Effect of Temperature and Strain Rate on Low Cycle Fatigue Resistance of AISI 304, 316, and 348 Stainless Steels*, GEMP-642 *(1968)*.

4. PATH B ALLOY DEVELOPMENT — HIGHER STRENGTH Fe-Ni-Cr ALLOYS

Path B alloys are the Fe-Ni-Cr "super alloys" in which tensile, creep-rupture, and fatigue strength levels higher than attainable in the austenitic stainless steels are achieved by precipitation of one or more phases. Many alloys in this class exhibit low swelling in fast-reactor irradiations. The technology for use of path B alloys in neutron radiation environments is not as advanced as for path A alloys. A basis to select a specific alloy type for further development is lacking. Accordingly, the ADIP task group has selected five base research alloys that are representative of the basic systems of path B alloys and deserve consideration for fusion reactor applications. The systems under investigation include γ' strengthened-molybdenum modified, γ' strengthened-niobium modified, $\gamma'\gamma''$ strengthened, and a high-nickel precipitation-strengthened alloy (~75% Ni).

Near-term activities are focused on evaluating the effects of a fusion reactor neutron spectrum on key mechanical and physical properties. Damage created by the fusion reactor neutron spectrum is approximated by fission reactor irradiation. Data are presently being obtained on a limited number of commercial alloys on which scoping studies were initiated two to three years ago. The emphasis will shift to the base research alloys as they become available. For those properties that are either inadequate or degraded to an unacceptable level, the influence of composition and microstructure on the response will be examined. The research program will be oriented toward determination of mechanisms responsible for the observed property changes and the effects of metallurgical variables on the response. The objective is to develop a basis for selection of the path B prime candidate alloy(s).

4.1 THE RESPONSE OF INCONEL 600 TO SIMULATED FUSION REACTOR IRRADIATION — F. W. Wiffen (ORNL)

4.1.1 ADIP Tasks

ADIP Tasks I.C.3, Microstructures and Swelling in High-Strength Fe-Ni-Cr Alloys, and I.B.14, Tensile Properties of High-Strength Fe-Ni-Cr Alloys.

4.1.2 Objective

High Flux Isotope Reactor (HFIR) irradiations were conducted to investigate radiation effects in nickel-base alloys under conditions of high helium production rates accompanying the production of displacement damage. Inconel 600, chosen as a typical solid-solution-strengthened nickel alloy, has demonstrated swelling resistance under a limited range of irradiation conditions.[1,2] The goals of these experiments were: (1) to investigate swelling under conditions of concurrent displacement damage and transmutation helium production, (2) to examine tensile properties of these irradiated materials as a function of irradiation and test temperatures. Samples of Inconel 600 were included both as solution annealed and 20% cold-worked.

4.1.3 Summary

Inconel 600 was irradiated in HFIR at 55 to 700°C to investigate swelling and postirradiation tensile properties as functions of irradiation and test temperature under conditions of concurrent displacement damage and helium production. Helium contents from 600 to 1800 at. ppm and displacement levels of 4 to 9 dpa were achieved, and the results were used to estimate performance in a fusion reactor environment. The swelling was weakly dependent on temperature between 300 and 600°C, with swelling ranging from 0 to about 1%, but increased rapidly above 600". The swelling values were much larger than expected from fast reactor and ion bombardment results. Cold work did not suppress swelling of Inconel 600. Tensile property measurements and fractography on the same samples showed that strength values increased

for irradiation at 55 to 400°C but decreased below unirradiated values for irradiations at 600 and 700°C. Elongation values were lowest at the temperature extremes. Total elongations below 1% were found only for irradiation and test temperatures of 600 and 700°C. The fractures were completely transgranular for samples irradiated and tested at 300 and 400°C, of mixed mode but predominantly intergranular at 500°C, and fully intergranular at 600 and 700°C. The results suggest that Inconel 600 does not offer any advantages over type 316 stainless steel and does not warrant further development for fusion reactor application.

4.1.4 Progress and Status

Table 4.1.1 gives a number of parameters for comparison of the response of Inconel 600 in a proposed fusion reactor to the response in the Experimental Breeder Reactor-II (EBR-II) and in HFIR. Both fission reactors provide a higher total neutron flux and also higher rates of atom displacements than for the same alloy in a Tokamak at a nominal neutronic wall loading of 1 MW/m^2. The two fission reactors produce hydrogen from (n,p) and similar reactions at approximately the same rate as the Tokamak with the power level listed. If defect production rates are compared in combination, however, the hydrogen production rate is too low. The ratio of at. ppm hydrogen/dpa for a fusion reactor is 104; for the two fission reactors this ratio is only 30 and 48. It is suspected that these differences are not of primary importance.

Helium is known to have a major effect on the irradiation response of metals, and must be treated as thoroughly as possible in predicting irradiation effects in future power systems. In this regard, the two fission reactors are quite different. EBR-II produces too little helium to simulate fusion reactor conditions, and in HFIR the nonlinear helium production rate soon results in too much gas. The ratio of at. ppm helium/dpa is 29 for a fusion reactor and is constant with service time in this system. In EBR-II the ratio is 2.1, also constant with time. In HFIR this ratio is much higher and is time-dependent. After 100 days of irradiation, the ratio is 235; after one year it has increased to 345.

Table 4.1.1. Radiation Effects Parameters for Inconel 600 in a Tokamak, EBR-II, and HFIR

	Tokamak Fusion Reactor[a]	EBR-II[b]	HFIR[b]
Location	First wall	Midplane, row 2	Midplane, PTP
Power level	1 MW/m^2	62.5 MW(th)	100 MW(th)
Neutron flux, n/m^{2}s			
~14 MeV	6.85×10^{17}	0	0
>0.1 MeV	2.58×10^{18}	21×10^{18}	14×10^{18}
Total	3.62×10^{18}	25×10^{18}	52×10^{18}
Displacements per year,[c] dpa	12	41	33
Hydrogen per year,[c] at. ppm	1,250	1,240	1,580
Helium,[c] at. ppm			
100 d	94	24	2,130
1 year	343	87	11,400

[a] Calculations from reference 3.

[b] Calculation from reference 4.

[c] All calculations are for a plant factor of 100%.

The result of these considerations is that in Inconel 600 processes that are driven solely by dpa level can be adequately simulated in either HFIR or EBR-II. Processes driven solely by helium production can best be simulated in HFIR. For most processes, however, the ratio of helium to displacement level is likely to be important. For these cases, then, the properties after irradiation in HFIR and EBR-II provide extremes that can be used to fit correlation models in predicting fusion power reactor service.

4.1.4.1 Experiment

The rod specimens of Inconel 600 had a gage section 2 mm in diameter and 18 mm long.' Samples to be irradiated with a solution annealed microstructure were annealed in an argon atmosphere for 4 h at 1080°C and then furnace cooled.

One of the 11 specimen positions in a typical HFIR-PTP elevated-temperature irradiation experiment is shown schematically in Fig. 4.1.1. The specimen is centered by a hub with integral fins. The temperature drop from the specimen irradiation temperature to the reactor coolant temperature is taken across the centering spur on the

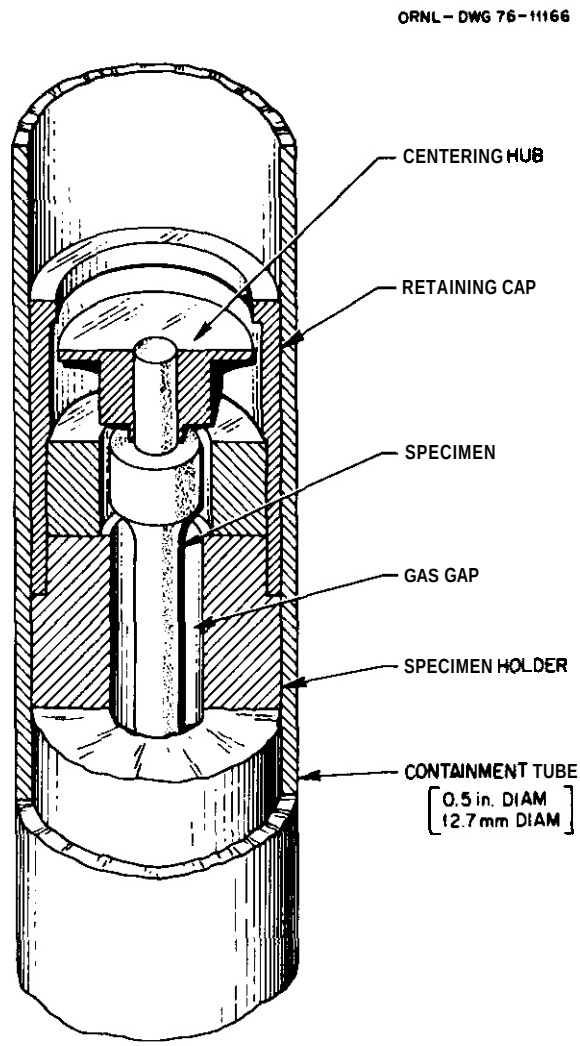

Fig. *4.1.1.* A Schematic Section Through a Typical Specimen Position in an Elevated-Temperature HFIR–PTP Experiment. The specimen overall length is *39.4* mm (1.55 in.), and the maximum diameter at the buttonhead is *4* mm (0.16 in.). The gage section is 2 mm diam by 18 mm long.

ends of the sample, the centering hub, and fins. The irradiation temperature at each position is fixed by the width of the gas gap between specimen and holder and by the geometry of the centering fins.

A few samples of Inconel 600 were irradiated in the same reactor position at a temperature near 55°C. These samples were held in place in perforated tubes, with the samples in direct contact with the cooling water.

4.1.4.2 Results

The swelling data obtained in these experiments are given in Table 4.1.2. Irradiation parameters listed include temperature, fast-neutron fluence, dpa level, and helium content. The displacement damage (dpa) was calculated[4] for the HFIR-PTP neutron spectrum by use of the IAEA Working Group recommended model. The helium content was calculated from correlations developed[5] for helium production in ^{58}Ni irradiated in HFIR.

Table 4.1.2. Swelling of Inconel 600 Irradiated in HFIR

Irradiation Conditions				Swelling, %			
				Solution Annealed		20% Cold-Worked	
Temperature (°C)	Fluence >0.1 MeV (10^{25} n/m^2)	Displacement Level (dpa)	Helium (at. ppm)	Density Decrease	Geometry $3\Delta L/L$	Density Decrease	Geometry $3\Delta L/L$
55	5	4.5	670	0.38	0.1		
55	9.6	7.3	1470	0.21	0.2		
55	13.6	10.9	2670	0.25	0.3		
55	12.4	10.0	2220			a	0.2
300	5.3	4.3	650	0.34	−0.23	0.12	0.08
300	9.7	7.9	1560	0.30	0.19		
400	5.6	4.4	670	0.23	−0.02	−0.04	−0.12
400	8.5	7.0	1270	0.48	0.25		
500	7.0	5.9	970	0.23	0.31	0.41	−1.28
500	10.4	8.5	1760	0.85	0.50		
600	7.5	5.9	970	0.61	0.87	0.63	1.45
600	9.9	8.1	1640	1.13	0.72		
650	10.6	8.7	1840	2.60	a		
700	8.8	7.0	1300	2.36	a	1.51	a
700	10.4	8.5	1770	3.88	a		

[a] Not available

Swelling determined by immersion density measurements showed a consistent pattern and thus is assumed to be quite reliable. The results will, however, be compared with microstructural evaluation when transmission electron microscopy is completed.

Swelling in Inconel 600 ranged from 0 to almost 4% for the irradiation conditions examined. The results in Table 4.1.2 are shown graphically as a function of irradiation temperature in Fig. 4.1.2. The data in Fig. 4.1.2 are shown with helium levels indicated but are plotted without regard to fluence differences in different samples. Inspection of these data shows the following:

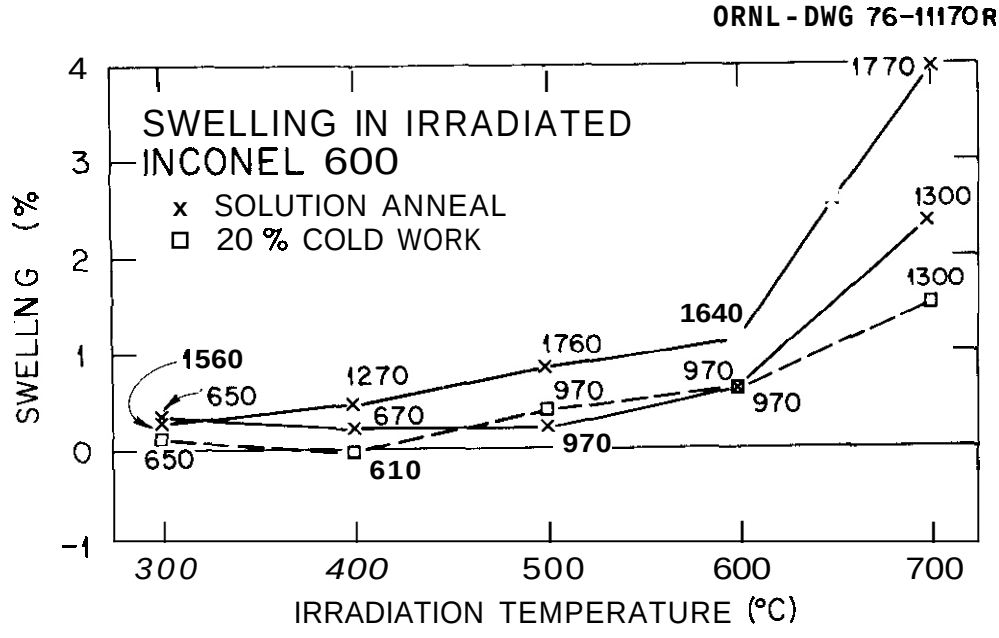

Fig. *4.1.2.* Measured Density Decrease for Inconel 600 Specimens Irradiated in the HFIR. Irradiation at the indicated temperatures produces *4* to *9* dpa, and the helium content, in at. ppm, shown at each datum.

1. Swelling values are very high for the dpa level. This establishes immediately that the helium production rates calculated for fusion reactors will result in swelling rates in Inconel 600 much greater than predicted by results obtained from nickel ion bombardment and from fast reactor neutron irradiation studies.

2. Swelling in Inconel 600 increases as the helium content increases, for a fixed irradiation temperature. The exceptions to this, at 55 and 300°C, may reflect only the uncertainty in measurement of these small swelling values.

3. Cold-working Inconel 600 is not very effective in suppressing swelling during irradiation with high helium production rates.

4. Swelling under these irradiation conditions depends only weakly on temperature for irradiations between about 55 and 600°C but increases markedly for irradiations at 650 and 700°C.

The Inconel 600 data would be more useful if they could be normalized, *so* some consideration was given to a possible method of accounting for the different fluences at each irradiation temperature.

The simplest assumption that can be made is that swelling at a fixed irradiation temperature is controlled by the helium content alone. If we further assume perfect gas law behavior and a constant concentration of equilibrium helium bubbles containing all the gas, then swelling (S) will be proportional to the 3/2 power of of the helium concentration (C_{He}):

$$S \propto C_{He}^{3/2} .$$

The swelling data were normalized with this assumption to the average helium value of the high-helium-content data. The normalized values are shown graphically in Fig. 4.1.3. They reinforce the conclusions drawn earlier on the temperature dependence of swelling.

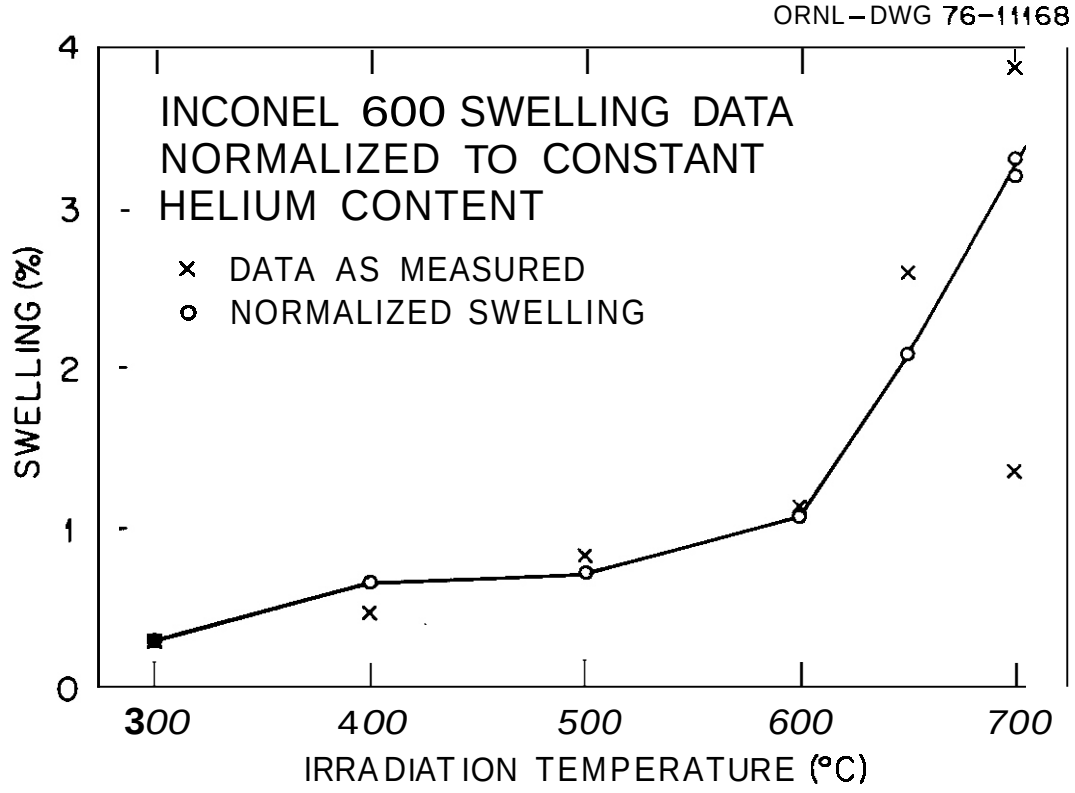

Fig. 4.1.3. Swelling of Solution Annealed Inconel 600 Normalized to an Average Helium Content of 1541 at. ppm. The normalization assumed that all swelling was due to helium bubbles, that helium behaves like an ideal gas, and that for small variations in helium content the bubble concentration at any temperature remains constant.

The microstructure in samples solution annealed and then irradiated at 400 and 650°C are shown in Fig. 4.1.4. Irradiation at 400°C produced cavities with diameters in the range 4 to 17 nm but few cavities at the upper end of this size distribution. These cavities were uniformly distributed throughout the sample, with grain boundary regions neither depleted nor enhanced in cavity population. The dislocation structure in this sample was a high concentration of tangled loops and networks. Cavities in the sample irradiated at 650°C were considerably larger, with the range of diameters of matrix cavities 45 to 290 nm and with larger than average cavities on grain boundaries. This sample also contained a moderate concentration of network dislocations.

The tensile properties for all tested samples and for control samples tested in the hot cell are given in Table 4.1.3. Most of the irradiated samples were tested at the same temperature as the design irradiation temperature. The properties for the 20%-cold-worked Inconel 600 are plotted against test temperature in Fig. 4.1.5(a). Values for unirradiated samples of the same material, tested in the hot cells under conditions identical to the irradiated sample tests, are plotted for comparison on the same graph. Figure 4.1.5(b) gives the properties of Inconel 600 irradiated in the solution annealed condition and gives handbook values for hot-rolled Inconel 600 rod. A few samples irradiated at about 55°C were tested at higher temperatures. The results of these tests are given in Fig. 4.1.6.

Strength values for the irradiated material show a much greater dependence on irradiation and test temnerature than for the unirradiated material. Irradiation and testing at 55 to 400°C produce strength values that exceed both the yield and ultimate strength of control specimens. Uniform and total elongations are well below the control specimen values. At higher temperatures the strength values for irradiated samples fall below the control values. The strength of 20%-cold-worked material irradiated at 700°C was only about 20% that of the control. In both cold-worked and solution annealed material the irradiated matetial was less ductile at high and low temperatures than at the intermediate temperatures.

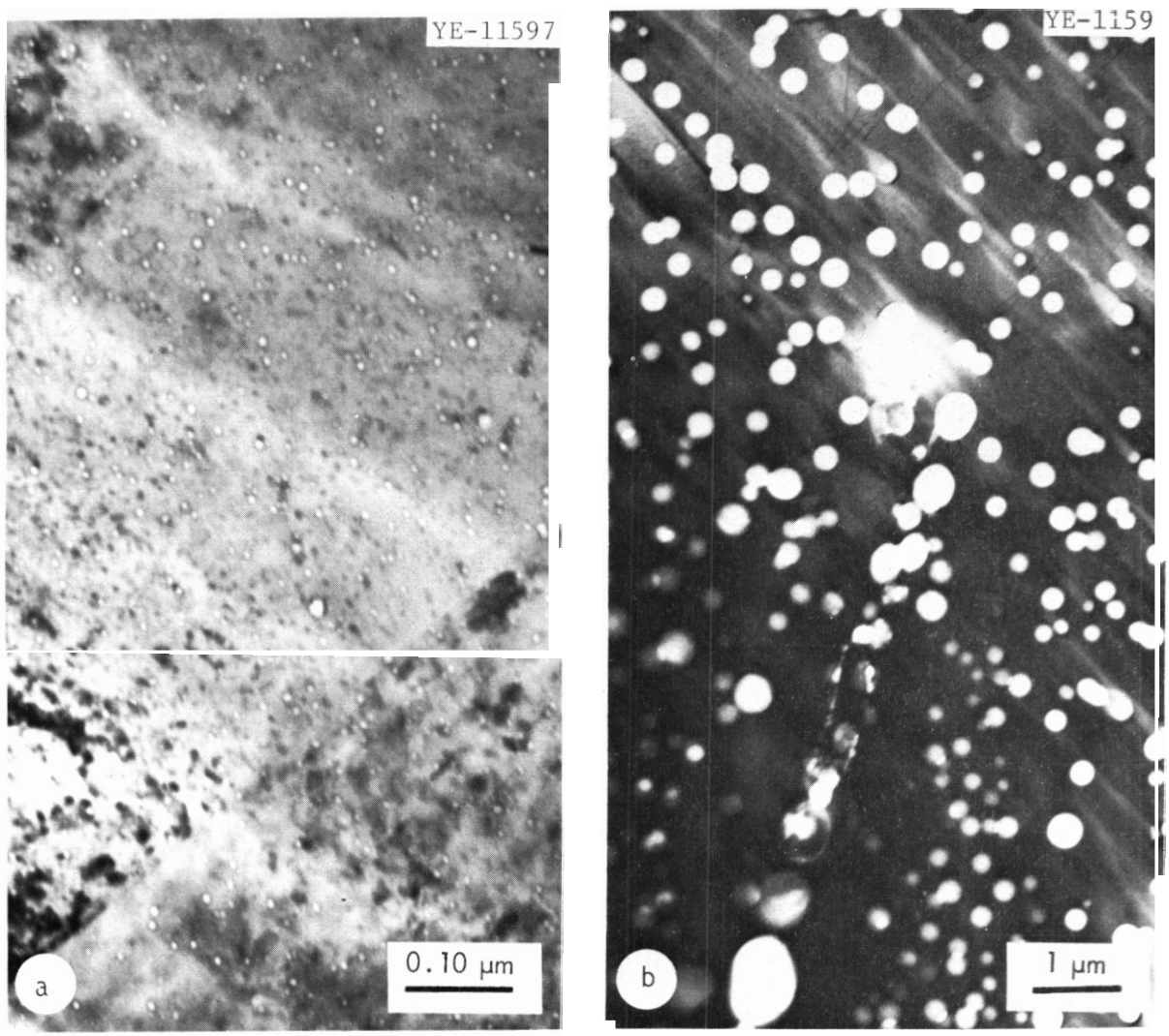

Fig. *4.1.4.* **Microstructures in Inconel** *600,* **Solution Annealed Before Irradiation. Note difference in magnification. (a) Irradiated at 400°C to** *7.0* **dpa and** *1270* **at. ppm He. The swelling was** *0.48%.* **(b) Irradiated at 650°C to** *8.7* **dpa and** *1840* **at. ppm He. Swelling** *2.6%.*

Tensile 4.1.3. Tensile Test[a] Results for Inconel 600 Irradiated in HFIR

Irradiation			Tensile Test Temperature (°C)	Stresses, MPa (ksi)		Elongation, %	
Temperature (°C)	dpa	He (at. ppm)		YS[b]	UTS	ε_{unif}	ε_{total}
			Cold Worked 20% Before Irradiation				
	Control		35	600 (87.1)	725 (105.1)	14.9	20.7
	Control		300	540 (78.38)	700 (101.57)	15.5	19.2
	Control		400	524 (76.0)	708 (102.7)	20.9	26.1
	Control		500	486 (70.48)	671 (97.35)	24.3	25.1
	Control		600	472 (68.4)	634 (92.0)	13.6	16.3
	Control		700	439 (63.74)	453 (65.75)	1.3	14.2
55	10	2220	35	880 (127.7)	919 (133.3)	7.2	10.1
300	4.3	650	300	924 (133.96)	925 (134.16)	0.8	4.2
400	4.4	670	400	699 (101.4)	780 (113.2)	4.3	6.7
500	5.9	970	500	419 (60.79)	528 (76.54)	5.5	6.4
600	5.9	970	600	314 (45.6)	320 (46.4)	0.43	0.68
700	7.0	1300	700	85.9 (12.46)	85.9 (12.46)	0	0
			Solution Annealed Before Irradiation				
55	7.3	1470	35	856 (124.1)	857 (124.3)	0.17	13.7
55	7.3	1470	300	709 (102.9)	741 (107.4)	11.8	14.8
55	10.9	2670	300	638 (92.6)	716 (103.8)	17.2	20.2
55	4.5	670	600	518 (75.2)	536 (77.8)	.97	1.82
300	4.3	650	300	847 (122.9)	850 (123.3)	3.3	7.0
300	7.9	1560	300	871 (126.4)	877 (127.2)	1.1	1.6
400	4.4	670	400	609 (88.3)	716 (103.8)	8.7	10.0
500	5.9	970	500	324 (46.99)	385 (55.78)	3.3	3.7
500	8.5	1760	500	263 (38.1)	367 (53.2)	6.5	6.8
600	5.9	970	600	187 (27.1)	251 (36.4)	2.6	3.1
600	8.1	1640	600	150 (21.7)	159 (23.1)	0.6	0.8
700	8.5	1770	700	113 (16.32)	113 (16.32)	0	0

[a] All tests at nominal strain rate of 0.0028/min.

[b] 0.2% yield strength.

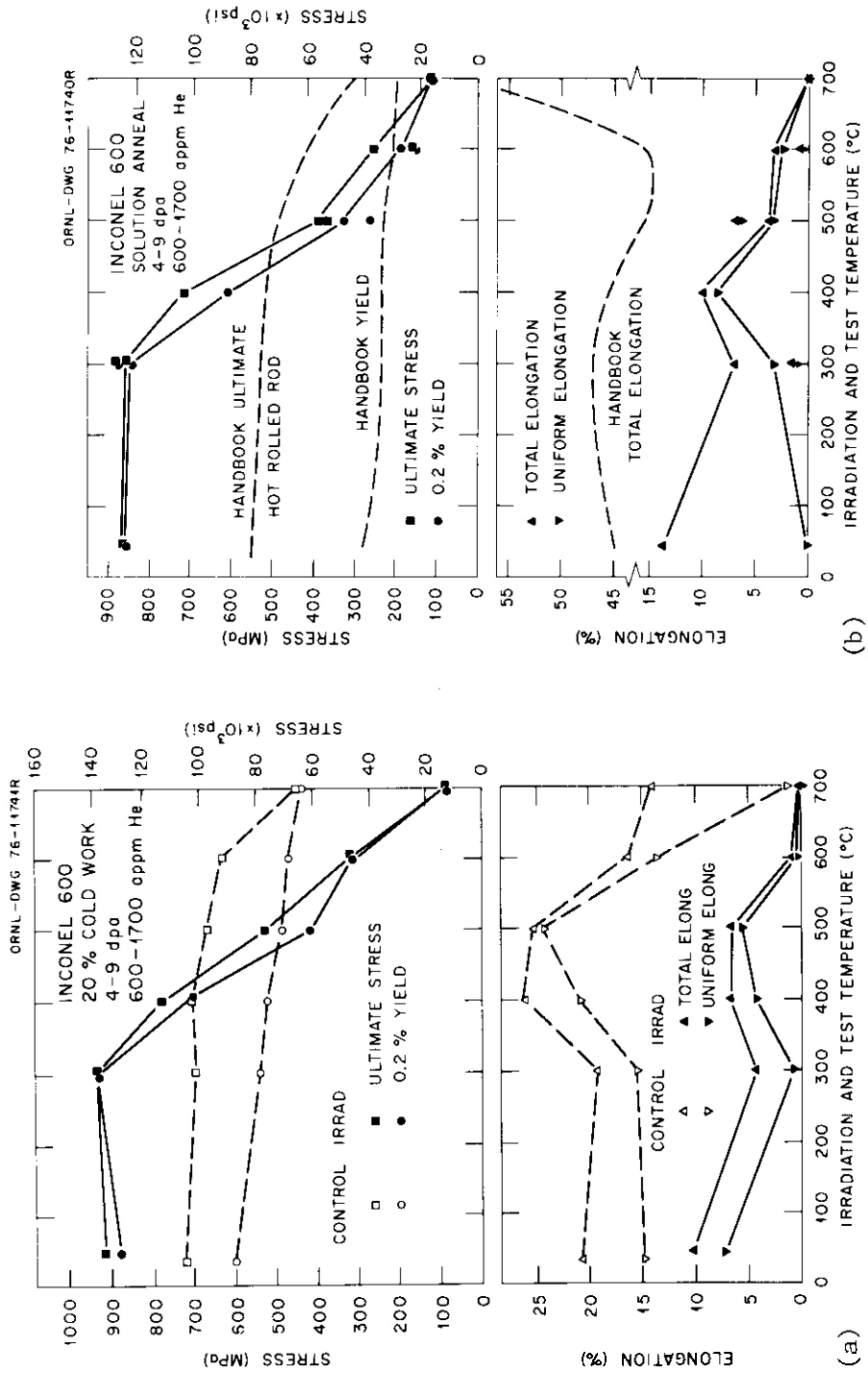

Fig. 4.1.5. Tensile Properties of Irradiated Inconel 600. Samples were irradiated and tested at the indicated temperatures. (a) Cold-worked 20% before irradiation. (b) Solution annealed 4 h at 1080°C before irradiation.

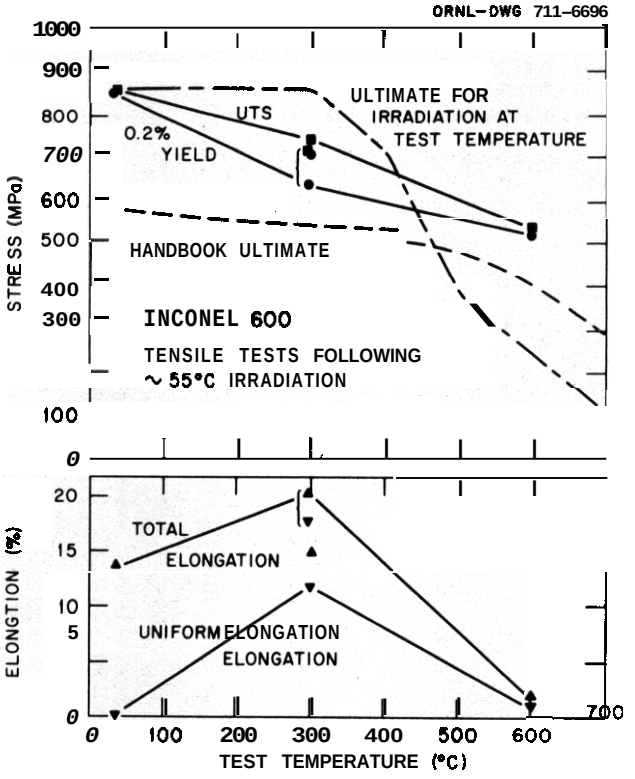

Fig. 4.1.6. Tensile Properties of Irradiated Inconel 600, Solution Annealed Before Irradiation. These samples were irradiated at about 55°C. They were held 30 min at the test temperature before test.

Comparison of Fig. 4.1.5(a) and (b) shows a great deal of similarity in the behavior of material either cold-worked or solution annealed before irradiation. The strength values of irradiated 20%-cold-worked material are consistently 80 to 140 MPa greater than for solution annealed material irradiated and tested at the same temperatures, for temperatures in the range 55 to 600°C. The ductility values, too, are closely similar for the two preirradiation microstructural conditions.

The effect of fluence on the irradiation response of solution annealed Inconel 600 appears to be a function of temperature. Strength increased and ductility decreased with increasing exposure for irradiation at 300°C. At 500 and 600°C strength decreased with increasing exposure. At 500°C higher fluence resulted in higher ductility but at 600°C the ductility decreased as fluence increased.

Fracture surfaces of the irradiated and tested 20%-cold-worked samples were examined by scanning electron microscopy. Representative fracture surfaces are shown in Fig. 4.1.7 and correlated with the total tensile elongation. Control samples and irradiated samples tested at 400°C or lower show features typical of a fully ductile fracture mode.

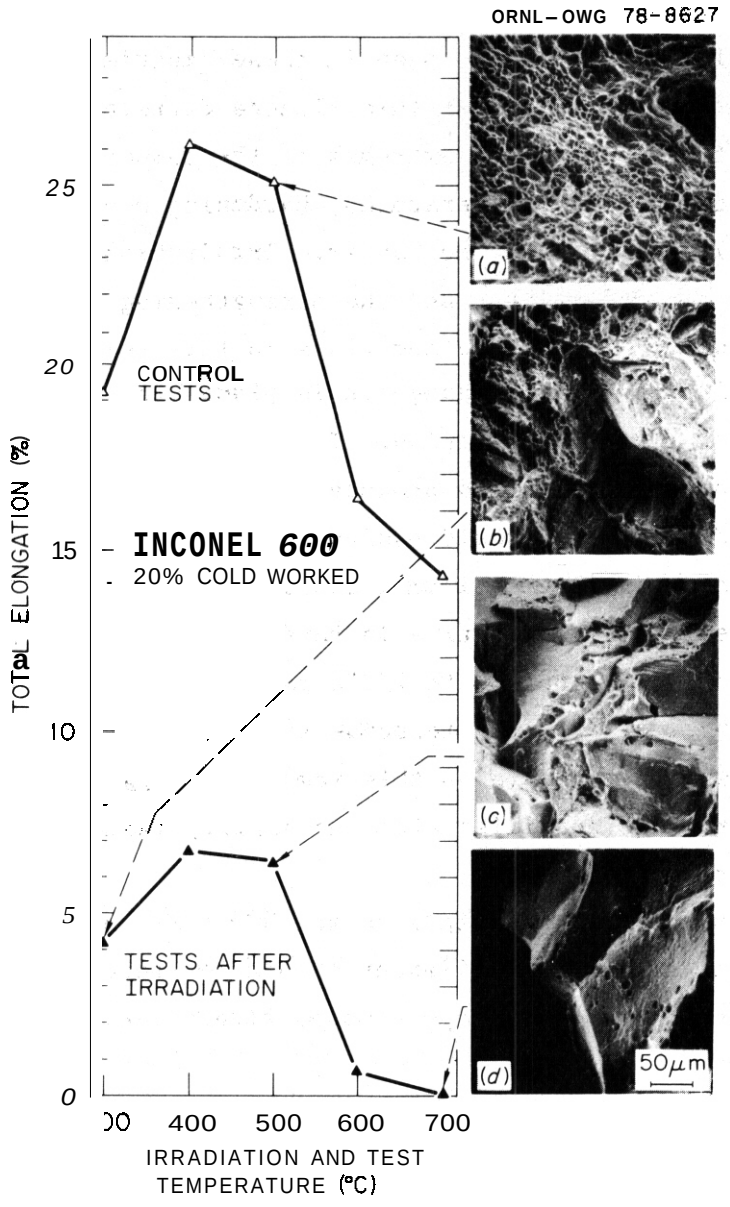

Fig. 4.1.7. Ductilities and Associated Fractographs for Inconel 600 20% Cold-Worked Before Irradiation.

The fractures were transgranular, with fracture surfaces largely covered with ductile dimples. Higher temperature fractures all exhibited some degree of grain decohesion. The fracture at 500°C was approximately 50% by grain boundary separation, with regions of tearing joining the exposed grain boundaries. At 600 and 700°C the failure was totally intergranular. Pore structures on grain boundaries of the sample tested at 700°C marked the sites of grain boundary helium bubbles in this sample. No evidence of the channel fracture mode observed6 in stainless steels was seen in these experiments.

These results suggest that at this fluence different mechanisms are dominant at the low and high extremes of the temperature range investigated. At the lower temperatures, hardening due to displacement damage is probably the dominant mechanism. Irradiation strengthens the matrix above the control values, and the strengthening increases as the dpa level increases. The role helium plays in this temperature range is not immediately apparent, although it is plausible that it enhances the rate of defect cluster nucleation. Irradiation in HFIR with high helium generation rate would thus produce a finer scale distribution of microstructural defects than would equivalent dpa level irradiation without the accompanying high helium production rates. The fine-scale damage would be especially effective in hardening the matrix.

For temperatures in the 600 to 700°C range the helium undoubtedly controls the mechanical property response to irradiation. The helium promotes intergranular fracture in this temperature range. This explains the decreasing ductility with increasing fluence (and hence increasing amounts of helium).

In the intermediate temperature range, $300 < T < 600$°C, both lattice hardening and helium embrittlement should be operative and a more complex dependence of tensile properties on fluence and temperature can be expected.

Samples irradiated at about 55°C and then tested at elevated temperatures showed a somewhat different behavior. For these samples, the strength in tests at 300°C was lower than for samples both irradiated and tested at 300°C. The ductility was lower for the samples irradiated

at the lower temperature. A test at 600°C of a sample irradiated at 55°C resulted in strength values higher than for samples both irradiated and tested at 600°C. The ductility was comparable to that in tests of samples irradiated at 600°C. Properties in tests at 300°C are probably controlled by matrix hardening from the irradiation-produced microstructure. Differences in strength for the two irradiation temperatures may reflect a greater stability of the microstructure to deformation at the temperature at which it was produced, compared with the lower stability of the microstructure produced at about 55°C and then tested at 300°C. The opposite strength effects at 600°C probably indicate that more of the helium produced at 600°C has reached grain boundaries than in samples irradiated at 55°C and then heated to 600°C for testing.

4.1.4.3 Discussion of Swelling

Irradiation-produced swelling in Inconel 600 ranged between 0 and 4% for the irradiation variables examined. The swelling was small, not over 1.0%, for irradiation temperatures between 55 and 600°C. In this lower temperature range, the swelling was slightly temperature dependent. In the temperature range 600 to 700°C the swelling increased rapidly with increasing temperature. We assumed that all swelling results from the accommodation of helium in equilibrium gas bubbles, as was the case for type 316 stainless steel with high helium content.

Swelling increased as the fluence increased. The two data points at each temperature from 400 to 700°C showed a greater than linear dependence of swelling on the helium content. The average exponent of the swelling dependence on helium content for these four temperatures is 1.53, in good agreement with the value 1.5 expected if the swelling is the result of equilibrium gas bubbles containing all the neutronically produced helium. This also assumes that the cavity concentration is independent of helium content at each temperature.

The magnitude of swelling found in these experiments is much larger than found under conditions producing higher dpa levels but little or no helium in the metal. Bombardment with nickel ions[1,8] at 625 and 655°C and dpa levels to 140 produced from 0 to 0.6% swelling

and ranked the alloy as "very low swelling" compared with stainless steel. In these HFIR irradiations, with the high helium contents more typical of fusion reactor conditions, comparable swelling occurred at less than 10 dpa.

Brager et al.[2] have determined the swelling in Inconel 600 irradiated in EBR-II to 13–30 dpa in the temperature range 420 to 700°C. For these conditions, where helium production would be below 65 at. ppm, swelling less than 0.35% resulted. Furthermore, the swelling decreased with increasing temperature, with an upper temperature limit for cavity formation of about 610°C. Preirradiation cold work of 50% also suppressed swelling relative to solution annealed material for the EBR-II irradiation.

All this evidence supports the thesis that, in the presence of high helium production during irradiation, swelling of Inconel 600 is driven by the gas content. Control of swelling would thus require development and stabilization of a high concentration of cavities, since the swelling produced by equilibrium gas bubbles and a fixed gas concentration will decrease as the concentration of cavities increases.[9] The current results show that 20% cold work does not suppress swelling.

4.1.4.4 Discussion of Tensile Properties and Fracture Mode

The tensile properties, combined with results of examination of fracture surfaces, suggest that the irradiation-produced helium in these samples dominates the mechanical properties for temperatures of 500°C or higher. Strength values of samples irradiated and tested at 500°C or higher fall below the strength values of control samples, and ductilities also are severely reduced. Ductilities at 500°C are near 5%, and the fracture surfaces show mixed intergranular separation and transgranular tearing. At higher temperatures the fractures become fully intergranular. The low stresses in tests at the highest temperatures thus reflect the low decohesion stress to separate grains and do not reflect the flow stress of the matrix material. In the temperature range 500 to 700°C the strength values are a strong function of temperature.

In the temperature range 55 to 300°C the yield and ultimate stresses were insensitive to temperature. Both cold-worked and solution annealed material were strengthened by the irradiation, and ductility values were reduced. This response suggests the classic irradiation hardening that results from displacement damage. In this range the influence of helium probably arises through its influence on the development of the damage microstructure, rather than through any direct influence on the deformation or fracture process.

The transition between these two behavior regimes probably occurs in the range 400 to 500°C but is not well defined by these experiments. Any transition temperature can also be expected to be a function of fluence.

The general strengthening and ductility reduction observed for the lower temperatures in these experiments are similar to results reported[10] after EBR-II irradiation of the same alloy to about 1.5 dpa. In the case of the same alloy irradiated in thermal spectrum reactors, but to lower fluences, a somewhat similar dependence of tensile properties on temperature was found.[11] [The neutron spectrum for the reactor used in the latter experiments is not available. Significant helium production during irradiation seems likely, but the data needed for exact calculations of dpa and helium content are not available.] Claudson[11] evaluated the property dependence on test temperature for fixed irradiation temperature. He reported more severe ductility loss for tests at 650°C than at lower temperatures. He also found the 650°C ductility loss to be relatively insensitive to irradiation temperature. The present experiments showed the same trend; irradiation at 55 and 600°C resulted in similar low values of postirradiation ductility in 600°C tests.

4.1.5 Conclusions

Irradiation of Inconel 600 to produce 4 to 9 dpa and helium contents of 600 to 1800 at. ppm at temperatures in the range 55 to 700°C produces significant swelling and loss of postirradiation tensile ductility. Swelling is only slightly temperature dependent and no more than 1% for temperatures from 55 to 600°C. Swelling increases rapidly

with increasing temperature from 600 to 700°C. Strength values are above those of control samples for temperatures below about 450°C. For higher temperatures, the strength values drop well below the strengths of unirradiated material. Similarly, the elongation was most severely reduced for temperatures of 600 and 700°C.

These results show that the helium produced during irradiation drives the property changes. For temperatures below about 600°C, the swelling is small but is much greater than would be produced in low-helium irradiations. The swelling is presumed to result from the microstructural accommodation of the gas in bubbles. At higher temperatures much greater swelling results, with up to 4% swelling at 700°C. For temperatures above about 500°C failure occurs by intergranular separation, and the low decohesion stress results in low stresses in tensile tests.

The helium domination of the irradiation response of this alloy requires caution in judging the irradiation response of candidate alloys based on limited simulation experiment data. In particular, the results of irradiations in "hard" neutron spectra or in heavy ion bombardments must be used with caution, since they generally lack the appropriate helium content of the sample.

The high helium production rate expected for Inconel 600 in service in a fusion reactor and the serious effects of helium on the irradiation response and postirradiation properties of this alloy do not make it an attractive candidate for fusion reactor structures. The lack of effectiveness of 20% cold work in improving the postirradiation response was particularly surprising and discouraging. Inconel 600 has no advantage over type 316 stainless steel and does not warrant further development for fusion reactor application.

4.1.6 References

1. W. H. Johnston et al., "An Experimental Survey of Swelling in Commercial Fe-Cr-Ni Alloys Bombarded with 5 MeV Ni Ions," *J. Nucl. Mater.* 54: 24–40 (1974).

2. H. R. Brager, J. L. Straalsund, and T. K. Bierlein, "Irradiation Swelling Resistance of Inconel 600," *Quarterly Progress Report Irradiation Effects on Reactor Structural Materials, November, December 1971, January 1972,* HEDL-TME 72-27, pp. HEDL-77 to 87.
3. T. A. Gabriel, B. L. Bishop, and F. W. Wiffen, "Calculated Atom Displacement and Gas Production Rates of Materials Using a Fusion Reactor First Wall Neutron Spectrum," *Nucl. Technol. 38:* 427–33 (1978).
4. T. A. Gabriel, B. L. Bishop. and F. W. Wiffen, *Calculated Irradiation Response of Materials Using* ***Fission*** *Reactor (HFIR, ORR, and EBR-II) Neutron Spectra,* ORNL/TM-6361 (in preparation).
5. F. W. Wiffen, E. J. Allen, H. Farrar, E. E. Bloom, T. A. Gabriel, H. T. Kerr, and F. G. Perey, "The Production Rate of Helium During Irradiation of Nickel in Thermal Spectrum Fission Reactors," paper to be presented at the First Topical Meeting on Fusion Reactor Materials, Jan. 29–31, 1979, Miami Beach, Fla.
6. R. L. Fish and C. W. Hunter, "Tensile Properties of Fast Reactor Irradiated Type 304 Stainless Steel," pp. 119–38 in *Irradiation Effects on the Microstructure and Properties of Metals, ASTM Spec. Tech. Publ.* 611, American Society for Testing and Materials, Philadelphia, 1976.
7. P. J. Maziasz, F. W. Wiffen, and E. E. Bloom, "Swelling and Microstructural Changes in Type 316 Stainless Steel Irradiated Under Simulated CTR Conditions, pp. 259-88 in *Radiation Effects and Tritium Technology for Fusion Reactors,* Vol. I, CONF-750989 (March 1976).
8. A. F. Rowcliffe, S. Diamond, M. L. Bleiberg, J. Spitznagel, and J. Choyke, "Swelling and Irradiation Induced Microstructural Changes in Nickel-Based Alloys," pp. 565–83 in *Properties of Reactor Structural Alloys After Neutron or Particle Irradiation, ASTM Spec. Tech. Publ.* 570, American Society for Testing and Materials, Philadephia, 1975.
9. R. S. Barnes, "A Theory of Swelling and Gas Release for Reactor Materials," *J. Nucl. Mater. 11:* 135–48 (1964).

10. J. M. Steichen and R. L. Knecht, "LMFBR Structural Materials Applications," pp. C-5 to C-13 in *HEDL Quarterly Technical Report*, HEDL-TME-74-4 Vol. 1 (January 1975).

11. T. T. Claudson, "Effects of Neutron Irradiation on the Elevated Temperature Mechanical Properties of Nickel-Base and Refractory Metal Alloys," pp. 67–94 in *Effects of Radiation on Structural Metals, ASTM Spec. Tech. Publ.* 426, American Society for Testing and Materials, Philadelphia, 1967.

5. PATH C ALLOY DEVELOPMENT — REACTIVE AND REFRACTORY ALLOYS

Two distinct and separate subgroups fall under the broad classification of path C alloys. These subgroups are conveniently classified as "reactive metal alloys" and "refractory metal alloys." Analyses of the properties required for performance of materials in high-flux regions of fusion reactors and assessments of the known and extrapolated properties have identified titanium alloys of the reactive metal alloys and vanadium and niobium alloys of the refractory metal alloys as having the most promise for fusion reactor applications. For both the reactive and refractory alloys, there is an extreme lack of data that are relevant and necessary for selection of specific alloy types for development (i.e., solid solution, precipitation strengthened, single or multiphase). In the case of titanium alloys, the most critical deficiency is the lack of data on the response of these alloys *to* high-fluence neutron radiation. For vanadium and niobium alloys, while the effects of radiation on mechanical behavior are not adequately known, perhaps the most alarming deficiency is the near total lack of base-line information on the effects of cyclic (fatigue) loading on mechanical performance. Precisely because of these deficiencies in the data base and overall metallurgical experience, these alloys are still in a "scoping study" phase of their evaluation as candidates for fusion reactor first-wall materials.

The ADIP task group has selected four titanium alloys, three vanadium alloys, and two niobium alloys for the scoping phase of the development program. Titanium alloys are generally classified according to the relative amounts of α (hcp) and β (bcc) phases that they contain. The titanium alloys selected represent the three alloys (types α plus β, α rich, and β rich). Vanadium and niobium alloys are not in commercial use as are the other alloy systems in the program. Selection of the scoping alloys was based primarily on results of previous programs on vanadium cladding development for LMFBRs and high-temperature alloys for space power systems. The three vanadium alloys are V—20% Ti, V—15% Cr—5%Ti, and Vanstar 7. The binary has relatively good fabricability, and appears to be swelling resistant in fast-reactor irradiations but is rather weak. The ternary V—15% Cr—5% Ti and precipitation-strengthened

Vanstar 7 alloys are significantly stronger. The Nb-1% Zr binary alloy is included as a reference material, since a significant amount of data exists for this alloy irradiated in fast reactors. The alloy Nb-5% Mo-1% ZR is much stronger than the binary and can be developed for applications near 800°C.

Near-term activities on path C alloys will focus on obtaining data on the unirradiated mechanical properties, corrosion and compatibility, and the effects of irradiation on physical and mechanical properties. Fission reactor irradiation with and without helium preinjection, high-energy neutron sources, and charged-particle irradiations will be used in the development of techniques to approximate the effects of the fusion reactor neutron spectrum (He/dpa production). The objective is to develop sufficient understanding of the behavior of path C alloy systems (Ti, V, and Nb alloys) to allow selection of path C base research alloys. The effects of composition and microstructure on alloy performance will then be investigated in the base research alloys.

5.1 MICROSTRUCTURE OF TITANIUM SCOPING ALLOYS PRIOR TO IRRADIATION – J. W. Davis, S. M. L. Sastry, and L. J. Pionke (McDonnell Douglas).

5.1.1 ADIP Task

Task Number I.C.4 – Microstructures and Swelling in Reactive/Refractory Alloys (Path C).

5.1.2 Objective

To characterize the microstructure of titanium alloys prior to irradiation and to provide a comparative base for postirradiation analysis.

5.1.3 Summary

Initial studies have been begun to characterize the microstructures of the titanium scoping alloys prior to irradiation. Also included are the titanium alloys that were under study prior to the selection of the scoping alloys. In general, the alpha base alloys (Ti-6242s and Ti-5621s) are composed of a high amount of primary alpha and transformed beta. The transformed beta is essentially composed of alpha platelets and interplatelet beta. The beta alloys, Ti-38-6-44 and Ti-15-3 as the name implies are composed primarily of beta phase with alpha phase precipitates. The alpha phase exists both intergrannuarly and transgrannuarly. The morphology of alpha phase depends critically on aging temperature and time. For example, a fine distribution of small alpha is produced upon aging at 500°C, higher temperatures results in a coarse distribution of relatively large (> *100* nm) alpha platelets in the beta grain.

The alpha-beta alloy, Ti-6Al-4V has a variety of microstructures available, depending upon heat treatment, but the primary phase is alpha. The low temperature mill anneal, below the beta transus, results in a very fine grained structure consisting of primary equiaxed alpha and grain boundary beta. The beta anneal results in a fully transformed beta microstructure consisting of Widmanstätten alpha-beta plates in air cooled alloys and hexagonal martensite (alpha prime) in fast cooled alloys.

5.1.4 Program and Status

Titanium alloys have been proposed for use as first wall and blanket structure of fusion reactors. However, little is known about the relative resistance of titanium alloys to radiation damage, especially at the temperatures and fluence levels of interest. In order to develop more information on the effect of radiation on the microstructure and mechanical properties of titanium the ADIP task group included titanium in its Path C refractory/reactive metal scoping studies.[1] The alloys selected for these studies are shown in Table 5.1.1 and are based on the recommendations of various titanium suppliers and research groups.[2] Also shown in the table are titanium alloys that were included in experiments prior to the ADIP alloy recommendations.[3-6] To date, all of the titanium included in these studies has been obtained from the titanium inventory. This inventory was established to fulfill the requirements of the various experimenters and contains all of the scoping alloys. All material is documented with respect to chemistry, heat treatment, and tensile properties. In addition, since many of the experimenters are unfamiliar with titanium's microstructure, MDAC initiated a study to characterize the various microstructures of the materials currently contained in the inventory. This report briefly describes the results of the microstructural analysis to date.

Over the past 20 years considerable effort has been devoted to developing titanium alloys. These studies revealed that specific phases or microstructures present in titanium can affect properties such as creep, fatigue and tensile strength. It is for this reason that the microstructural changes brought about by alloying are the basis for the classification of titanium alloys into alpha (HCP), beta (BCC), and alpha-beta groups. In general, the single phase and near single phase alpha alloys (these alloys have a small amount of beta) exhibit good weldability and are not heat treatable. Among the principal alpha stabilizing elements in titanium are aluminum, tin and zirconium. In alloys that contain large amounts of beta stabilizing elements such as vanadium, molybdenum, niobium and tantalum the beta phase is retained as a metastable phase, on air cooling from above the beta transus to room temperature. The beta alloys are heat treatable, are capable of high strengths and usually are not

weldable. The alpha-beta alloys which contain both alpha stabilizing and beta stabilizing elements can contain from 10 to 50% beta phase at room temperature. The alloying elements in this class of alloy tend to partition to either phase according to their alpha-stabilizing or beta-stabilizing characteristics. These alloys are heat treatable and are usually weldable provided the amount of beta phase is kept below 20%. The scoping alloys shown in Table 5.1.1 are representative of these 3 classes of materials.

TABLE 5.1.1 TITANIUM ALLOYS INCLUDED IN MICROSTRUCTURE STUDY

ALLOY DESIGNATION	ALLOY CLASSIFICATION	COMPOSITION	CONDITION	STUDY REFERENCE*
Ti-6-4	α + β	Ti-6Al-4V	MILL ANNEAL	2*4,5
			DUPLEX ANNEAL	2*,4
			BETA ANNEAL	2*4,5
			RECRYSTALLIZATION ANNEAL	4
Ti-6242S	α	Ti-6Al-2Sn-4Zr-2Mo-0.09Si	DUPLEX ANNEAL	2*3,5
Ti-5621S	α	Ti-5Al-6Sn-2Zr-1Mo-0.25Si	DUPLEX ANNEAL	2*3,5
Ti-811	α	Ti-8Al-1Mo-1V	MILL ANNEAL	4
Ti-38-6-44	β	Ti-3Al-8V-6Cr-4Mo-4Zr	SOLUTION TREAT + AGE	2*
Ti-15-3	β	Ti-15V-3Cr-3Al-3Sn	SOLUTION TREAT + AGE	5
			SOLUTION TREAT + OVERAGE	3,4

* SCOPING STUOV ALLOYS

**SEE REFERENCES

The alpha alloys selected for the scoping studies are Ti-6242s and Ti-5621s (see Table 5.1.1 for alloy compositions) both were supplied in what is referred to as the duplex anneal condition. The annealing cycle for the Ti-6242S consisted of 30 minutes at 900°C followed by a rapid cool to room temperature and a reanneal for 15 minutes at 790°C. This annealing cycle produced the microstructure shown in Figure 5.1.1(a). The initial annealing temperature of 900°C is well below the beta transus (990°C) and as a result of the structure consists of large amounts of equiaxed primary alpha and small regions of transrormed beta. The transformed beta structure is too fine to be resolved optically. The transformed beta structure can be more easily distinguished in the transmission electron micrograph shown in 5.1.2(a).

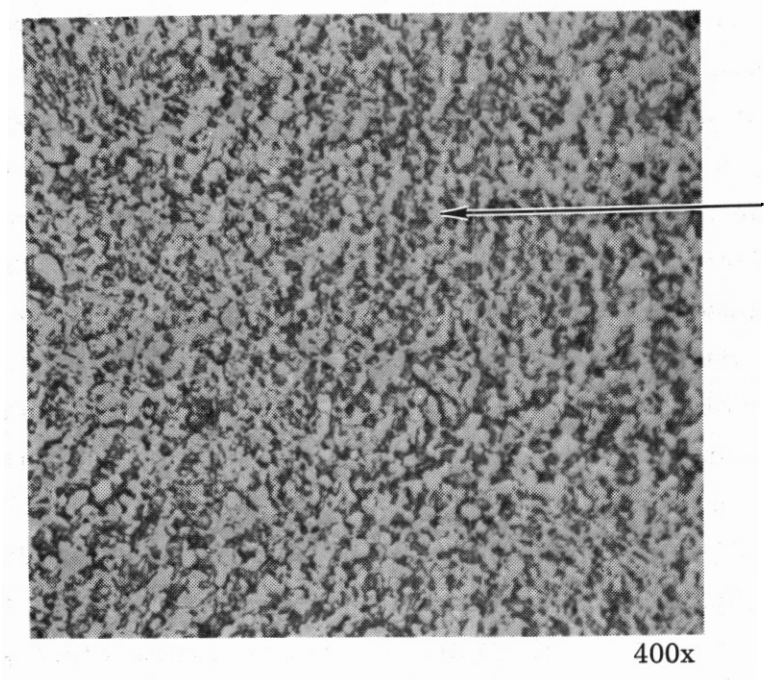

(a) Ti—6242s in Duplex Annealed Condition

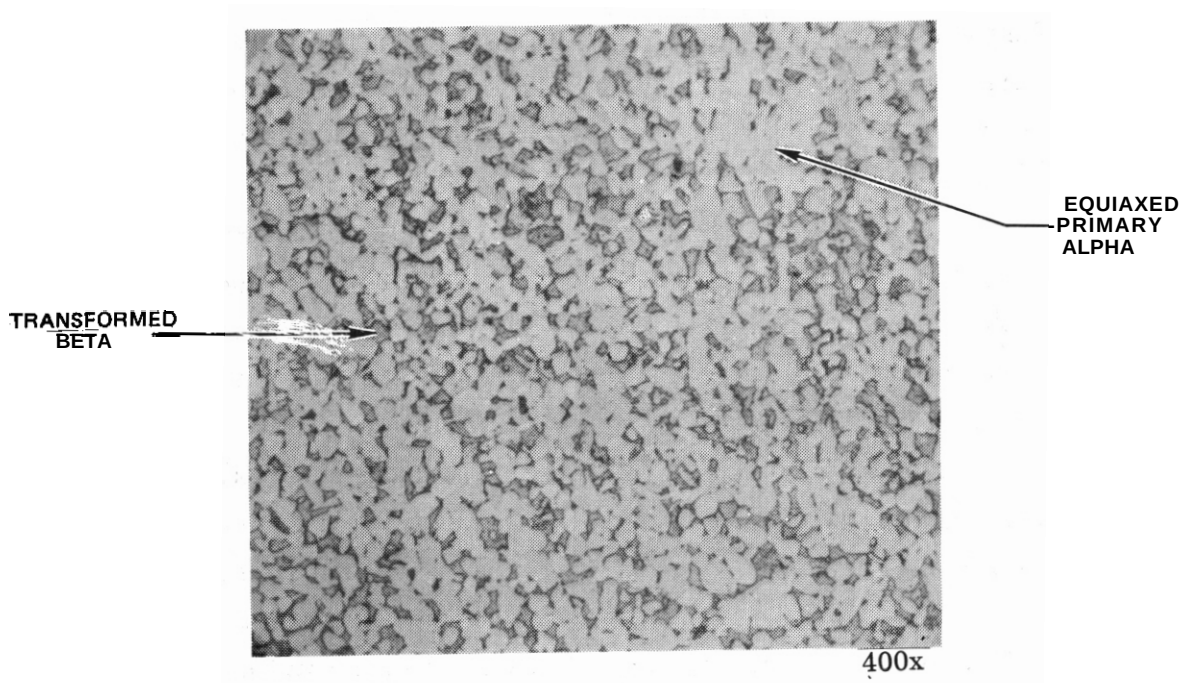

(b) Ti—5621s in Duplex Annealed Condition

Figure 5.1.1 Microstructures of Alpha Scoping Alloys Prior to Irradiation

Since the second annealing was also done at high temperatures close to the single phase alpha field, the retained beta from the first anneal has transformed to fine equiaxed alpha on subsequent annealing and as a result only a very small amount of intergranular beta is retained. In contrast to the predominantly single phase microstructure of Ti-6242s. the Ti-5621s alloy conta: e volume percent, formed beta, as seen in Figures 5.1.1(b) and 5.1.2(b). These differences are primarily due to the differenc nealing schedu. two alloys. The annealing cycle for Ti 5621S alloy used in the HBBL experiment,(5) and the MFE #1(6) consisted of 15 minutes at 955°C followed by air cooling to room temperature and reannealing at 575°C for 2 hours and air cooling to room temperature. The microstructure of this alloy is shown in Figure 5.1.1(b). The initial annealing temperature for Ti-5621s is nearer the beta transus (1010°C) than for Ti-6242, which results in larger alpha grains and, a greater volume percent of transformed beta. The transformed beta shown in Figure 5.1.2(b) consists of Widmanstätten alpha-beta plates formed as a result of nucleation and growth of alpha in a beta matrix. Both of these alloys contain small amounts of silicon, which is added to improve high temperatur . The precise role of silicon in these alloys is not known at this time and silicon compounds were not observed in the microstructures.

The beta alloy selected for scoping studies is Ti-38-6-44 which is a commercial alloy. Prior to the selection of Ti-38-6-44 another beta alloy Ti-15-3 was included in some early experiments.(3-5) This alloy is in the early development stages and is reported to be more stable than previous beta alloys. Since this alloy is also being evaluated in some experiments it was decided to include it in the microstructure studies. The beta alloys are heat treatable and can achieve very high strength levels, through the precipitation of hexagonal alpha phase in a bcc beta matrix, they are usually used in solution treat and aged condition (STA). For the Ti-38-6-44 alloy this heat treatment consisted of solution treating at 815°C for 30 minutes, rapid cooling to room temperature and aging for 8 hours at 620°C. The solution treatment is above the beta transus (795°C) and as a result the structure is all beta. During aging the structure

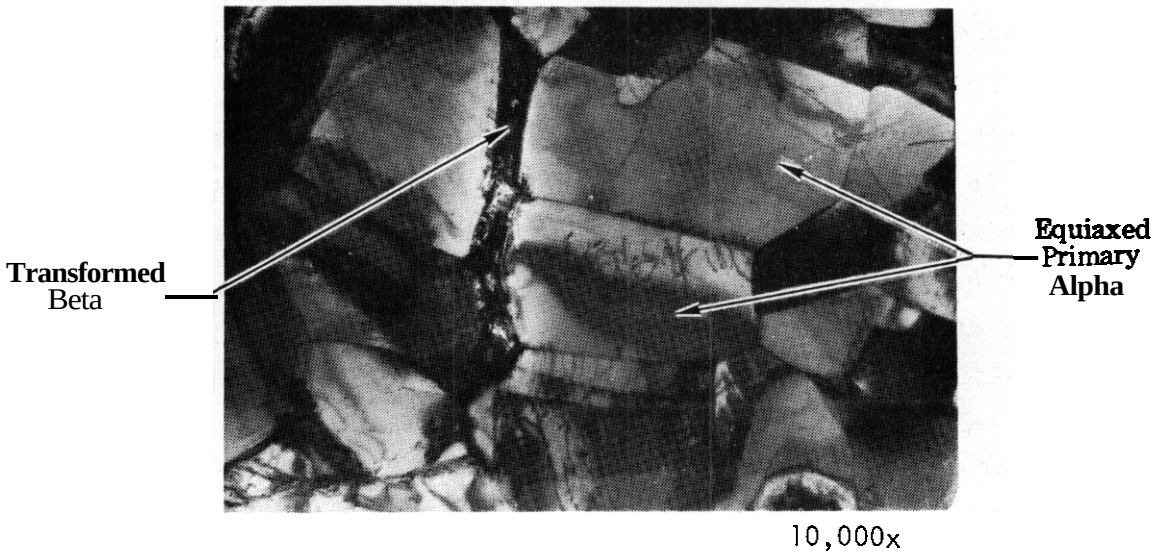

(a) Ti-6242S in Duplex Annealed Condition

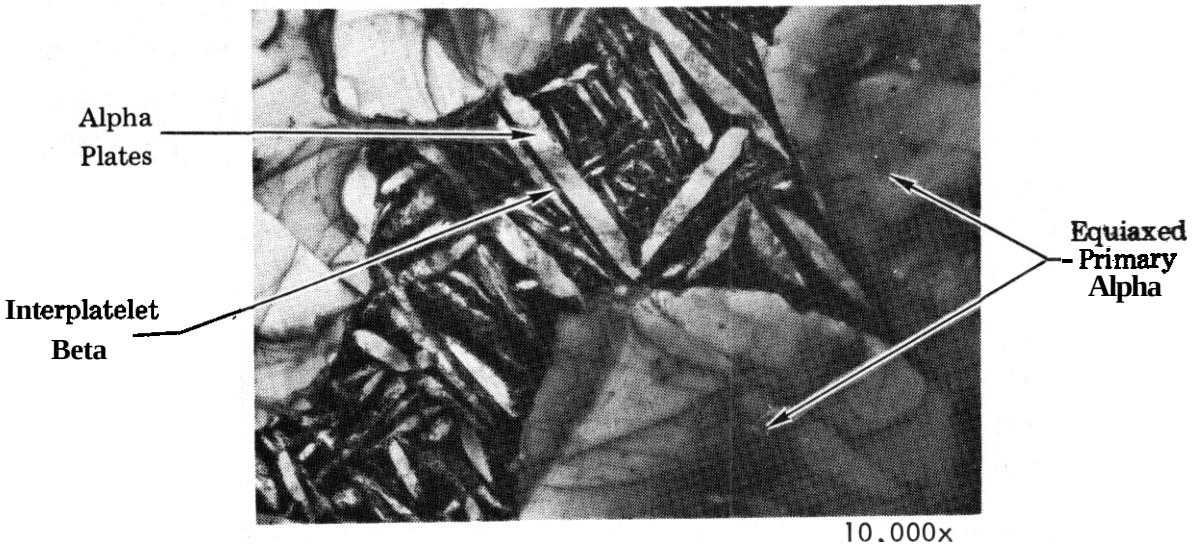

(b) Ti-5621S in Duplex Annealed Condition

Figure 5.1.2 Transmission Electron Micrographs of Alpha Titanium Scoping Alloys Prior to Irradiation

begins to transform and the alpha precipitates both intergranularly and transgranularly (See Figure 5.1.3(a)). At this aging temperature and time the volume of alpha in the structure is roughly 22%.

By varying the aging treatments,two types of alpha precipitates can be produced in this alloy. A lower aging temperature (below 500°C) and shorter aging durations (< 4 hours) results in the formation of a type 1 alpha which obeys the Burger's orientation relation and a large noncoherent type 2 alpha precipitate , formed by aging 500°C, which do not obey the Burger's relation. Even though high strengths can be obtained by small coherent alpha precipitates, the resulting ductility is very low. The best combination of strength and ductility is obtained with the large noncoherent type 2 alpha. Since the alloy was aged at 620°C, the resulting alpha precipitates are the large noncoherent type 2 alpha precipitates as seen in the transmission electron micrograph (Figure 5.1.4(a)).

The Ti-15-3 is in 2 heat treat conditions. The first is the standard solution treat and age which consists of solution treating at 760°C for 15 minutes and aging for 16 hours at 510°C. This material is currently being evaluated in the HEDL irradiation creep experiment.[5] The 760°C solution treating temperature is slightly below the beta transus temperature (790°C) but results in essentially the same microstructure as the Ti-38-6-44 (See Figure 5.1.3(b)). The precipitates formed on aging the alloy at 510°C is shown in 5.1.4(b). The Ti-15-3 alloy used in the ANL dual ion irradiation experiment[4] is in the overaged condition. This heat treatment consisted of solution treating at 760°C for 15 minutes and air cooling which is the same as the previous heat treatment of Ti-15-3, however the aging cycle consisted of 4 hours at 650°C followed by a slow furnace cool. Upon aging the alloy at a higher temperature (650°C), a larger amount of coarser alpha is precipitated as shown in Figures 5.1.5(a) and 5.1.5(b). The alloy aged at 510°C contains a fine, differently oriented, elongated alpha precipitate from 0.1 to 1 μm in size, while the alloy annealed at 620°C has a much coarser alpha.

The two phase alpha-beta alloy selected for the scoping studies is Ti-6Al-4V. Since Ti-6Al-4V is a heat treatable alloy there are a variety

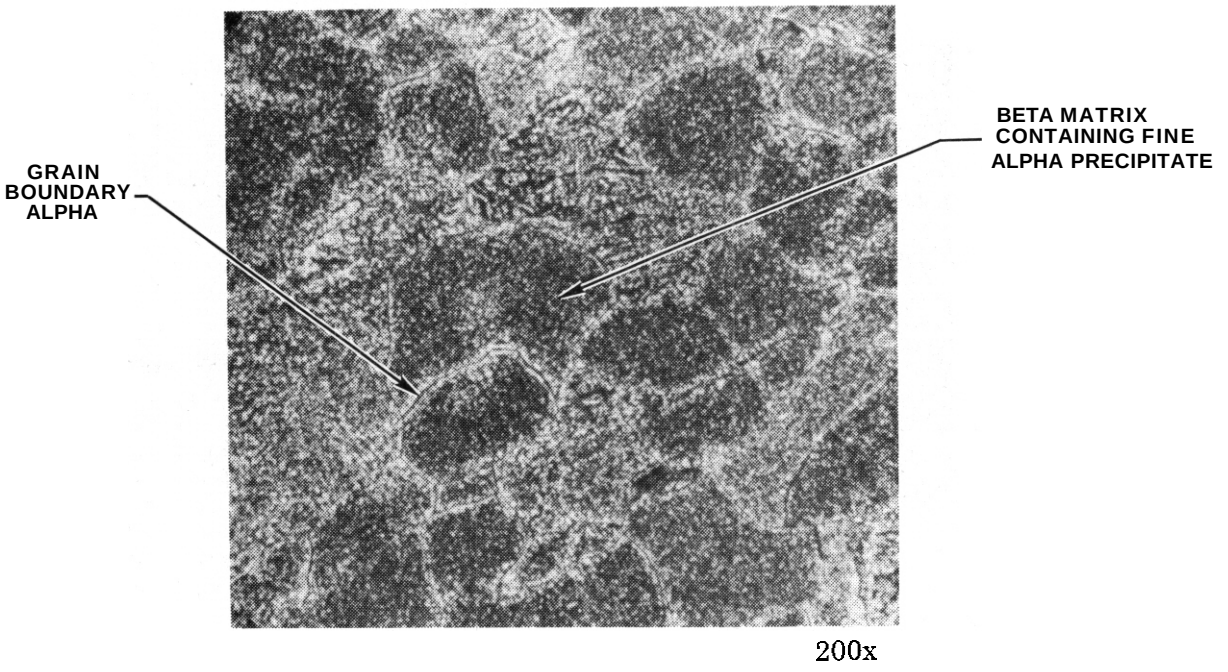

(a) Ti—38—6—44 in **the Solution Treat and Age Condition**

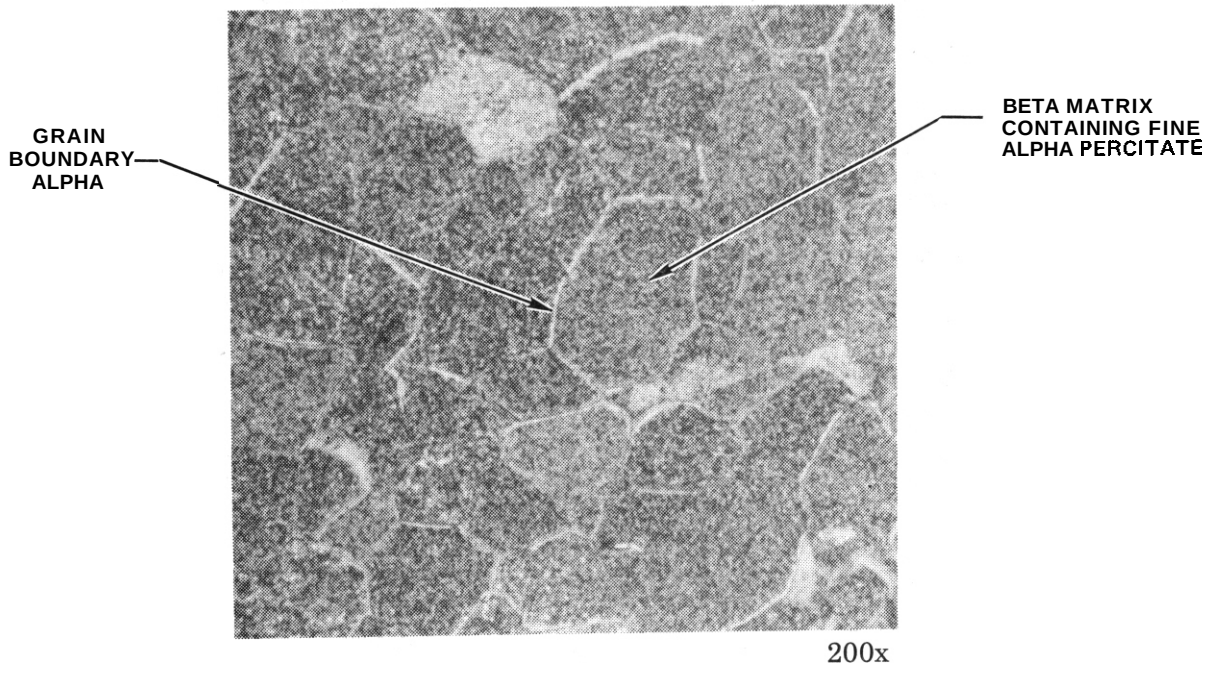

(b) Ti—15—3 Solution Treated at 760°C and Aged for **16** Hours **at 510°C**

Figure 5.1.3 Microstructures of **Beta Alloys Prior to Irradiation**

)x

(a) Ti—38—6—44 in Solution Treated and Aged Condition

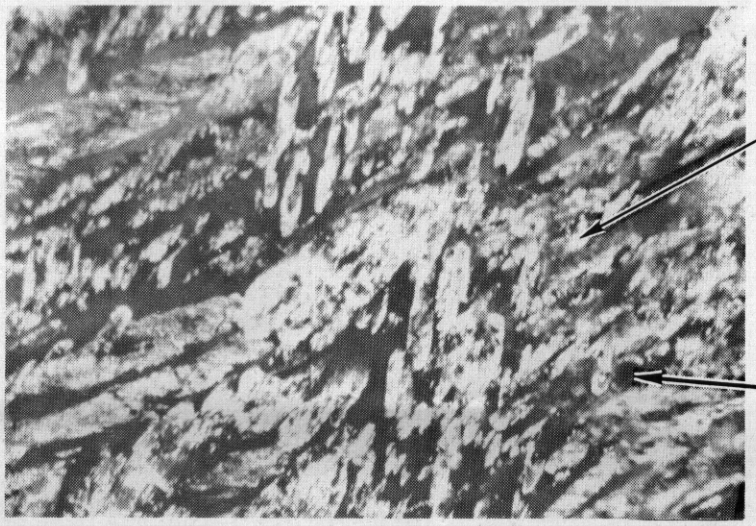

Dark Field 41,000x

(b) Ti—15—3 Solution Treated at 760° and Aged for 16 Hours at 510°C.

Figure 5.1.4 Transmission Photomicrographs of Beta Alloys Prior to Irradiation

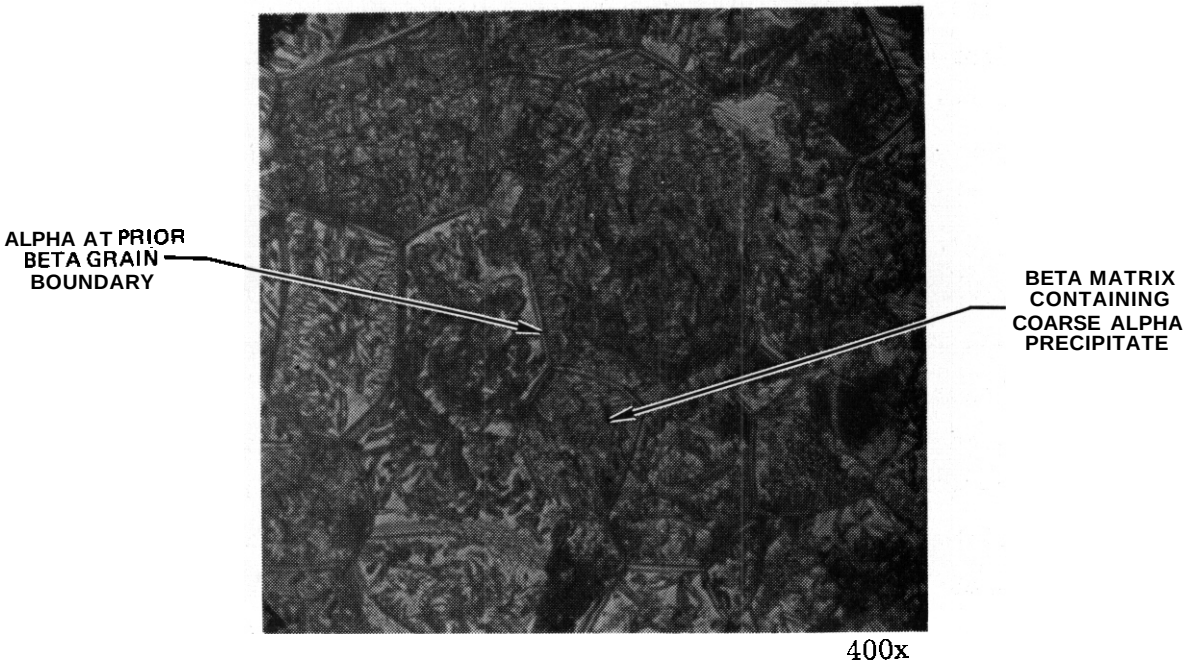

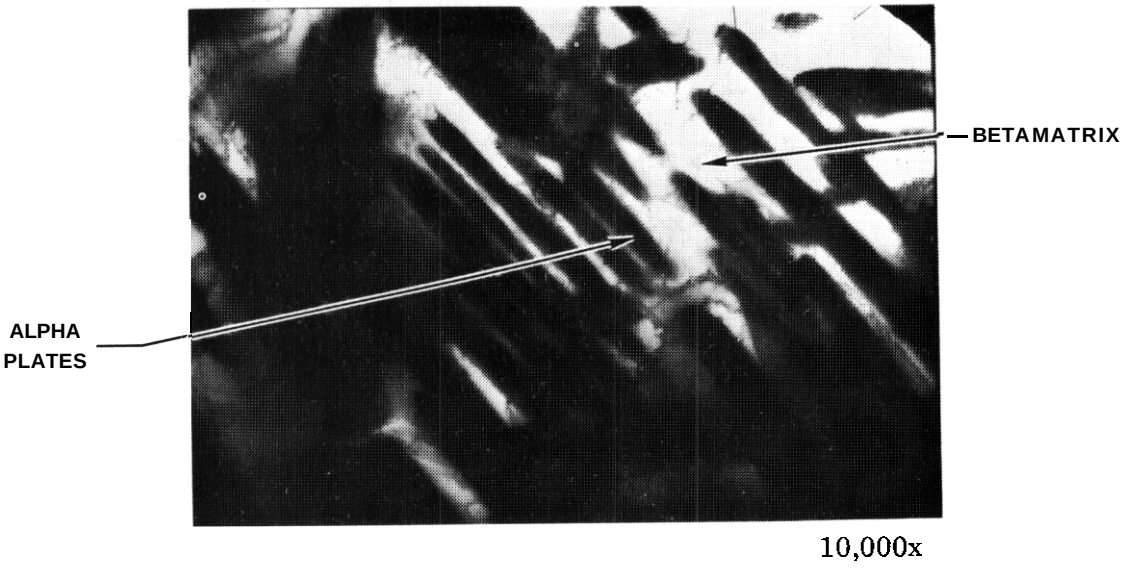

Figure 5.1.5 Microstructure of Ti–15–3 Solution Treated at 760°C and Aged For 4 Hours at 650°C

of heat treatments available, each of which produces a different microstructure, improving certain properties. Three heat treatments were selected for the scoping studies. They are mill-, beta-, and duplex-anneal. The mill anneal consisted of 2 hours at 730°C followed by a rapid argon cool. This annealing temperature is well below the beta transus of 995°C and results in a microstructure consisting of very fine equiaxed primary alpha and intergranular beta (See Figure 5.1.6). Annealing above the beta transus as in the case of the beta anneal (30 minutes at 1040°C) followed by fast cooling, results in the transformation of beta to hexagonal martensite alpha prime (if the cooling rate is very fast) or to Widmanstätten alpha beta platelets at moderate cooling rates. Alpha prime is a nonequilibrium, supersaturated, alpha structure produced by diffusionless transformation of the beta phase. Upon reannealing the martensite structure at 700°C, the alpha prime transforms to equilibrium alpha plus beta, the beta being formed by nucleation and growth processes. The alpha nucleates heterogeneously at the martensite plate boundaries and at the internal martensite structure. A high magnification micrograph of alpha-beta structure resulting from the tempering of alpha prime martensite is shown in Figure 5.1.7(a). Air-cooling from above the beta transus results in a fine acicular Widmanstatten alpha shown in Figure 5.1.7(b). There is also a preferential nucleation of alpha at the prior beta grain boundaries.

The duplex anneal consists of 10 minutes at 940°C, followed by air cooling and a stabilization of 4 hours at 675°C. The microstructure produced by this heat treatment, shown in Figure 5.1.8 consists of primary equiaxed alpha and transformed beta. The relative sizes and amounts of alpha and beta depend on the alpha-beta annealing temperature. Depending on the cooling rate from the alpha-beta annealing temperature, the high temperature beta phase transforms to either metastable retained beta (in the case of water quenching) or transformed beta (in the case of air cooling). The subsequent annealing at lower temperature stabilizes the microstructure by the transformation of beta to equilibrium products.

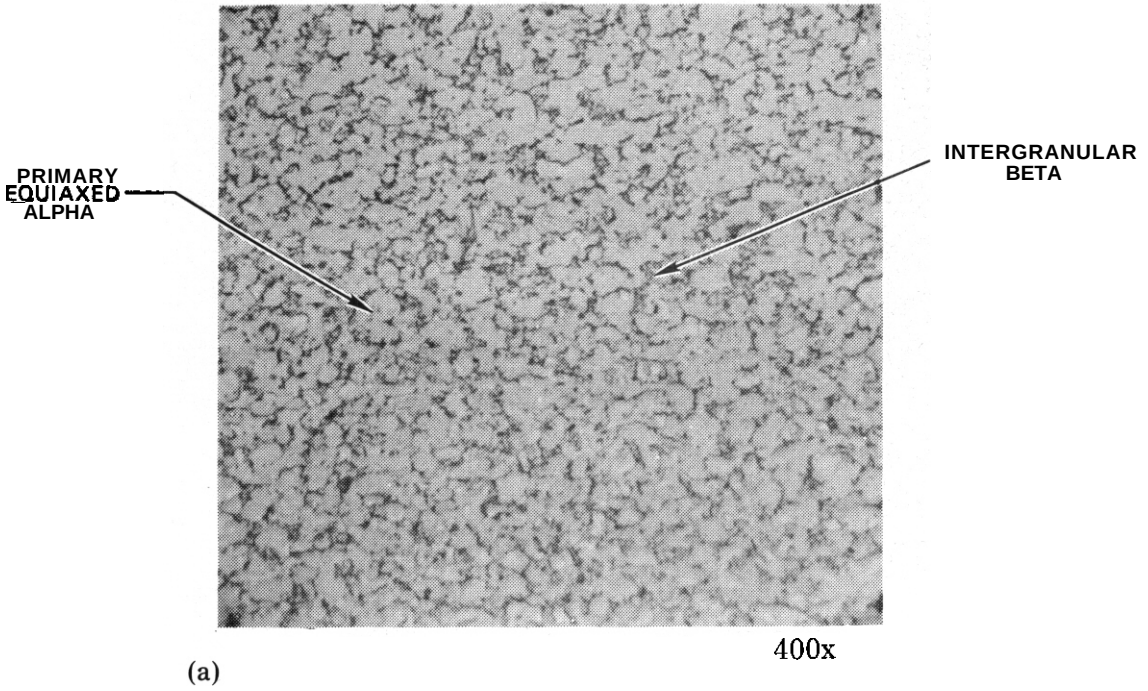

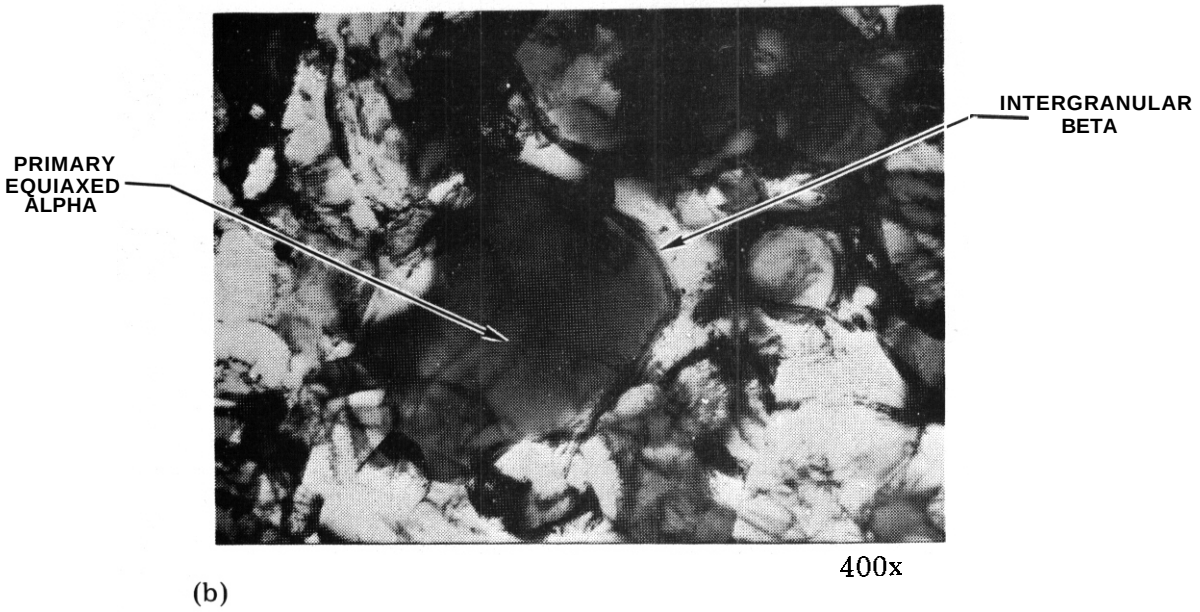

Figure 5.1.6 Microstructure of Ti–6A1–4V in the Mill Anneal Condition

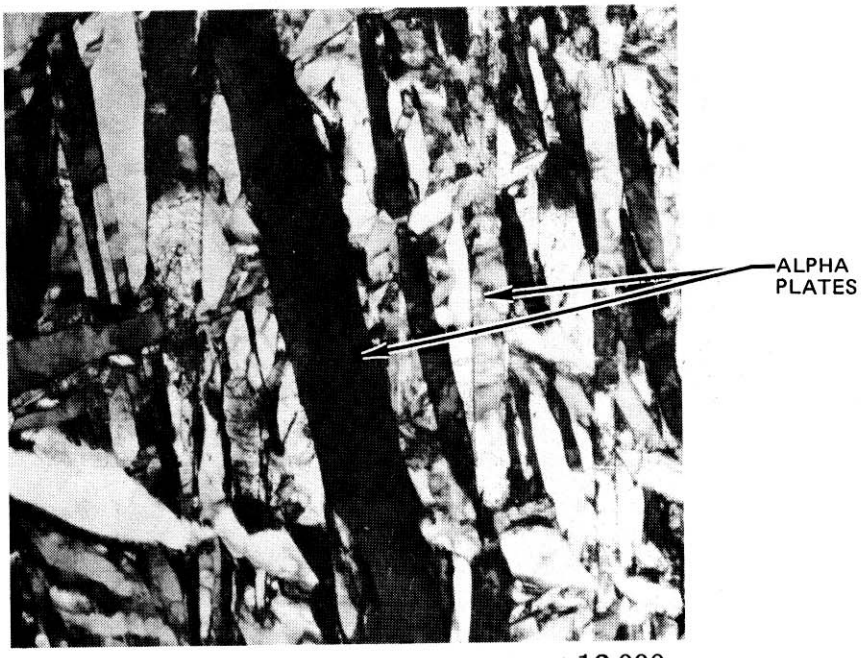

12,000x

(a) Martensite Structure in Ti—6Al—4V, Quenched from 1040°C and Reannealed at 700°C for 2 hours.

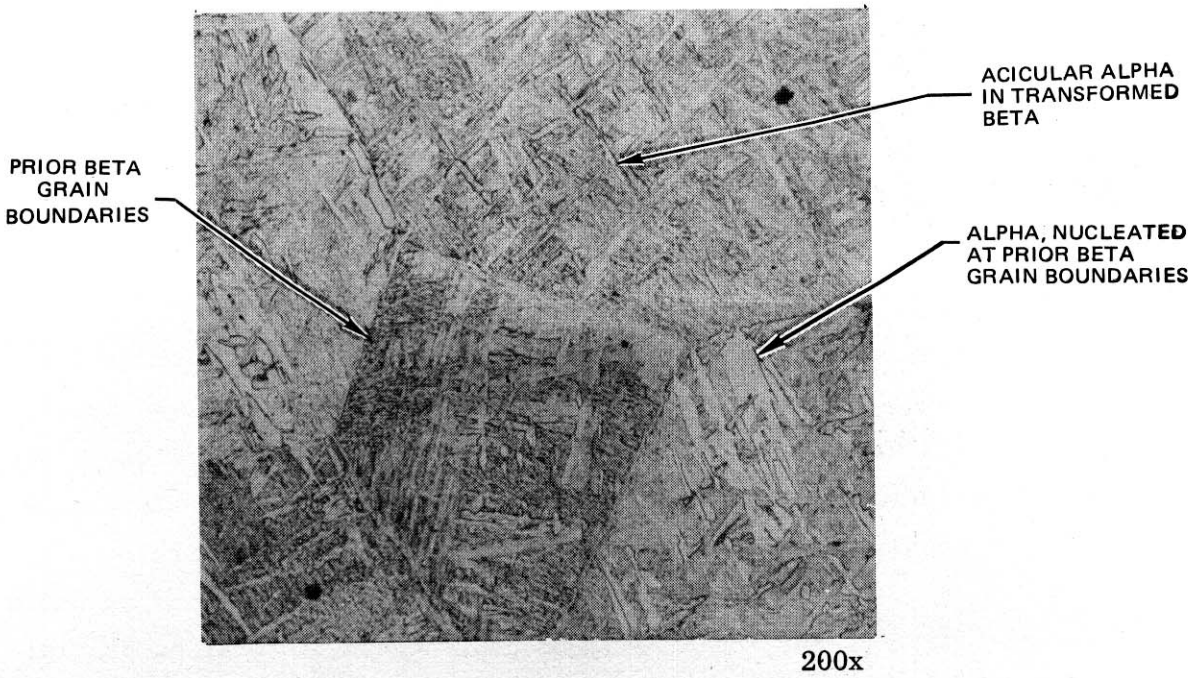

200x

(b) Acicular Alpha in Ti—6Al—4V, cooled in Argon From 1040°C and Reannealed at 700°C for 2 hours.

Figure 5.1.7 Microstructures of Ti—6Al—4V in the Beta Anneal Condition

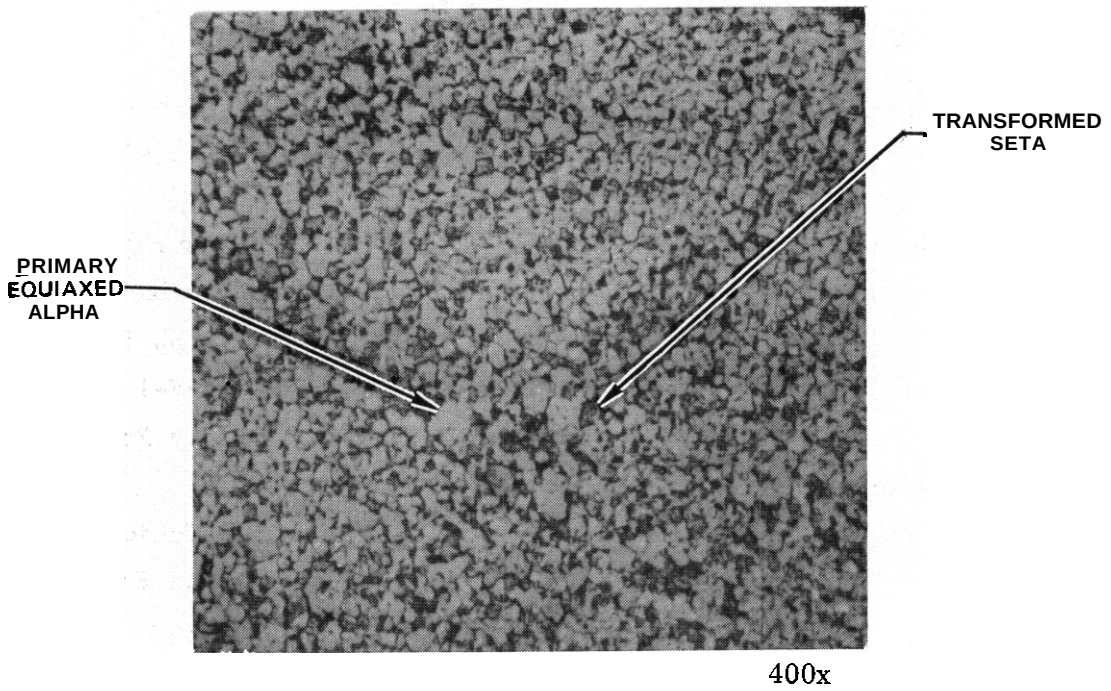

Figure 5.1.8 Microstucture of Duplex Annealed Ti—6Al—4V

5.1.5 Future Work

During the next quarter the transmission electron microscopic studies on the beta and duplex anneal of Ti-6Al-4V will be completed. In addition studies of the Ti-8Al-1Mo-1V will be initiated. The primary thrust of the studies, however, will be to identify the phase composition and the degree of crystallographic texture present in the alloys. Since the formation of Ti_3Al has been shown to embrittle some commercial titanium alloys, rich in aluminum, attention will be focused on the determination of the presence of Ti_3Al in Ti-8-1-1 and Ti-6242s. The nature of five alpha precipitates produced on aging the beta alloys at lower temperature will be studied by TEM which will enable the comparison of the alpha precipitates in the condition with that of radiation modified precipitate. The Ti-6242s and Ti-5621s alloys will be studied with particular emphasis on determining the preference of silicon bearing and tin bearing precipitates, if any.

5.1.6 References

1. E. E. Bloom, et al., Alloy Development for Irradiation Performance: Program Strategy, presented at Third Topical Meeting on The Technology of Controlled Nuclear Fusion, May 9–11, 1978.
2. J. W. Davis, Selection of Titanium Alloys for the Path C Scoping Studies, Reported in Alloy Development for Irradiation Performance Quarterly Progress Report for Period Ending March 31, 1978, pp 109–118.
3. R. W. Powell and G. R. Odette, DAFS Experiment in the ORR–MFE–1 Test, reported in Damage Analysis and Fundamental Studies Quarterly Progress Report for Period Ending March 31, 1978, pp 121–125.
4. S. C. Agarwal and G. Ayrault, Microstructure of Irradiated Fusion Reactor First–Wall Materials, reported in Damage Analysis and Fundamental Studies Quarterly Progress Report for Period Ending March 31, 1978, pp 136–158.
5. R. E. Nygren, Irradiation Induced Stress Relaxation in Titanium Alloys, reported in Alloy Development for Irradiation Performance, Quarterly Progress Report for Period Ending June 30, 1978.
6. J. W. Woods, et al., Status of ORR–MFE–1 and –2 Irradiation Experiments, reported in Alloy Development for Irradiation Performance, Quarterly Progress Report for Period Ending June 30, 1978, pp 164–175.

5.2 EVALUATION OF NIOBIUM ALLOY DATA BASE - L. J. Pionke and J. W. Davis (McDonnell Douglas)

5.2.1 ADIP Task

Task Number I.A.1 - Define Material Property Requirements (Path C)

Task Number I.A.2 - Define Test Matrices and Test Procedures (Path C)

Task Number I.A.3 - Perform Chemical and Metallurgical Compatibility Analyses (Path C)

5.2.2 Objective

Determine the engineering feasibility of using refractory metals in fusion power plant components by identifying those physical and mechanical properties that are critical to the successful performance of refractory metal structure.

5.2.3 Summary

A large data base has been compiled on niobium alloys, however, the data base for any one alloy is limited. There is a large amount known about the metallurgy of niobium alloys and as a result, an alloy composition could be developed to meet the various property requirements, except for radiation damage which is unknown. The tensile and creep properties of niobium-1% Zr are probably below those required and as a result a higher strength ternary will be required. While there is large amount of data on creep and creep-rupture most of the data is at higher temperatures and for shorter times than required in fusion devices. In addition many of the long time creep tests were performed in marginal vacuums and as a result some of the data is suspect.

Data concerning the fatigue behavior at both room and elevated temperature is meager, primarily because past applications were limited by creep and/or oxidation. While the niobium alloys appear to be compatible with the liquid lithium, the impact of interstitial transport may be as critical as the fatigue and flaw growth and as a result data will have to be developed.

5.2.4 Progress and Status

The elevated temperature strength, low thermal stresses, compatibility with most liquid metal coolants and apparent resistance to radiation damage, makes the refractory metals attractive for use as structure in fusion reactors. The elevated temperature strength allows the reactor designer to take advantage of increased thermal conversion efficiency or higher wall loadings while the low thermal stresses and resistance to radiation damage can lead to longer component lifetimes or higher wall loading. Off-setting these advantages are the higher costs associated with using using the refractory metals and a limited data base.

The impact of the higher costs of the refractory metals on the cost of electricity was examined in a recent economic study.[1] This study looked at the relationship between the cost of fabricated hardware, coolant temperature, life and the cost of electricity. By using a reactor with a 5000 MW_{th} capacity, having a noncircular plasma (aspect ratio of 2), lithium as a coolant, and steam for electrical power generation, the costs of electricity associated with using the refractory metals niobium, vanadium and molybdenum in the first wall and blanket, including the header and in the primary coolant loop were determined. The results were then compared to the costs associated with using stainless steel in the same areas. This study indicates that the use of the refractory metal in the first wall, blanket, and header region of a fusion reactor offers an economic advantage over a stainless structure, provided the refractory metals show a modestly longer life or permit a moderately higher peak coolant temperature. If the use is extended beyond the header, for example throughout the primary coolant loop, the cost of electricity will be significantly increased. The increased cost is only recovered for the refractory metals niobium and vanadium over a very narrow set of operating conditions. These conditions require that the stainless steel structure operate with a peak coolant temperature of *400°C* and have a structural life of < 5 MW•yrs/m^2 and the niobium or vanadium operate with a peak coolant temperature of 650°C and have a structural life > 15 MW•yrs/m^2. Based on the results of this study, it appears that the use of the refractory metals, particularly niobium and vanadium, should be limited to the

first wall, blanket, and header region. Beyond this region, lower cost materials such as titanium or stainless steel should be used.

Since the economic advantage of the refractory metals are predicated on their having longer structural lives and/or operating at higher temperatures, analytical studies, similar to those performed on stainless steel, need to be made. However, before these studies can be performed, more information needs to be obtained reguarding the refractory metal data base and identify those properties that are critical or potentially critical to the successful performance of the refractory metals.

Since the economic advantage for the refractory metals rested with their use in the first wall, blanket and header region the scope of the survey was reduced to the type of properties necessary for the design of these structures. In addition, since vanadium was the subject of a previous study and these are questions if molybdenum could ever be used in a structure, the scope of the study was further reduced to include only niobium alloys.[2] A final report covering the results of this study is in preparation and as a result only a synopsis will be presented here.

5.2.4.1 Unirradiated Mechanical Properties

The short time tensile properties, including the effects of interstitials have been well characterized for many of the niobium alloys at both room and elevated temperature. Studies have shown that interstitial impurities can significantly affect the tensile properties, particularly the strain rate sensitivity and the ductile-to-brittle transition temperature. The bulk of this data is for temperatures > 900°C and little of the data exists for the temperature range of interest < 650°C.

The available data concerning the creep-rupture properties of niobium base alloys was developed for aerospace applications which required alloys to sustain a short time (i.e., 100 to 1000 hours) in a high stress environment. Very little creep-rupture data has been developed for the relatively low temperatures (< 650°C) and long times (> 15,000 hours) combinations proposed for the fusion reactor first wall and blanket. In general, it appears that the stress and temperature dependence of creep deformation for niobium are similar to vanadium based on the same homologous temperature (T/Tm).

Data concerning the fatigue behavior at both room and elevated temperature is meager, primarily because past aerospace and nuclear applications were limited by creep and/or oxidation resistance. The elevated temperature fatigue tests that have been reported are for coated specimens or inert atmosphere rather than high vacuum. Elevated temperature tests (> 815°C) of a coated niobium alloy (C103) show lives greater than 10^6 cycles at stresses roughly equivalent to the ultimate tensile strength.

5.2.4.2 Corrosion and Compatibility

In the conceptual fusion reactor designs that are based on the deuterium-tritium reaction, the use of lithium or a lithium compound is proposed for use as a tritium breeder. In some designs, lithium has also been proposed as the primary coolant, although other liquid metals as well as such coolants as helium or molten salts have been also proposed.

Corrosion studies of most refractory metal/alkali metal systems have shown that under certain conditions these metals are highly resistant to mutual dissolution. However, a number of parameters can alter this stability including alloy composition, alloy and liquid metal purity, temperature, liquid metal velocity, and temperature gradients. Interstitial impurities are particularly damaging to the corrosion resistance of such systems, and the damage mode is strongly dependent on whether the impurities are present in the alkali metal or in the refractory metal.

A sufficient amount of data concerning the interaction of niobium and its alloys with the various alkali metals proposed for use in fusion reactors (i.e., lithium, sodium, and potassium) has been generated to indicate specific behavioral trends. The corrosion resistance of niobium in lithium, sodium, and potassium is extremely sensitive to the oxygen concentration of the liquid metal. Oxygen reacts with the niobium to form compounds which, if soluble in these alkali metals or removed by the flowing metal in dynamic systems, can lead to an accelerated rate of attack.

The results of a number of studies conducted using static, refluxing, and flowing test techniques have indicated that, in general, niobium and niobium-base alloys possess excellent compatibility with liquid lithium, potassium, and sodium at temperatures to 1000°C and above, provided

precautions are taken to maintain the interstitial content, particularly for oxygen, to low levels in both the liquid and solid metal.

5.2.4.3 Niobium Alloy Data Needs

Because the main thrust of the past niobium alloy investigations was geared to oxidation and creep resistant applications above 1000°C, it is not surprising that little reliable data or no data at all exists in areas of critical importance to first wall/blanket design. One such area is that concerning the elevated temperature tensile properties of niobium alloys. Although the amount of such data is voluminous, its reliability in the temperature range of a fusion reactor structure (400°C to 800°C) is marginal, due to differences in the quality of the test environment (air, inert gas, vacuum), in strain-rate and in interstitial content. Furthermore, most of the data tabulated over this range of temperatures was obtained by interpolation of plotted curves, and seldom did more than one data point lie in the temperature range of interest.

In contrast, data is completely lacking for such interrelated mechanical properties as moderate temperature creep, creep-fatigue, and fracture behavior. Although the basic steady-state creep resistance of several niobium alloys has been well documented at temperatures above those proposed for first wall/blanket operation, little is known about the long term (10,000 hours or more) creep behavior of such alloys in the temperature range *400°C* to *800°C*. Of even more importance, however, is the knowledge of niobium alloy response under cyclic creep involving fluctuating stress and temperature.

In many of the nonrefractory metals examined for creep fatigue resistance, accelerated creep rates and diminished creep lifetimes have been observed as a result of stress fluctuations, relative to constant load tests at the same peak stress. However, the opposite trend (i.e., creep deceleration) has also been observed underscoring the point that no method currently exists for accurately predicting the response of a given alloy to cyclic creep conditions based on static creep behavior.

The life of the first wall is likely to be determined not only by the creep resistance of the material but also by its resistance to the growth of preexisting, undetected flaws. Such flaw growth can result in a wall penetration, or leak, condition which for most designs is cause for reactor shutdown. However, such a failure mode is infinitely more desirable than a catastrophic brittle failure. Therefore, in order to predict potential failure modes and assess wall life, the fracture toughness and fatigue flaw growth properties must be established.

5.2.5 Conclusions

Like the vanadium base alloys, the viability of niobium base alloys for fusion reactor first wall and blanket structural components cannot be proved, if all the possible failure modes are considered. Conversely, it is also true that no part of the existing data base shows the niobium base alloys to be deficient for this application. Therefore, more information needs to be developed particularly with respect to fatigue behavior, irradiation effects, and material compatibility before the question of the feasibility of niobium alloys for fusion is answered.

5.2.6 References

1. J. W. Davis, Economic Impact of Using refractory metals for fusion reactors, U.S. Department of Energy Report, COO-4247-1, Oct 1977.
2. R. E. Gold, et. al., "Technical Assessment of Vanadium-Base Alloy For Fusion Reactor Applications, U.S. Department of Energy Report, COO-4540-1, April 1978.

5.3 IRRADIATION INDUCED STRESS RELAXATION IN TITANIUM ALLOYS - R. E. Nygren (Hanford Engineering Development Laboratory)

5.3.1 ADIP Task

Task Number I.C.8.1 - Irradiation Creep Response of Scoping Set of Research Alloys.

5.3.2 Objective

The objective of this study was a preliminary estimate of neutron irradiation creep rates in titanium alloys.

5.3.3 Summary

Neutron irradiation creep rates were determined by stress relaxation measurements on four titanium alloys, Ti-6Al-4V (in three heat treat conditions) Ti-6242S, Ti-5621s and Ti-15-333. The superalpha alloy Ti-5621s had the greatest creep strength and the beta alloy Ti-15-333 was weakest. The calculated irradiation creep coefficients ranged from 7 to 51 x 10^{-30} $(psi\text{-}n/cm^2)^{-1}$ or 1 to 7 x 10^{-27} $(MPa\text{-}n/cm^2)^{-1}$. The data were obtained using bent beam type specimens irradiated in EBR-II (Row VII) to a fluence of .34 x 10^{22} n/cm^2 (E > 0.1 MeV) at about 840°F.

5.3.4 Progress and Status

The development of suitable structural materials for fusion reactors will require an understanding of the effects of intense neutron radiation on the mechanical properties of these materials. Materials irradiations in fission reactors will be the major near-term source of data. The present data base consists primarily of radiation effects studies in the FBR industry on stainless steels and some high strength Fe-Ni-Cr alloys. However, some materials, such as titanium alloys, that offer potential as first wall candidate materials[1] have not been studied in the FBR industry. Very little information on radiation effects exists for these materials and for titanium in particular. The only previous information on irradiation creep of titanium alloys was a single sample irradiated with 16 MeV protons.[2] Thus, scoping studies such as the Ti Creep Experiment reported here are a necessary starting point.

5.3.4.1 Experimental Procedure

The irradiation creep coefficients for several titanium alloys were estimated by measuring the change in shape of mandrel-loaded beams due to stress relaxation during neutron irradiation in EBR-II. Figure 1 is a cross-sectional view of a mandrel and specimens. The specimens were small rectangular coupons (2.0 x .25 x .040 inches or *5.0* x *.64* x .102 cm) and were flat prior to being loaded into the mandrels. The mandrels imposed a uniform radius of curvature on the specimens. During irradiation the bending stresses in the specimens relaxed due to irradiation creep. Comparing the residual curvature of the specimens, after they were removed from the mandrels, with the curvature of the mandrels provided a measure of stress relaxation from which neutron irradiation creep coefficients were calculated. Wire and Straalsund[3] have used this technique to compare neutron irradiation creep in *304* SS specimens with different irradiation histories. The technique is excellent as a comparative tool because within each mandrel the individual specimens all undergo the same loading deflections and the same irradiation conditions.

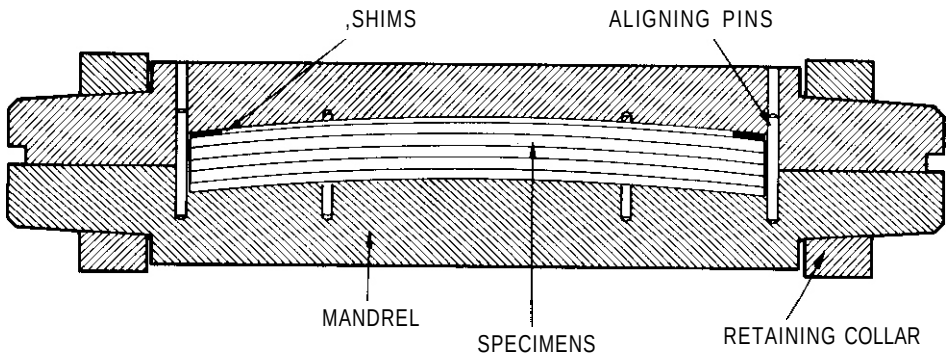

HEDL 7604-178.9

Figure 1: Cross-sectional view of mandrel with specimens.

5.3.4.2 Irradiation Conditions

The test consisted of two pins, HEDL numbers B-277 and B-278, placed in assembly X217D and in position 7D3 in Row VII of EBR-II during Run 92 (2444 megawatt days). The accumulated fluence of the specimens was .34 x 10^{22} n/cm^2 (E > 0.1 MeV). This value of fluence is based on previous characterizations rather than in-situ dosimetry. The equivalent damage parameter is 1.5 dpa.[4] The specimens in each pin were contained in two mandrels placed in the mid-core region where the flux profile is fairly flat. The specimen centers were 1.6 inches (4.1 cm) above and below the core midplane and the portion of the specimens furthest from midplane still received about 95% of the peak flux. The pins were single-walled, sodium-filled capsules. The specimen temperatures were about 65°F (36°C) above the ambient temperature of the reactor coolant. The estimated irradiation temperature of the specimens is 840°F ± 50° (449°C). The large uncertainty in temperature is typical of uninstrument tests in EBR-II.

5.3.4.3 Materials

This experiment compared the irradiation creep behavior of four titanium alloys: Ti-6Al-4V, Ti-6242S, Ti-5621s and Ti-15-333. Three heat treat conditions of Ti-6Al-4V were used. Tables I and II give the alloy compositions and the heat treatments. The McDonnell-Douglas Company prepared the specimens from sheet stock obtained from Titanium Metals Corporation and from RMI. These alloys are the titanium alloy group identified as base research alloys in the national fusion program. Basically, they represent a range of commercially available alloys used primarily in the aerospace industry.

The microstructure of irradiated specimens and archive samples will be the subject of future work. Only a few explanatory remarks will be given here.

Pure titanium is allotropic. The high temperature phase has a body-centered-cubic structure (β) and the low temperature phase is hexagonal (α). Various alloying additives are used as phase stabilizers. Strengthening is most effective in the α phase both by solid solution strengthening and by precipitation. Ti-6242s and Ti-5621s are super-alpha alloys. Both contain substantial amounts of aluminum, tin, zirconium and silicon

TABLE 1
Alloy Compositions

Alloy	Composition	
Ti-6Al-4V	Al - 6.08 %	O - 0.10
	V - 3.71	N - 0.01
TiMet heat V-5412		Fe - 0.09
Ti-62425	Al - 5.8 %	C - *0.022*
	Mo - *2.0*	O - 0.13
TiMet heat N5122	Zr - 4.0	N - 0.015
	Sn - 2.0	H - 0.008
	Si - 0.08	Fe - 0.06
Ti-5621s	Al - 5.2 %	C - *0.02*
	Sn - 5.9	D - 0.113
RMI heat 303021	Zr - 1.9	N - 0.009
	Mo - 0.84	H - 0.0035
	Si - 0.27	Fe - 0.05
Ti-15-333	V - 15.3 %	O - 0.16
	Cr - 3.04	N - 0.01
TiMet heat V-5295	Al - 3.11	Fe - 0.17
	Sn - 2.0	Zr - <.05

TABLE II
Heat Treatments

1.	Ti-6Al-4V	Mill Anneal	a. 730°C/2hr. - A.C.
2.	Ti-6Al-4V	Beta Anneal	a. 1040°C/30 min - A.C. h. 730°C/2 hr. - A.C.
3.	Ti-6Al-4V	Duplex Anneal plus Overage (DUP)	a. 940°C/10 min. - Argon Q. h. 675°C/4 hr. - A.C.
4.	Ti-6242s		a. 900°C/30 min. - A.C. h. 790°C/15 min. - A.C.
5.	Ti-5621s		a. 950°C/15 min. - A.C. b. 600°C/2 hr. - A.C.
6.	Ti-15-333		a. 760°C/15 min. - A.C. b. 510°C/16 hr. - A.C.

plus the interstitials oxygen, carbon and nitrogen. Aluminum and the interstitials are potent alpha stabilizers while tin and zirconium are primarily solid-solution strengthening agents.[5,6] Silicon specifically has been found to increase creep strength.[5] Ti-15-333 is a beta alloy and contains a large amount of the beta stabilizer vanadium. Ti-6Al-4V contains both a strong beta stabilizer, aluminum, and a strong beta stabilizer, vanadium. Consequently, the two phase region ($\alpha + \beta$) extends over a wide temperature range and the alloy exhibits a variety of possible microstructures. Three heat treatments of Ti-6Al-4V were used in this experiment: mill anneal, beta anneal and duplex anneal plus overage (DUP).

5.3.4.4 Measurements

The measurement device was a translating table that moved laterally under a vertical LVDT as shown in Figure 2. The LVDT measured the relative height of points on the specimen's surface (vertical displacement) and a

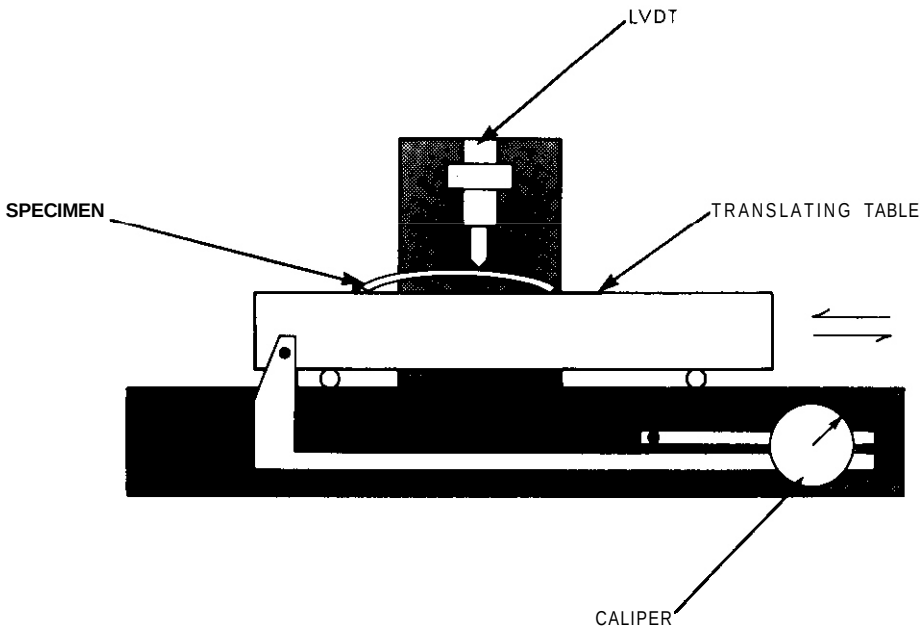

HEDL 7807 - 048.1

Figure 2: Simplified sketch of measurement system.

caliper mounted on the translating table indicated the lateral position (horizontal displacement). Thirty measurements were taken at increments of .050 inch (.127 cm) of horizontal displacement along the length of the specimen. Standards were measured intermittently to reconfirm the calibration of the LVDT. Estimated accuracy of the measurement system is ±.0001 inch (.00025 cm) which corresponds to ± 270 psi (1.9 MPa) in the calculated residual stress.

5.3.4.5 Analysis

The analysis contains two basic elements. The first is the elastic loading imposed on the specimens by the mandrels and the second is the fluence dependent stress relaxation that occurs during irradiation.

The mandrels elastically bent the specimens to conform to a specified radius of curvature R_m. The specimens were thin plates; consequently, the fiber strain across the width of a specimen was essentially zero (plane strain). Also, the through thickness stresses were neglibible compared to the fiber stresses. With these assumptions the stress state was easily derived. The maximum longitudinal fiber stress, σ_x, occurred at the outer (convex) surface and is given by Equation [1].

$$\sigma_x(0) = \frac{E}{1-\nu^2} \quad \frac{t}{2R_m} \qquad [1]$$

where E is the Young's Modulus

v is poisson's ratio

t is the specimen's thickness

R_m is the mandrel's curvature

(0) indicates zero fluence, i.e., the loading conditions prior to irradiation.

When the specimenswereremoved from the mandrels after irradiation they retain some curvature. The amount of retained curvature corresponds exactly to the amount of stress relaxed σ_x^* during irradiation using Equation [1]. Equation [2] restates this relationship in terms of the specimen's radius of curvature R and Equation [3] gives the residual stress in the specimen prior to its removal from the mandrel.

$$\sigma_x^* = \frac{Et}{2(1-\nu^2)} \frac{1}{R} \qquad [2]$$

$$\sigma = \sigma(0) - \sigma^* = \qquad [3]$$

Equation [4] gives the stress relaxation in terms of the irradiation creep coefficient B, the fluence ϕt and material parameters.

$$\frac{\sigma_x}{\sigma_x(0)} = \frac{1+\nu}{2} \exp\left[\frac{-BE\phi t}{2(1-\nu)}\right] + \frac{1-\nu}{2} \exp\left[\frac{-3BE\phi t}{2(1+\nu)}\right] \qquad [4]$$

The derivation is presented elsewhere[3] and is straightforward using the assumptions of Hooke's law, plane strain and a constant coefficient of irradiation creep. The two terms (relaxation times) in Equation [4] correspond respectively to the dilatative stress term $(\sigma_x + \sigma_y)$ and the deviatoric stress term $(\sigma_x - \sigma_y)$ that evolve in the derivation.

Values of B were determined from the stress relaxation data by plotting Equation [4] with the stress relaxation as the ordinate and B as the abscissa as shown in Figure 3. Appropriate values of B were then estimated and confirmed by calculation.

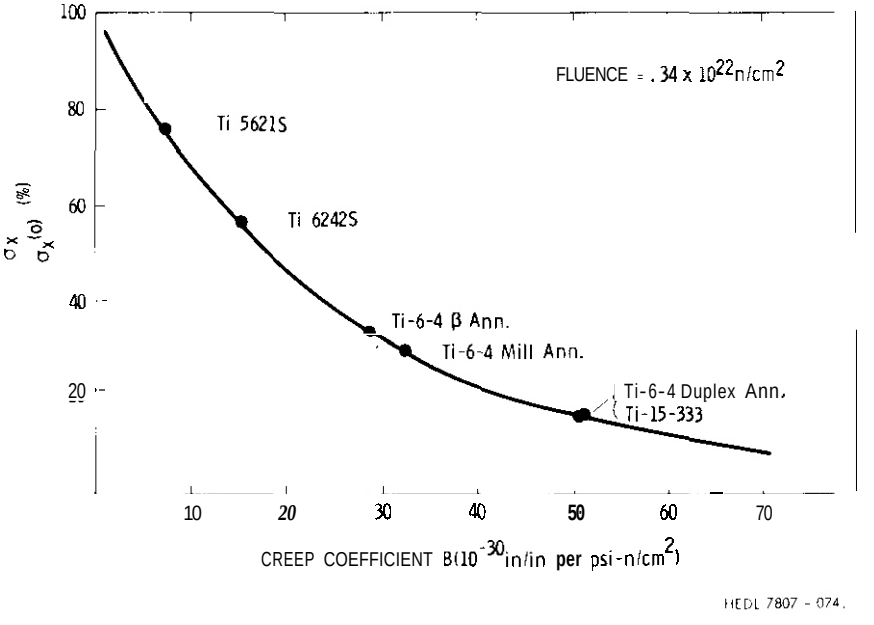

Figure 3: Residual stress versus average creep coefficient Equation [4] at constant fluence.

5.3.4.6 Results

The superalpha alloys Ti-5621s and Ti-6242s had the greatest creep strengths (lowest coefficients) and the beta alloy Ti-15-333 had the least. Table III gives the data. The "no data" points (--) in Table III reflect the selections of five specimens for each mandrel from the six alloy conditions. The stresses indicated below the radii of the mandrels are the maximum fiber stresses initially present in the specimens at the irradiation temperature 840°F (449°C).

TABLE III
Ti Creep Experiment - Stress Relaxation Data
Percent Relaxation of Stress

Mandrel Radius (in) Stress	1 25.0 (10 ksi) (69 MPa)	2 16.7 (15 ksi) (103 MPa)	3 10.0 (25 ksi) (172 MPa)	4 8.3 (30 ksi) (207 MPa)	Ave. Relax.	$\frac{\sigma_x}{\sigma_x(0}$
Ti-5621S	25%	22%	21%	27%	24%	76%
Ti-6242s	49%	38%	45%	44%	44%	56%
Ti-6-4 Beta Ann.	69%	66%	66%		67%	33%
Ti-6-4 Mill Ann.		70%		73%	71%	29%
Ti-6-4 Duplex Ann.	94%		81%	81%	85%	15%
Ti-15-333	(109%)	80%	87%	88%	85% (91%)	15%

The limited high temperature data on these alloys showed small variations among alloys. Consequently, the material constants reported for Ti-6Al-4V[7,8] were used to evaluate Equation [4] for all alloys. The estimated values of the irradiation creep coefficients are given in Table IV.

The accuracy of these results were influenced by three major factors, two of which relate directly to the measurements and calculations. First, the comparison of the irradiation creep coefficients between alloys as a relative measure depend only on the accuracy of the measurement system. The previously quoted measurement accuracy of .0001 inch produces the largest uncertainties in B values for the 10 psi mandrel. In this case

the error is 3 to 5 ($\times 10^{-30}$) as indicated in Table IV. The error ranges for the higher stress mandrels are proportionately less.

TABLE IV
Ti Creep Experiment - Irradiation Creep Coefficients

Yaterial	Irradiation Creep Coefficient B	
	10^{-30}(psi-n/cm^2)$^{-1}$	10^{-27}(MPa-n/cm^2)$^{-1}$
Ti-5621s	7 (±4)*	1.0
Ti-6242s	15 (±3)	2.2
Ti-6Al-4V Beta Ann.	29 (±3)	4.2
Ti-6Al-4V Mill Ann.	33 (±4)	4.8
Ti-6Al-4V Duplex Ann.	51 (±6)	7.4
Ti-15-333	51 (±6)	7.4

*Error estimates for 10 ksi mandrel.

The second limit in accuracy arises from less well-defined uncertainties in the material parameters and the fluence. The Ti Creep Experiment was irradiated in an uninstrumented position in EBR-II. Consequently, the accumulated fluence and the irradiation temperature and known only within the rough bounds typical of such tests. The uncertainty in the estimated fluence is about ± 20% and the uncertainty in the irradiation temperature combined with the uncertainty in material parameters at high temperature produces a gross uncertainty of at least 10% in the material parameters. The lumped effect of this second type of uncertainty is roughly ± 50% in the absolute value of B.

A more general concern with the approach taken here is the possibility that primary creep transients may occur. This subject is discussed in the following section.

5.3.4.7 Discussion

A comparison of the irradiation creep behaviors of the titanium alloys with that of CW 316 SS is useful here both as a reference point and as a vehicle for discussing transient creep effects. The appropriate data

on CW 316 SS for this comparison are from the low fluence beam bending experiment conducted by GE.[9] The GE specimens were also flat beams and were irradiated at about 800°F (425°C).

The beam bending data on CW 316 SS indicates that a significant primary transient occurs. If a constant coefficient of irradiation creep is assumed (average irradiation creep coefficient B), then the observed value of creep strain at a fluence of .34 x 10^{22} n/cm^2 corresponds to a $\overline{B}$ of about 3 x 10^{-29} (psi-n/cm^2)$^{-1}$ or 4 x 10^{-27}(MPa-n/cm^2)$^{-1}$. This low fluence value is about six times greater than the steady state value observed at a higher fluence and about ten times greater than the steady state irradiation creep coefficient determined using pressurized tubes. Using this low fluence value of the average irradiation creep coefficient placed CW 316 SS roughly in the middle of the $\overline{B}$ values for the titanium alloys. The titanium alloys weakest in creep, Ti-15-333 and Ti-6Al-4V in the DUP condition, had average irradiation creep coefficients roughly a factor of two greater (weaker) than CW 316. The other two heat treatments of Ti-6Al-4V, the beta annealed and mill annealed conditions, were about equal to the low fluence average creep coefficient for CW 316. Both the super alpha alloys (actually near alpha alloys) Ti-5621s and Ti-6242s had lower (stronger) average irradiation creep coefficients than CW 316. The coefficients for Ti-6242s and Ti-5621s are respectively one-half and one-quarter that of CW 316.

The irradiation creep behaviors of Ti-6Al-4V (DUP) dnd CW 316 SS at low doses have been compared directly using 14.8 MeV protons" and the results support the comparison above. The transient creep behaviors of the two materials were similar and the irradiation creep coefficients differed by roughly a factor of two which is consistent with the comparison made above.

5.3.5 Conclusions

The average irradiation creep coefficients of the various titanium alloys tested were spread within one order of magnitude. The observed irradiation creep behavior of the titanium alloys is similar to that observed in CW 316 at low fluences.

5.3.6 References

1. McDonnell-Douglas Astronautics Company, *Assessment of Titanium for Use in the 1st Wall/Blanket Structure of Fusion Powers Reactors,* EPRI ER-386 (Project 472-1), April 1977.
2. E. K. Opperman, "16 MeV Proton Creep in a Ti-6Al-4V Specimen," *Alloy Development for Irradiation Performance Progress Report,* DOE/ET-2058/1 (1978).
3. G. L. Wire and J. L. Straalsund, "Irradiation Induced Stress-Relaxation of Previously Irradiated 304 Stainless Steel in a Fast Flux Environment," *Journal of Nuclear Materials,* 64:254-264 (1977).
4. T. A. Gabriel, J. A. Amburgey, N. M. Greene, "Radiation-Damage Calculations: Primary Recoil Spectra, Displacement Rates and Gas-Production Rates," *Nuclear Science Engineering,* 61: 21-32 (1976).
5. C. Hammond and J. Nutting, "The Physical Metallurgy of Superalloys and Titanium Alloys," *Metal Science,* 11:10:474-490 (1977).
6. R. A. Wood and R. J. Favor, *Titanium Alloys Handbook,* December 1972, MCIC-NB-02, pp 1-6:72.
7. IBID, pp1-4:72.
8. ASM, *Metals Handbook Vol. Ed. 8,* pp 537.
9. A. J. McSherry, M. R. Patel, J. Marshall and E. R. Gilbert, "Irradiation Creep in Bending of CW AISI 316 at Low Fluence," *Transactions ANS - 1978 Annual Meeting,* 28:146 (June 1978).
10. E. K. Oppermand and J. L. Straalsund, "Proton Simulation of Irradiation Induced Creep in 20% Cold Worked AISI 316 Stainless Steel," presented at the *9th ASTM International Symposium - Effects of Radiation on Structural Materials,* July 11-13, 1978, Richland, Washington.

Acknowledgement

I wish to thank John Davis of the McDonnell-Douglas Company for providing the specimens for this experiment.

6. PATH D ALLOY DEVELOPMENT — INNOVATIVE MATERIAL CONCEPTS

Innovative material concepts are included as a path in the alloy development program because the fusion reactor environment is extremely demanding on materials in the high-flux region and the more conventional materials and metallurgical concepts may not be adequate. Novel approaches to alloy design, nonconventional material processing to tailor properties, or alternate materials such as structural ceramics and fiber composites will be considered.

6.1 EFFECT OF ^{4}He AND ^{3}H ON THE TENSILE PROPERTIES OF SAP — P. J. Maziasz and K. Farrell (ORNL)

6.1.1 ADIP Tasks

ADIP Tasks I.B.16, Tensile Properties of Special and Innovative Materials, and I.C.5, Microstructure and Swelling in Special and Innovative Materials.

6.1.2 Objective

The objective of this work is to examine the effect of producing and dispersing large quantities of ^{4}He and ^{3}H on the mechanical properties swelling and microstructure of SAP at high temperatures.

6.1.3 Summary

Sintered Aluminum Product (SAP) has been doped with ^{6}Li and irradiated in HFIR to produce ^{4}He and ^{3}H at concentrations of 13, 270, and 1700 at. ppm and 2.0—6.7 dpa.

The specimens were annealed at 300, 400, and 500°C for 1000 h after irradiation. Tensile testing (at the annealing temperatures) revealed little or no degradation in strength up to 1700 at. ppm ^{4}He and no loss of total elongation up to 270 at. ppm ^{4}He. Immersion density results show essentially no swelling at any ^{4}He level. Microstructural examination reveals that the lack of effect of the gas is due to its being accommodated in small, elongated cavities at the Al_2O_3-Al interfaces. However, the oxide levels obtained in the material are 17 to 25 wt %, well above levels that would be used in SAP for structural applications. As a result, the high-temperature total elongation, both irradiated and unirradiated, is quite low. If work on SAP is to be pursued, the irradiation resistance of SAP with lower oxide levels needs to be examined.

6.1.4 Progress and Status

The SAP specimens irradiated in HFIR were fabricated by four general steps. Powders of aluminum containing lithium were prepared, consolidated into billets, extruded into bar stock, and machined into tensile specimens. The SAP was doped with lithium about 94 at. % enriched in ^6Li to approximate concentrations of 0, 15, 300, and 1870 at. ppm ^6Li. The ball-milling procedure was designed to yield 11.5 wt % Al_2O_3 so that the alloy would nominally be SAP 895; however, chemical analysis indicated that 17 to 24 wt % Al_2O_3 had been produced. The tensile specimens were irradiated in HFIR at reactor coolant temperature (55°C) to a fluence of 1.4 to 4.6 x $10^{25} n/m^2$ (>0.1 MeV) to produce a calculated ^6Li burnup of 94 to 99+ % via the reaction

$$^6Li + n \rightarrow {}^4He + {}^3H$$

and 2.0 to 6.7 dpa. Table 6.1.1 shows the measured Al_2O_3 content, the measured ^6Li level, the measured ^4He level, and the calculated ^6Li level necessasry to produce the measured helium. The measured ^6Li was determined by wet chemistry for only the aluminum matrix, and the difference in measured and calculated ^6Li indicates that significant ^6Li was tied up in the oxide also. Following irradiation, samples at all ^4He levels were annealed at 300, 400, and 500°C for 1000 h to disperse the gas produced during irradiation.

The tensile properties of unirradiated aged and unaged samples are reported in Table 6.1.2 and shown in Figs. 6.1.1 and 6.1.2. Tensile tests were conducted at various temperatures at a strain rate of 0.0023/min. The tensile properties of irradiated material, aged and unaged, are reported in Table 6.1.3 and shown in Figs. 6.1.3 through 6.1.5. The unirradiated strength and ductility are consistent with Copeland's datal extrapolated to oxide contents comparable to this work. Increases in strength are directly attributable to finely dispersed oxide flakes.2 Transmission electron microscopy confirms a fine distribution even at the high oxide levels achieved in these samples.

Table 6.1.1. Amount of Al_2O_3, ^6Li, and ^4He in Each *SAP* Batch

Batch	Al_2O_3 (wt %)[a]	Concentration, at. ppm		
		^6Li[a]	^4He[b]	^6Li[c]
1	20.0	0	0	0
2	17.3	6.0	13.0	14
3	17.7	200	270	290
4	24.5	725	1700	1800

[a] Measured by chemical analysis.

[b] Measured by mass spectrometry.

[c] Calculated amount of ^6Li necessary to produce measured ^4He based upon 94+ % conversion according to the reaction $^6Li + {}^1n \rightarrow {}^4He + {}^3H$.

Table 6.1.2. Engineering Mechanical Properties of Unirradiated SAP for Various Lithium Levels

Batch	^6Li (at. ppm)	Test Temperature (°C)	Stress, MPa[a]		Elongation, %	
			Yield	Ultimate Tensile	Uniform	Total
		As Received				
1	0.0	37	343	435	1.69	1.69
		37	358	448	1.57	1.57
		37	347	443	2.07	2.07
		31	354	463	1.35	1.35
		150	283	321	1.36	1.36
		300	194	207	0.60	0.72
		500	66	66	0.12	0.12
2	6.0	37	397	474	2.49	3.06
		150	317	344	1.23	2.42
		300	202	207	0.28	0.28
		300	206	211	0.48	0.48
		400	144	144	0.18	0.18
3	191	150	255	288	2.41	3.16
		400	143	150	0.60	0.60
4	725	37	418	474	1.77	2.58
		150	312	339	1.29	2.44
		300	208	218	0.59	0.59
		400	155	158	0.30	0.30
		400	150	157	0.52	0.52
		500	97	97	0.10	0.10
		Aged 1000 h at the Test Temperature				
2	6.0	300	222	226	0.43	0.43
		500	74	74	0.24	0.33
3	191	300	212	220	0.55	0.89
		400	157	157	0.22	0.22
		500	83	83	0.10	0.10
4	725	300	195	202	0.45	0.45
		400	158	158	0.10	0.10

[a] Multiply by 145 psi/MPa to convert to psi. All tests run at 0.8 μm/s crosshead speed.

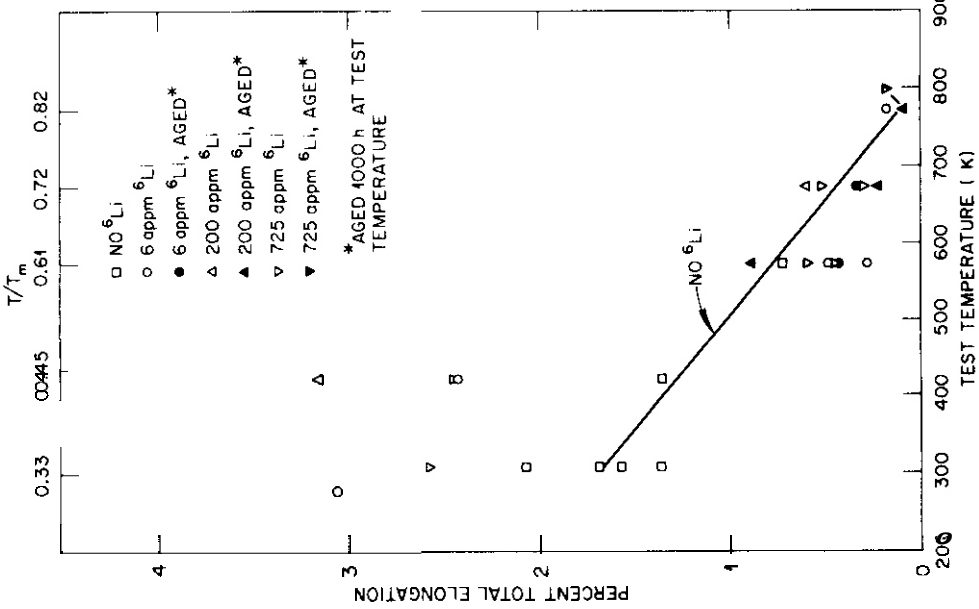

Fig. 6.1.2. Total Tensile Elongation as a Function of Test Temperature for Unirradiated SAP.

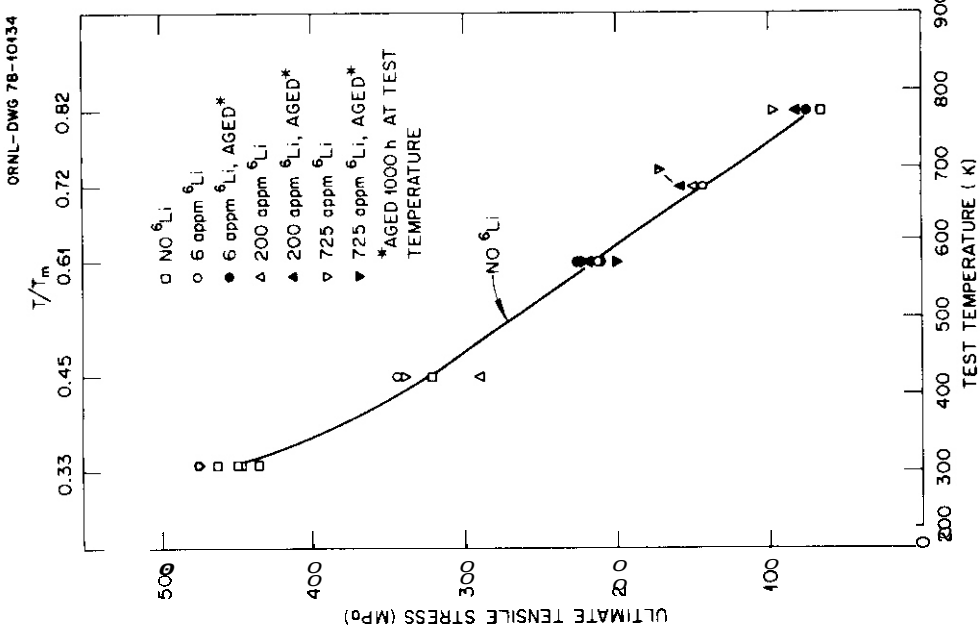

Fig. 6.1.1. Ultimate Tensile Strength for Unirradiated SAP as a Function of Test Temperature.

Table 6.1.3. Postirradiation Engineering Mechanical Properties of SAP for Various Helium Levels

Batch	^{4}He (at. ppm)	Test Temperature (°C)	Stress, MPa		Elongation, %	
			Yield[a]	Ultimate Tensile	Uniform	Total
			As Irradiated			
1	0	37	302	517	1.42	1.42
		400	182	185	0.2	0.2
		400	118	151	0.47	0.47
2	13.3	400	146	156	0.47	0.47
		400	150	155	0.27	0.27
3	268	37	341	514	4.5	4.5
		150	287	364	2.9	2.9
		400	191	217	0.58	0.58
4	1684	300	198	198	0.06	0.06
		500	98	98	0.124	0.124
		Irradiated and Aged 1000 h at 300°C				
2	13.3	300	228	260	0.68	0.68
3	268	300	221	269	0.78	0.78
		300	219	241	0.41	0.41
4	1684	300	234	234	0.12	0.12
		Irradiated and Aged 1000 h at 400°C				
1	0	400	158	165	0.36	0.36
		400	152	165	0.53	0.53
		400	145	153	0.38	0.38
2	13.3	300	214	224	0.59	0.59
		400	145	153	0.38	0.38
3	268	300	180	203	0.59	0.59
		400	143	143	0.27	0.27
		400	149	166	0.44	0.44
		400	140	150	0.37	0.37
		500	93	96	0.29	0.29
4	1684	400	163	163	0.19	0.19
		400	154	154	0.08	0.08
		400	146	146	0.02	0.02
		Irradiated and Aged 1000 h at 500°C				
2	13.3	500	74	78	0.35	0.35
3	268	500	67	67	0.20	0.20
		500	71	71	0.12	0.12
4	1684	500	98	98	0.124	0.124
		500	82	83	0.24	0.24

[a]Multiply by 145 psi/MPa to convert to psi. All tests run at 0.0023/min strain rate.

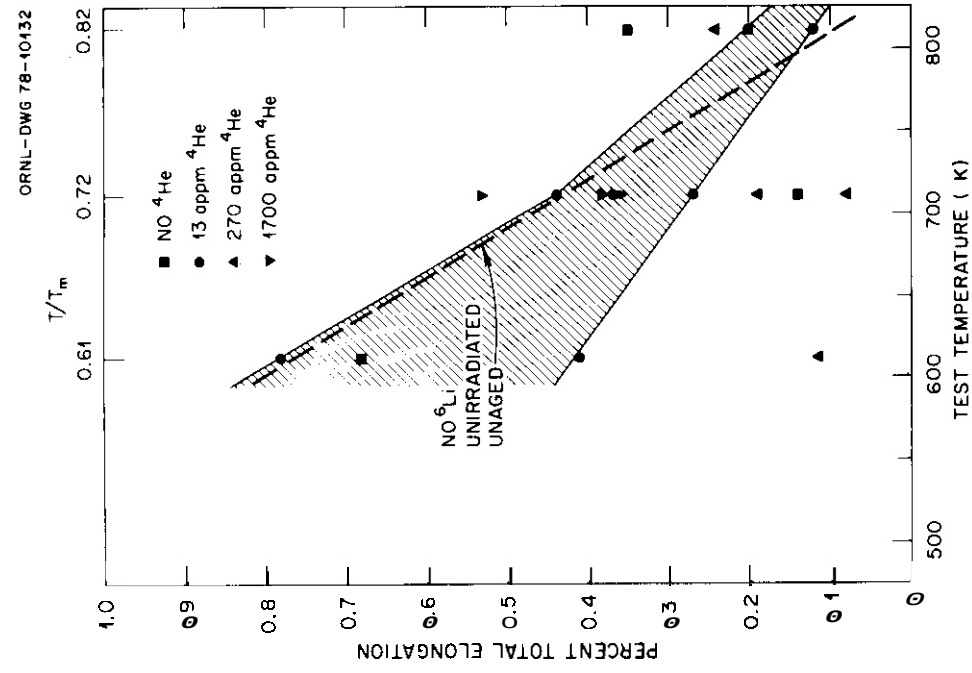

Fig. 6.1.4. Total Tensile Elongation as a Function of Test Temperature for SAP Irradiated in HFIR.

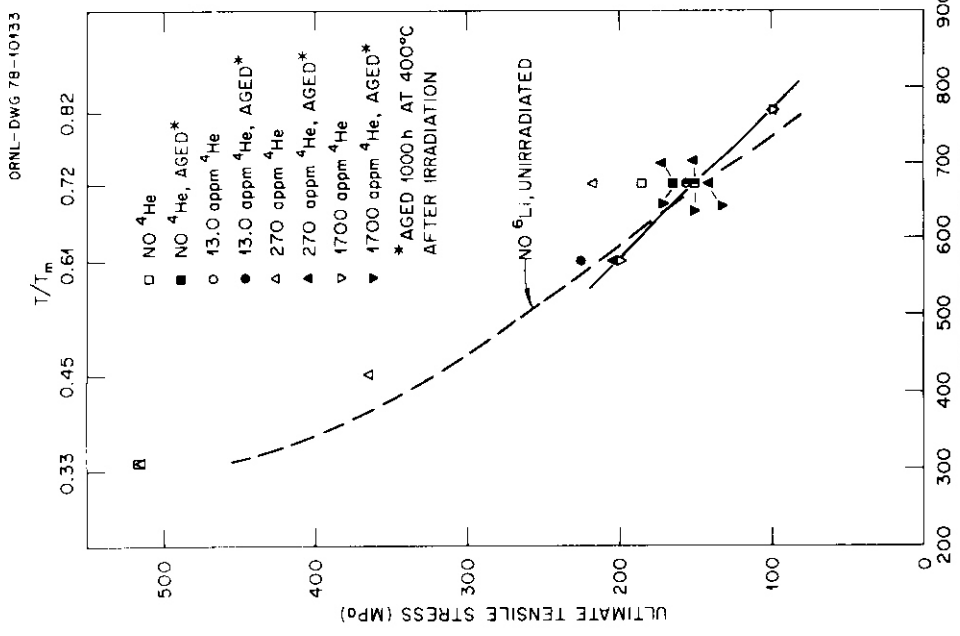

Fig. 6.1.3. Ultimate Tensile Strength as a Function of Test Temperature for SAP Unirradiated in HFIR.

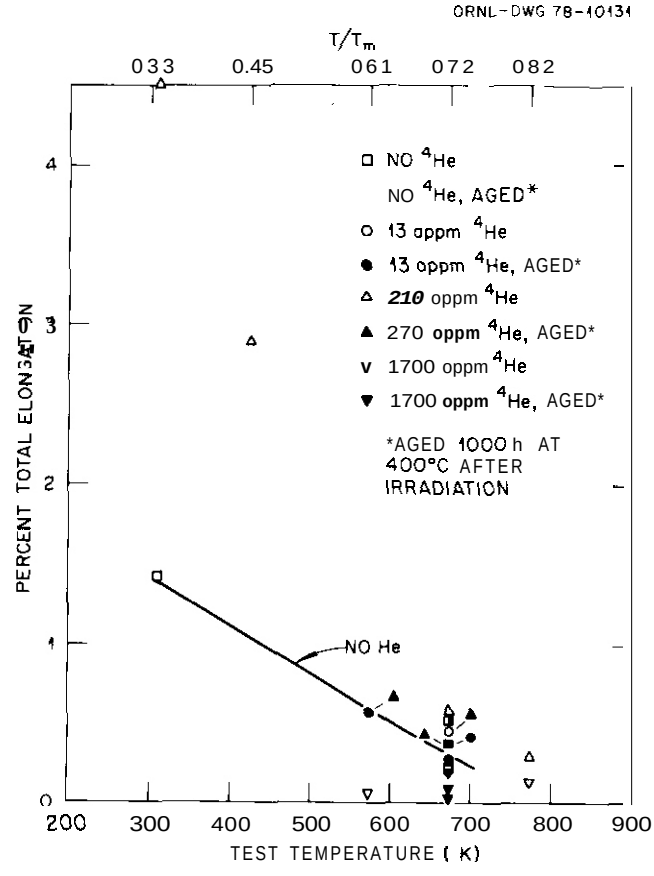

Fig. 6.1.5. Total Elongation as a Function of Test and Aging Temperature for SAP Irradiated in HFIR.

In the unirradiated material shown in Figs. 6.1.1 and 6.1.2, strength and elongation decrease with increasing temperature. Harman and Nolan[3] characterized the fracture of SAP as beginning with void formation at large oxide agglomerates, followed by tearing and separation, with final failure occurring by shear. At low temperatures shear predominates and at high temperatures separation and tearing predominate. The SAP examined in this work showed behavior consistent with these trends.

Examination of Figs. 6.1.3 and 6.1.4 shows that production of gas by neutron irradiation and dispersion of the gas by postirradiation annealing at *400°C* for **1000** h produced little or no effect on strength and ductility relative to unirradiated material for gas contents up to 270 at. ppm ^{4}He. Figure 6.1.5 shows the ductility after postirradiation annealing at **300,** *400,* and *500°C* for **1000** h followed by tensile

testing at the aging temperature. Both Figs. 6.1.4 and 6.1.5 show a slight reduction in ductility outside the data scatter for a gas content of 1700 at. ppm ^4He.

The fracture surface of a sample containing 270 at. ppm ^4He postirradiation annealed for 100 h at 400°C and tensile tested at 400°C is shown in Fig. 6.1.6. Figure 6.1.6(b) indicates ductile dimple failure on a fine scale, similar to the fracture behavior observed by Harman et al.[3] in unirradiated SAP.

Immersion density measurements before and after irradiation and after postirradiation annealing show no detectable swelling at any gas level. Figures 6.1.7 and 6.1.8 show the microstructures of SAP containing 270 and 1700 at. ppm ^4He, respectively, after postirradiation aging at 400°C for 1000 h. Both show trapping of the gas in fine, irregularly shaped cavities at Al-Al_2O_3 interfaces. This trapping on a fine scale would be expected to produce little swelling and is consistent with the immersion density measurements and the retention of preirradiation ductility values up to 270 at. ppm ^4He. Figure 6.1.8 indicates that cavities are beginning to form at the aluminum grain boundaries. This is consistent with the small ductility loss shown by the samples containing 1700 at. ppm ^4He. Examination of as-irradiated samples indicates no resolvable cavities. The observed formation of cavities on Al_2O_3 particles during annealing is consistent with similar results reported by Ruedl[4] for about 1000 at. ppm ^4He in irradiated SAP containing 2.5 wt % Al_2O_3. The trapping of gas at Al_2O_3 is also indicated by the ^3H release measurements performed by Talbot and Wiffen.[5] These measurements were conducted on the same material used in this work, but were irradiated to a lower fluence producing less ^4He and ^3H, followed by gas release at temperatures from 383 to 500°C. These samples retained about 70% of the ^3H present, compared with pure aluminum containing similar ^3H levels, which released 99+% of the tritium at the same temperatures. The effect is not unexpected. in light of the cavities present at the Al-Al_2O_3 interfaces. The irregular cavities at Al-Al_2O_3 interfaces, the lack of swelling, and the retention of strength and ductility up to 270 at. ppm ^4He are all indicative of the effective microstructural accommodation of ^4He by Al_2O_3 in SAP.

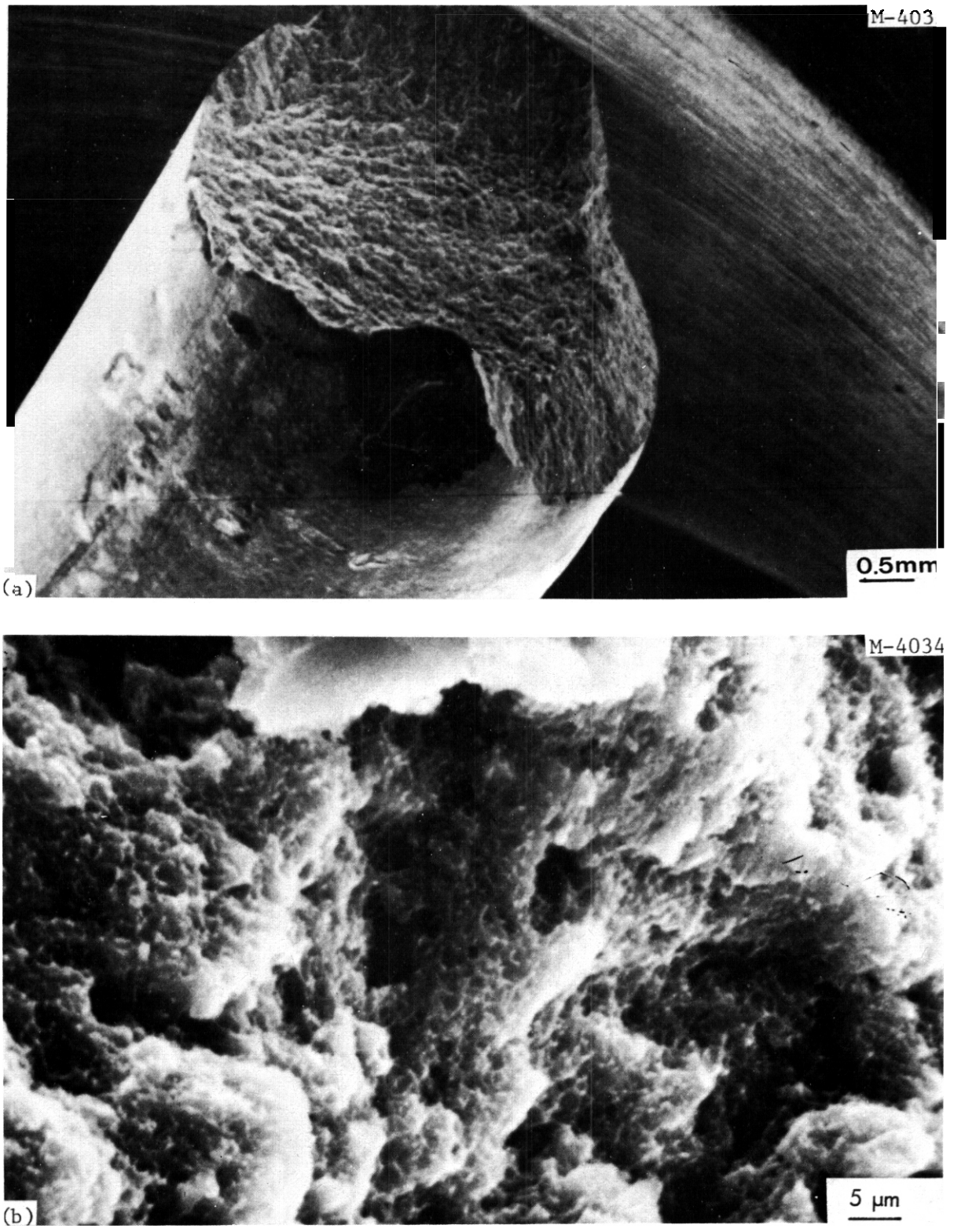

Fig. 6.1.6. Fracture Surface of SAP After Irradiation in HFIR at 55°C to Produce 270 at. ppm ^{4}He, Annealing at 400°C for 1000 h, and Tensile Testing at 400°C. (a) Low magnification of shear lip. (b) High magnification shows fine dimples indicative of ductile failure on a fine scale.

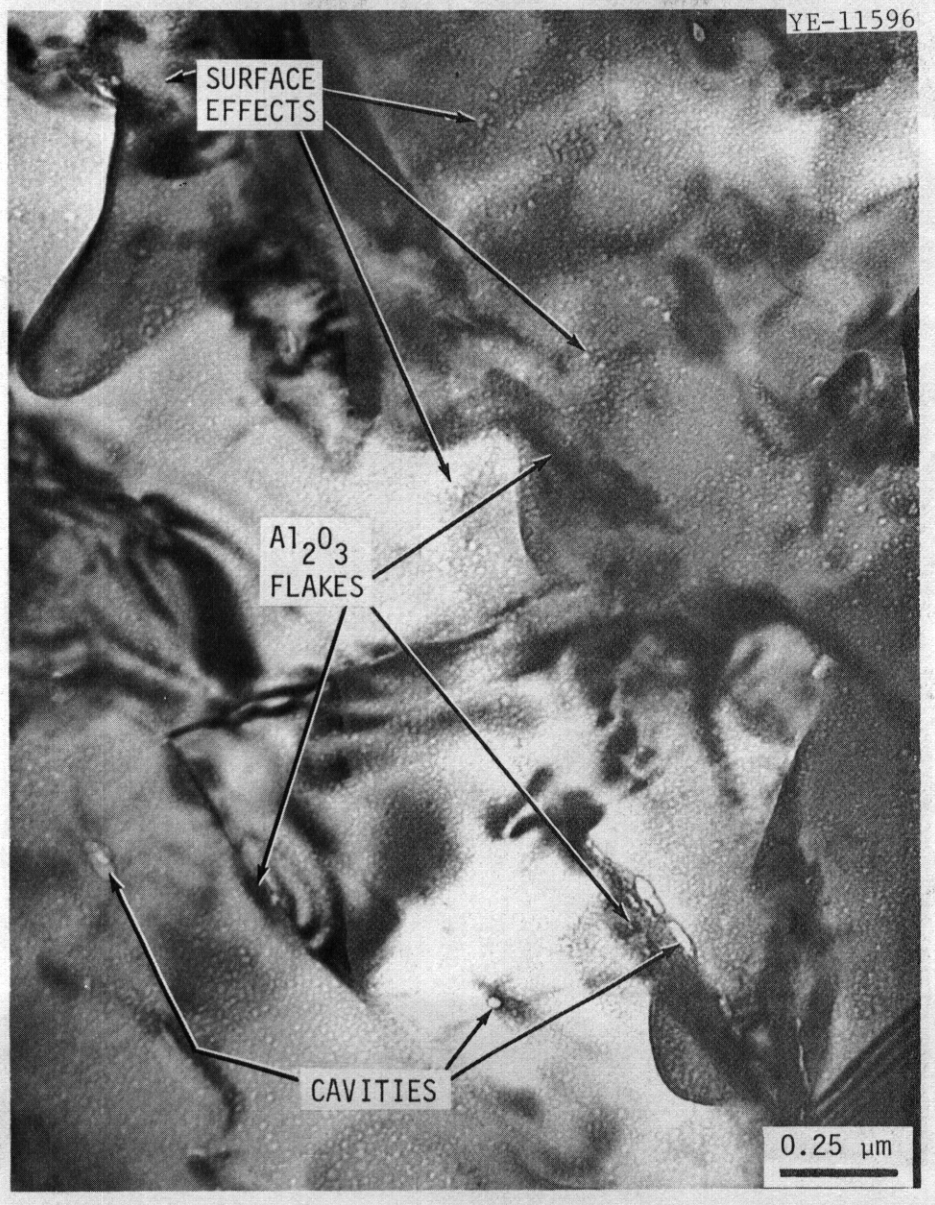

Fig. 6.1.7. Microstructure of SAP After Irradiation in HFIR at 55°C to Produce 270 at. ppm ^4He and Annealing at 400°C for 1000 h. Cavities are nearly exclusively associated with Al_2O_3 particles. What appears to be fine cavitation in the matrix is actually a surface artifact on only one surface as determined by stereomicroscopy.

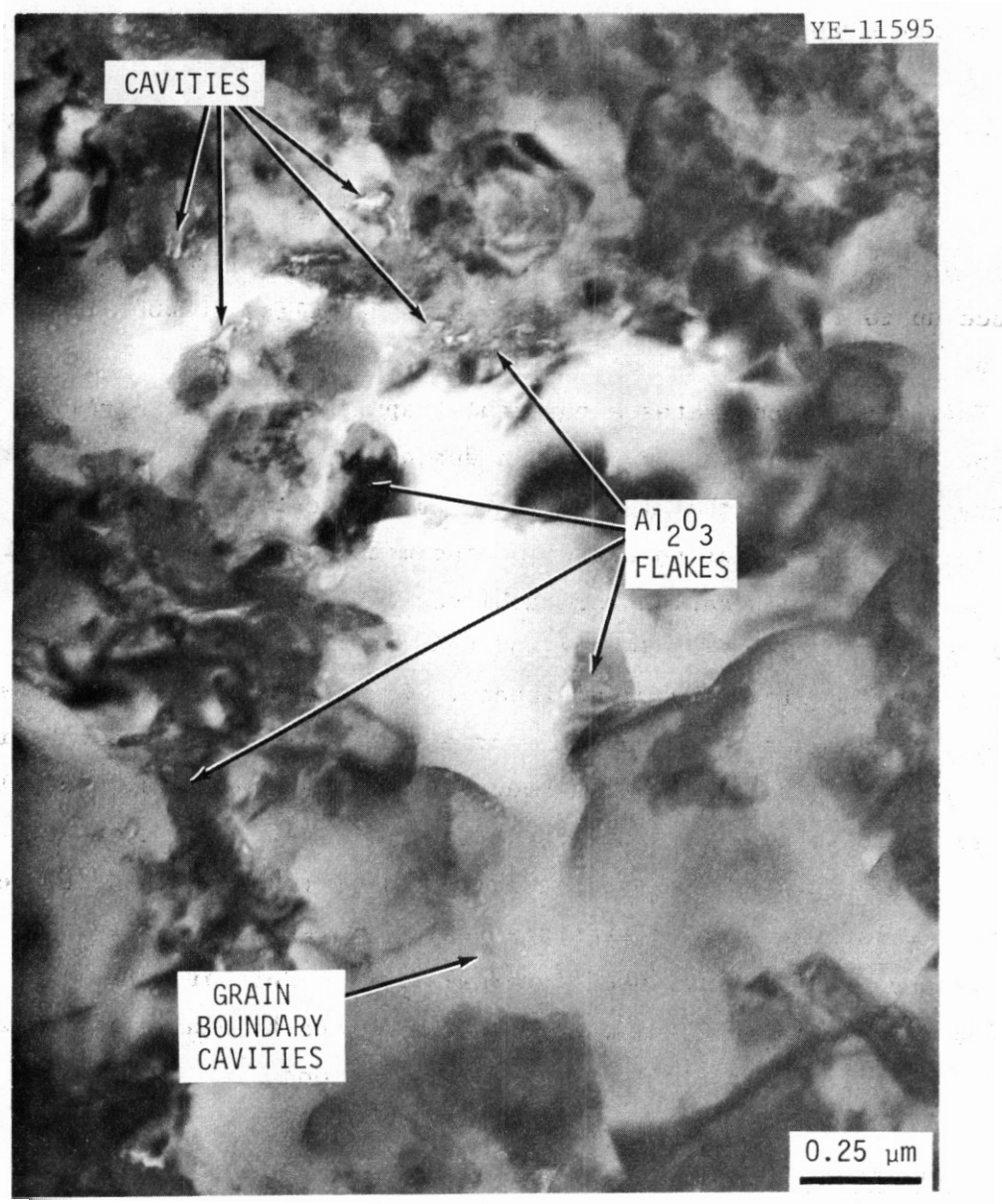

Fig. 6.1.8. Microstructure of SAP After Irradiation in HFIR at 55°C to Produce 1700 at. ppm ^4He and Annealing at 400°C for 1000 h. The same surface artifacts appear as in Fig. 6.1.7. Note cavities clustered about Al_2O_3 particles and cavities associated with aluminum grain boundaries.

6.1.5 Conclusions

1. Tensile strength of SAP is unaffected by up to 1700 at. ppm ^4He and ductility unaffected by up to 270 at. ppm for samples irradiated at about 55°C and aged at temperatures from 300 to 500°C.

2. Immersion density measurements reveal no swelling at any gas level after irradiation and postirradiation annealing.

3. Microstructural examination reveals fine trapping of ^4He in irregular cavities at the $Al-Al_2O_3$ interfaces after irradiation to produce up to 1700 at. ppm ^4He followed by annealing at 400°C for 1000 h.

This work demonstrates a powerful trapping effect of $Al-Al_2O_3$ internal interfaces for ^4He produced during irradiation. This fine dispersion of gas in the microstruture is manifest in little or no swelling and little nor no effect on the mechanical properties until very high gas concentrations are achieved. However, this material contained very high oxide levels and had very low ductility and as such, is of limited engineering significance. Work needs to be done to see if the effect can be maintained at lower oxide levels and at what helium level the effect saturates. Of course, the finest dispersion of Al_2O_3 is desired to produce optimum effect for any given oxide content. This work clearly supports the general principal of reducing the detrimental effects of large gas concentrations on the properties of metals by introducing finely distributed internal traps. Further work might consider incorporation of suitable internal (and hopefully intragranular) traps in metals desirable for fusion applications.

6.1.6 References

1. G. L. Copeland, *An Investigation of Alloying Effects in Aluminum Dispersion Strengthened with Al_2O_3.* Doctoral Dissentation, University of Tennessee, March 1975; ORNL-5088 (October 1975).

2. J. S. Benjamin and M. J. Bamford, "Dispersion Strengthened Aluminum Made by Mechanical Alloying," *Metall. Trans.* 8A: 1301 (1977).

3. D. G. Harman and T. A. Nolan, *Fracture of $Al-Al_2O_3$ Alloys: Fracture Analysis of the Commercial SAP-Type Alloy* ***XAP-001,*** ORNL/TM-1826 (July 1967).

4. E. Ruedl, "Direct Observation of Radiation Damage in $Al-Al_2O_3$ Alloys," pp. 171-83 in *Radiation Damage in Reactor Materials.* Vol. 1, International Atomic Energy Agency, Vienna, 1969.

5. J. B. Talbot and F. W. Wiffen, "Recovery of Tritium From Solid Lithium – Sintered Aluminum Product (SAP) and Lithium Aluminum Alloys," submitted to *Journal* of *Inorganic and Nuclear Chemistry.*

/. STATUS OF IRRADIATION EXPERIMENTS

Irradiation experiments are presently being conducted in the ORR and HFIR, which are mixed-spectrum fission reactors, and in the EBR-II, which is a fast-spectrum reactor. Experiments are generally cooperative between several program participants. Experiment plans, tests matrices, etc. are reviewed by the Alloy Development for Irradiation Performance Task Group.

7.1 STATUS OF ORR-MFE-2 — J. W. Woods, E. E. Bloom, A. F. Zulliger (ORNL), and L. R. Greenwood (ANL)

7.1.1 ADIP Task

This experiment supports those tasks of the ADIP Program Plan that require neutron irradiations to accomplish their objectives. The experiment contains alloys from each alloy development path.

7.1.2 Objective

The ORR-MFE-2 irradiation experiment is a vehicle for irradiation of samples for postirradiation testing and examination (e.g., tensile, creep-rupture, and fatigue testing; measurement of irradiation creep; and microstructural examination). The objectives of these experiments from the viewpoint of alloy development are to examine:

1. effects of composition on the tensile properties of stainless steels with nominal compositions near that of type 316 stainless steel;
2. effects of preirradiation heat treatment on the tensile properties of type 316 stainless steel;
3. effects of irradiation on the tensile properties of type 316 and 16-8-2 stainless steel welds;
4. effects of irradiation on the tensile properties of representative path B alloys;
5. effects of irradiation on the tensile, creep-rupture, and fatigue properties and on the microstructures of representative titanium alloys, vanadium alloys, and niobium alloys;
6. irradiation creep of type 316 stainless steel and Nimonic PE-16, path A and B alloys, respectively;
7. postirradiation fatigue properties of type 316 stainless steel, Nimonic PE-16, and high-nickel alloys X-750 and Inconel 600;
8. effects of irradiation on tensile and creep-rupture properties of alloys with long-range order (path D).

7.1.3 Summary

Redesign of ORR-MFE-2 to obtain more efficient heat removal has been completed. The experiment is being assembled and reactor insertion is projected to be about July 24. The flux and spectral mapping experiment is assembled and will be irradiated shortly before insertion of ORR-MFE-2.

7.1.4 Progress and Status

7.1.4.1 Introduction

It is desirable to maximize the amount of fuel around an experiment to increase the fast-neutron flux and thus the displacement production rate. The first experiment, ORR-MFE-1, in support of fusion reactor materials development conducted in the ORR, was placed in position C-7 and had fuel elements on four sides. Temperatures in this experiment exceeded the desired control temperatures in many positions. The core configuration was changed and some control temperatures were raised for operation of the experiment. The results of ORR-MFE-1 showed that the lower irradiation temperatures desired for ORR-MFE-2 could not be obtained unless the number of samples was drastically reduced. It was decided to redesign ORR-MFE-2 to obtain more efficient heat removal, thus permitting the required number of samples.

7.1.4.2 Status of ORR–MFE–2

Redesign of the experiment for the E-7 position of the ORR is completed, and assembly is in progress. A quarter axial section of the overall layout of the experiment is shown in Fig. 7.1.1. The space inside the experiment can has been divided into two sections. The top two-thirds of the can will be occupied by the upper holder assembly and contain four gas-gap capsules in each of the levels 1 through 4. The lower holder assembly, containing four capsules in level 5, will occupy the bottom one-third of the experiment can volume. Figure 7.1.2 shows the holder assembly before the capsules were positioned.

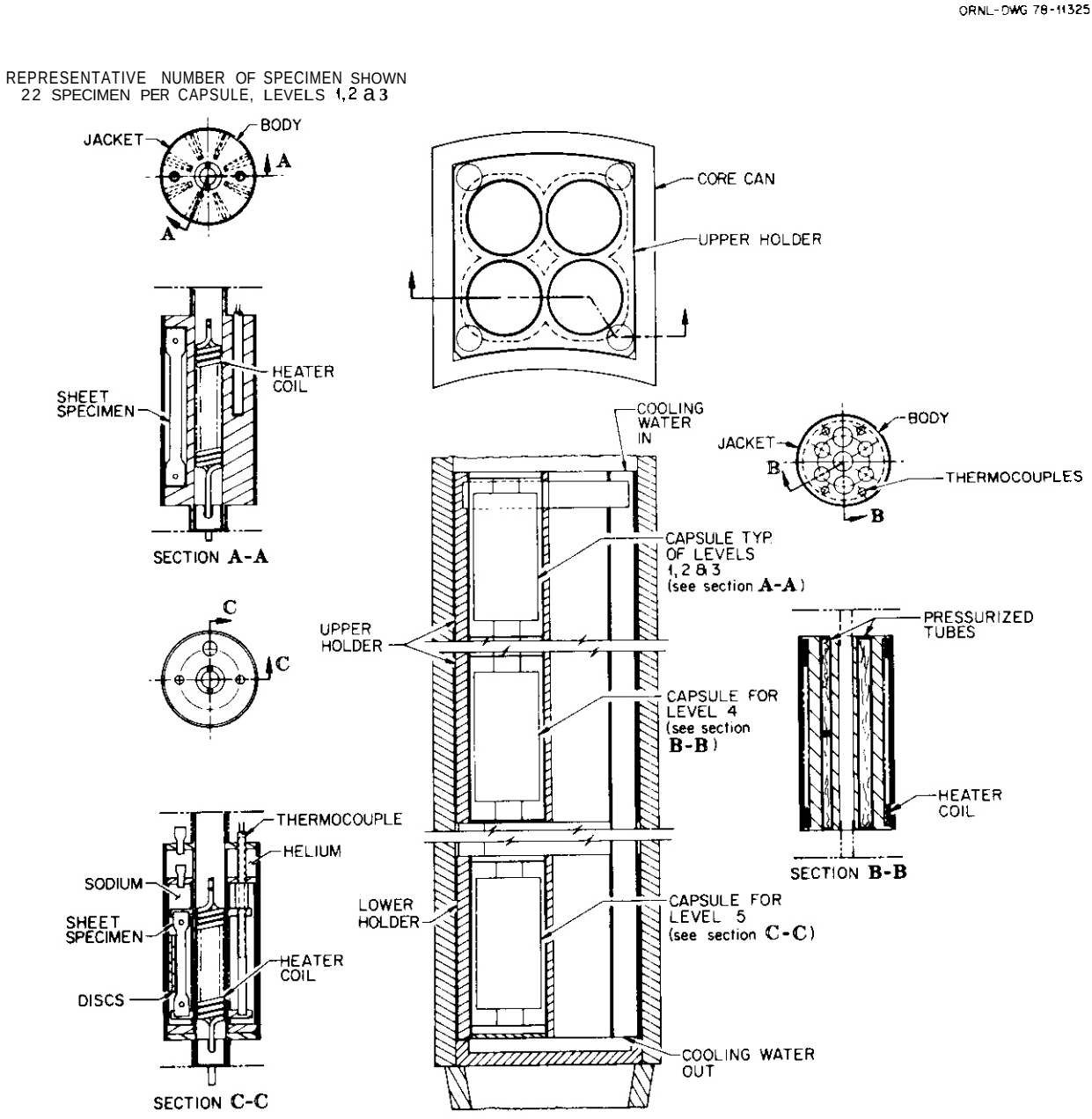

Fig. 7.1.1. ORR-MFE-2 Irradiation Experiment.

Y-154836

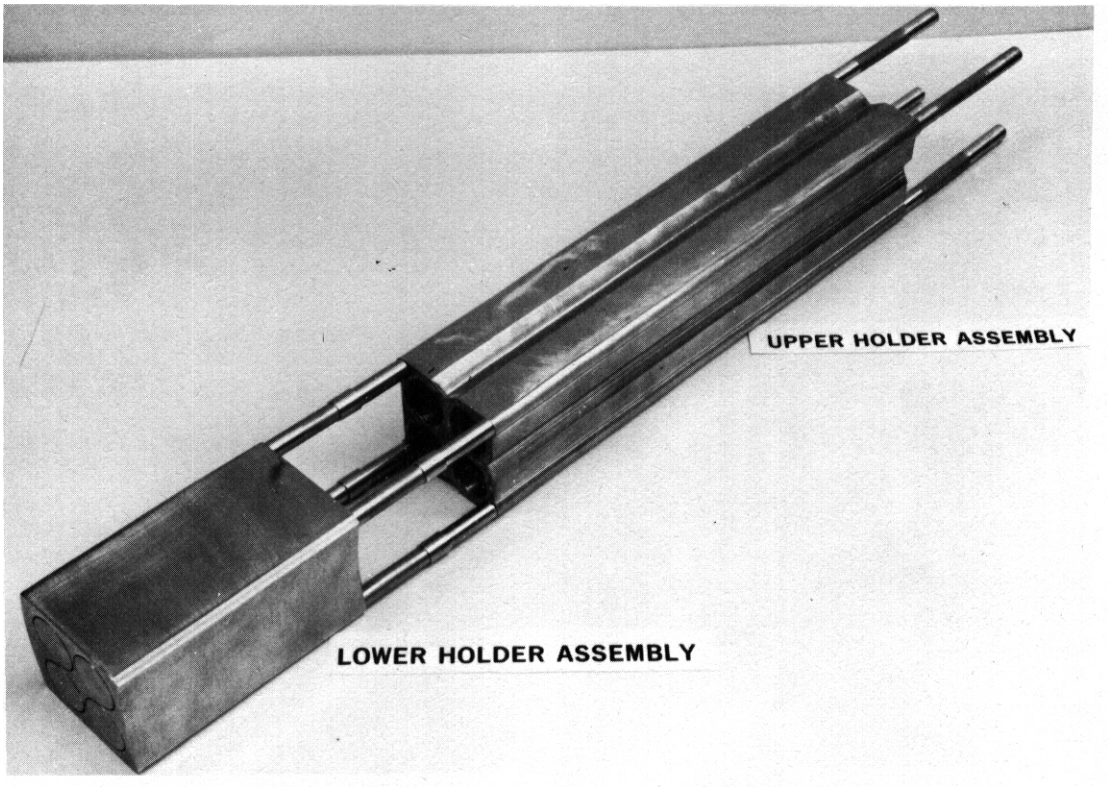

Fig. 7.1.2. Upper and Lower Holder Assembly for ORR-MFE-2 Irradiatios Experiment.

Capsules in levels 1, 2, and 3 will have a segmented 6061-T6 aluminum body. Between adjacent segments 22 sheet specimens are fitted and the assembly is held in place by a jacket of either 6061-T6 aluminum or type *430* stainless steel. Centering disks with integral hubs of type *430* stainless steel will be pinned to capsule end extensions to provide a uniform gas annulus around the capsules and to minimize axial heat flow. The thickness of the helium annulus and of the centering fins has been determined for each capsule so that its specimens will be irradiated at the desired temperature. Sufficient electric heat is provided to control each capsule's temperature (a heater coil is located in the center hole of each capsule). Figure 7.1.3 shows the components of a typical capsule in levels 1 through 3.

Capsules in level 4 are similar to the above capsules except that each will contain 12 pressurized tube specimens. The body of each capsule is 6061-T6 aluminum with holes drilled in it to accommodate the

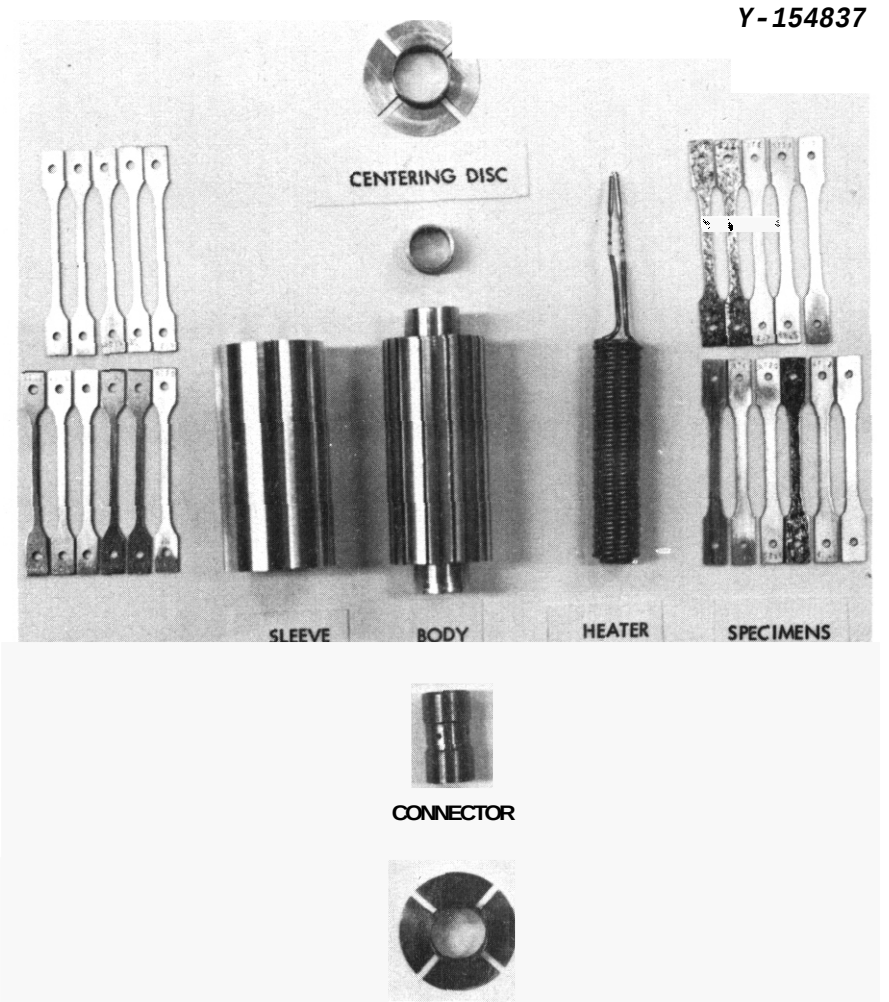

Fig. 7.1.3. Components of Typical Capsule from Levels 1 through 3.

specimens and thermocouples. The specimen holes are sized to provide a 10% diametral and 5% axial change in the pressurized tubes. The heater coil will be wound directly on the outside of the body and held in place with a jacket of either aluminum or stainless steel. Figure 7.1.4 shows the components of a level 4 capsule.

Figure 7.1.5 shows the arrangement of a stack of four capsules in each sleeve of the upper holder, along with the desired operating temperature per stack and position of the stacks in the experiment can. The capsules in a stack will be connected by a coupling pinned to capsule end extensions.

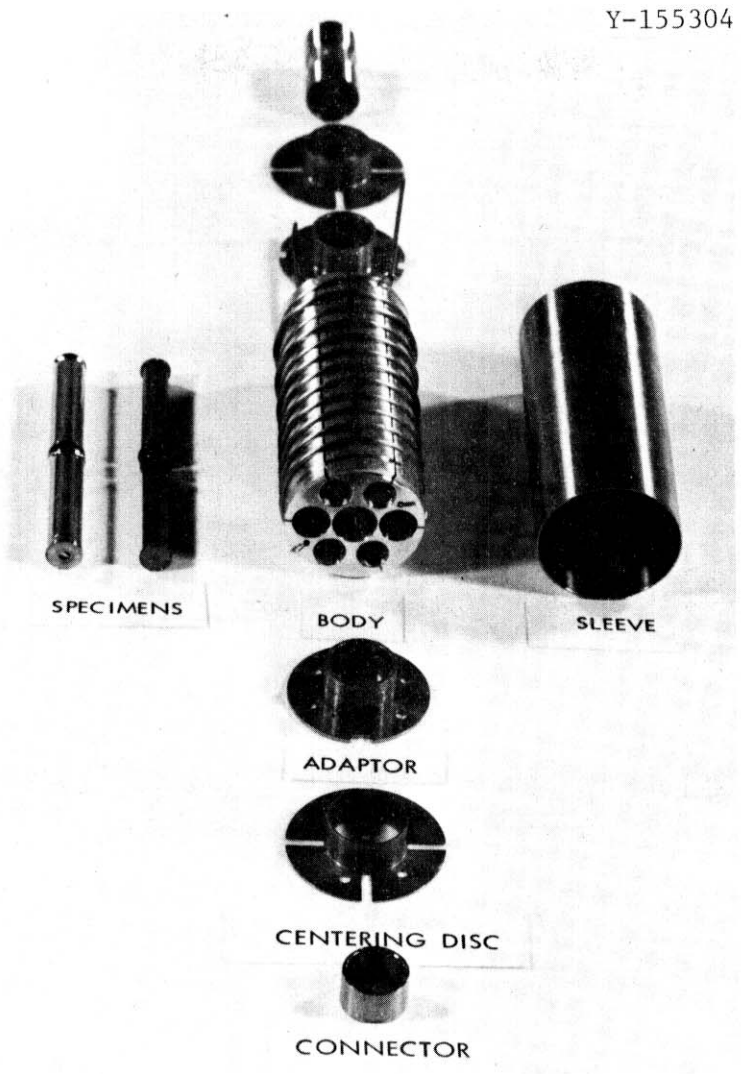

Fig. 7.1.4. Components of Pressurized Tube Specimen Capsule.

The lower holder assembly is similar to the upper holder assembly and will contain four sodium-filled gas-gap capsules (level 5) positioned inside water-cooled sleeves. The sodium will be doubly contained: a type 304L stainless steel capsule for the outer container and a type 321 stainless steel container for the inner capsule. The inner container will be filled with sodium to a 50-mm height, submerging a complement of 44 sheet specimens and numerous thin disk specimens. A helium plenum above the sodium level is provided to allow for sodium expansion. The capsule components are shown in Fig. 7.1.6.

ORNL-DWG 78-9151

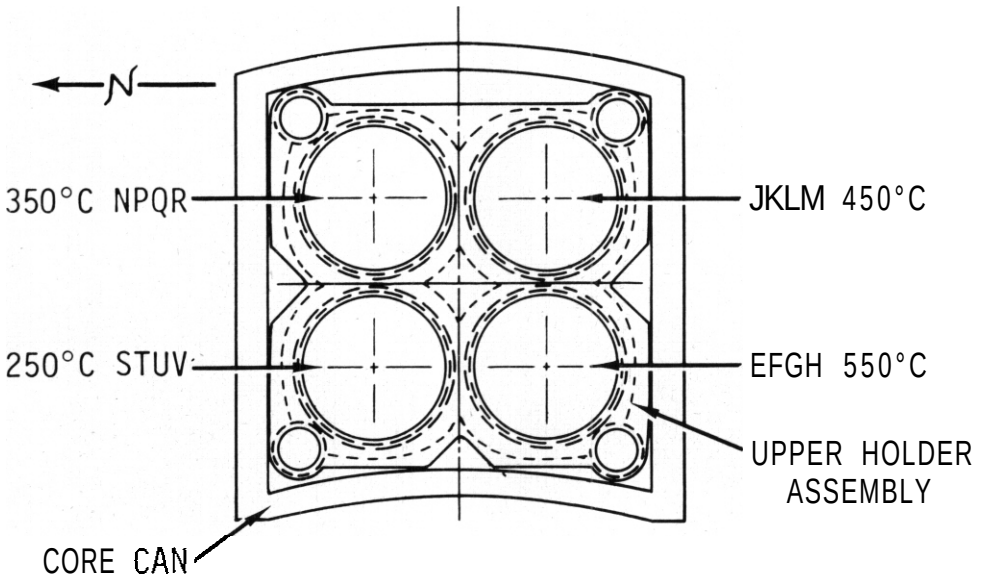

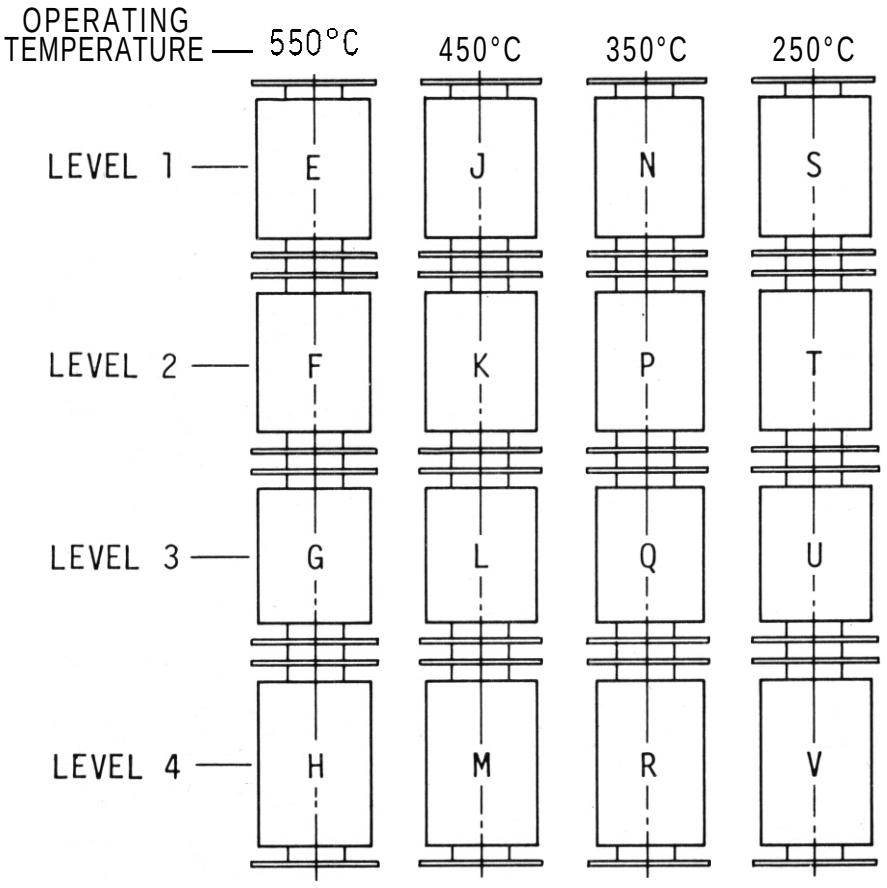

Fig. 7.1.5. Capsule Arrangement for Levels 1 through *4.*

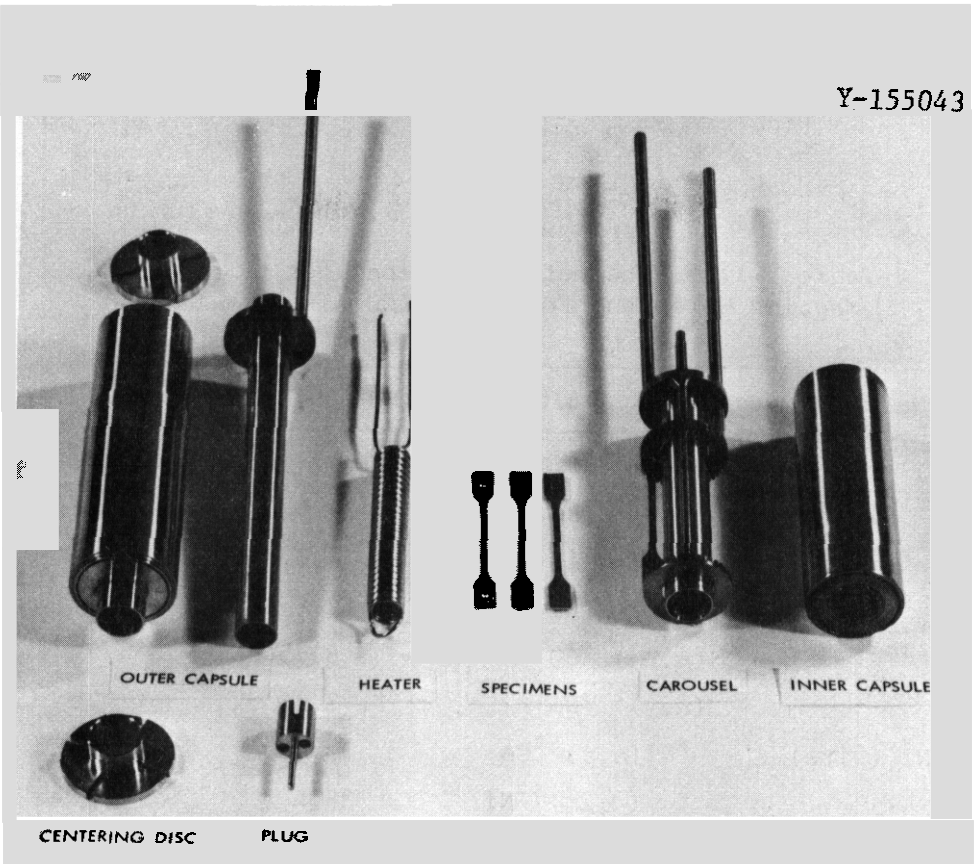

Fig. 7.1.6. Sodium-Filled Capsule Components.

7.1.4.3 Neutron Dosimetry

The Dosimetry Center at ANL has planned the dosimetry for the ORR-MFE experiments. Before the insertion of ORR-MFE-2, a short irradiation (24 h at a reactor power level of 3 MW) for spectral mapping will be conducted. Dosimetry reactions that are to be used for this run are listed in Table 7.1.1. Bare and cadmium-covered dosimeter foils are placed near each other at five locations along each quadrant of the assembly. This spectral mapping experiment is assembled and awaiting insertion.

7.1.5 Conclusions

Redesign of ORR-MFE-2 has been completed. Twenty gas-gap capsules positioned in a holder assembly will allow testing of 432 sheet tensile specimens and 48 pressurized tubes. Assembly of the experiment is in progress and insertion in the reactor is projected to be about July 24.

Table 7.1.1. Dosimetry Reactions for ORR Spectral Mapping Wires and Foils in 1100 Aluminum Capsule

Material	Reaction	Half-Life	Cd Cover
^{237}Np, ^{235}U, ^{238}U	$(n,f)^{95}Zr$	64.1 d	Yes
	$(n,f)^{103}Ru$	39.4 d	Yes
	$(n,f)^{131}I$	8.0 d	
	$(n,f)^{140}Ba$	12.8 d	
^{238}U	$(n,2n)^{237}U$	6.75 d	
	$(n,\gamma)^{239}Np$	2.36 d	Yes
Ni (wire)	$^{58}Ni(n,p)^{58}Co$	70.85 d	
	$(n,2n)^{57}Ni$	36 h	
Co (wire)	$^{59}Co(n,\gamma)^{60}Co$	5.27 y	Yes
	$(n,p)^{59}Fe$	44.6 d	
	$(n,2n)^{58}Co$	70.85 d	
Fe (wire)	$^{54}Fe(n,p)^{54}Mn$	312.5 d	
	$(n,\alpha)^{51}Cr$	27.1 d	
	$Fe(n,\gamma)^{59}Fe$	44.6 d	
Au	$^{197}Au(n,\gamma)^{198}Au$	2.7 d	Yes
	$(n,2n)^{196}Au$	6.1 d	
Ti	$^{46}Ti(n,p)^{46}Sc$	83.9 d	
	$^{47}Ti(n,p)^{47}Sc$	3.4 d	
	$^{48}Ti(n,p)^{48}Sc$	1.8 d	
Sc	$^{45}SC(n,\gamma)^{46}Sc$	83.9 d	Yes
	$(n,2n)^{44m}Sc$	2.44 d	

7 2 IRRADIATION EXPERIMENT SCHEDULE

Experiment Designation	Major Objective
A. Oak Ridge Research Reactor	
ORR-MFE-1 / ORR-MFE-2	Experiments to scope the effects of composition and microstructure on the tensile, fatigue, and irradiation creep of representative path A, B, and C alloys.
ORR-MFE-3	Effects of irradiation on postirradiation fatigue crack growth in representative path A, B, and C alloys.
ORR-MFE-4	Effect of irradiation on tensile, fatigue, and irradiation creep of path A PCA (Prime Candidate Alloy) and path B base research alloys. Spectral tailoring to maintain correct He/dpa ratio. Irradiation on continuing basis.

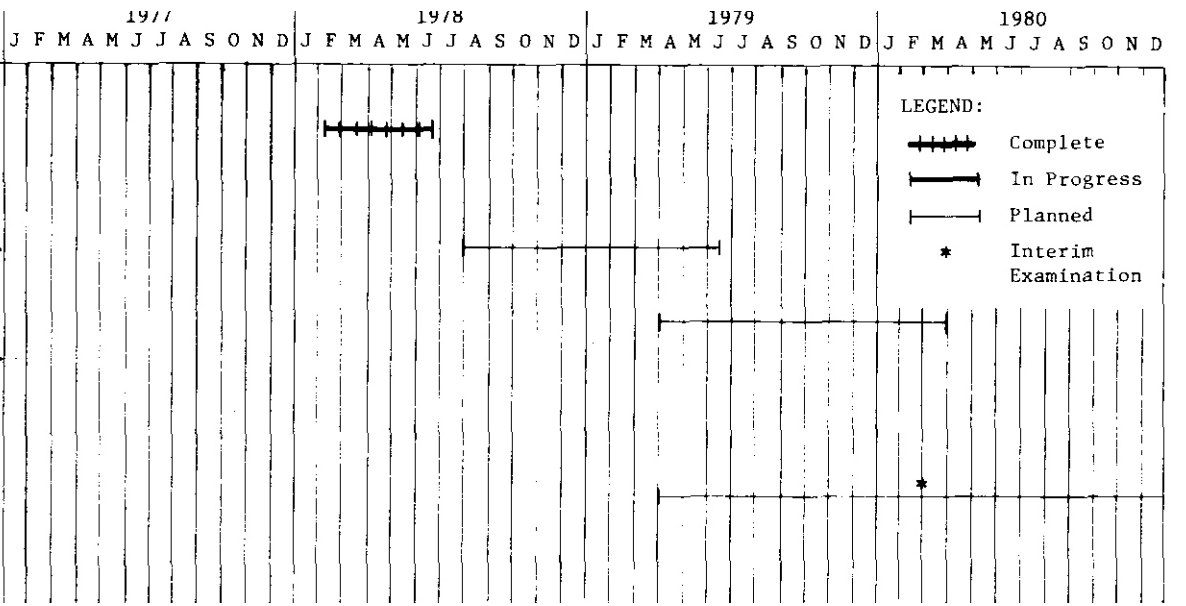

Experiment Designation	Major Objective
ORR-MFE-5	In-reactor fatigue crack growth experiment
B. Experimental Breeder Reactor II	
Subassembly X 264	Effect of preinjected helium (2–200 at. ppm) on microstructure and tensile properties of 316 SS, PE-16, V and Nb alloys. Fluence $\leq 2.3 \times 10^{26}$ n/m^2, 500–825°C.
Subassembly X 287	Effect of preinjected helium (2–200 at. ppm He) on microstructure and tensile properties of 316 SS, PE-16, V and Nb alloys. Fluence $\leq 4 \times 10^{26}$ n/m^2, 400–700°C.
Subassembly X 217D	Stress relaxation Ti Alloys
Planned, Subassembly Designation not available	Effect of irradiation on swelling, tensile, fatigue, and crack growth properties of Ti scoping alloys. 370, 450, and 550°C, position in reactor not finalized, therefore no fluence estimate

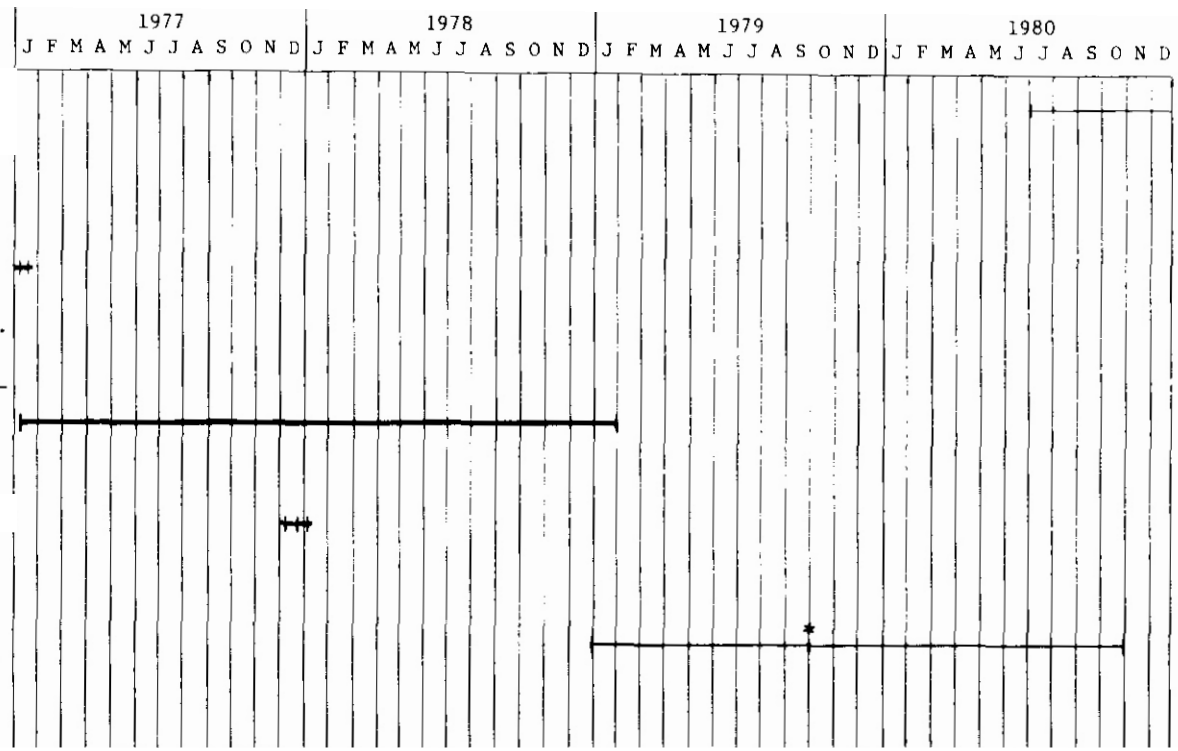

Experiment Designation	Major Objective
Not available	Effect of Irradiation on swelling, tensile, fatigue, and crack growth properties of V and Nb scoping alloys. 370, 450, 550, and 650°C. Position in reactor not finalized, therefore no fluence estimate.
C. High Flux Isotope Reactor (HFIR)	
HFIR-CTR-4	PE-16 for swelling and tensile properties, 300—700°C 2.2—4.5 dpa, 100—350 at. ppm He
HFIR-CTR-7	PE-16 for swelling and tensile properties, 300—700°C 9—18 dpa, 1250—3000 at. ppm He
HFIR-CTR-8	duplicate of -7
HFIR-CTR-9	316 and 316 + Ti for swelling and tensile properties, 280—680°C, 9—18 dpa, 400—1000 at. ppm He

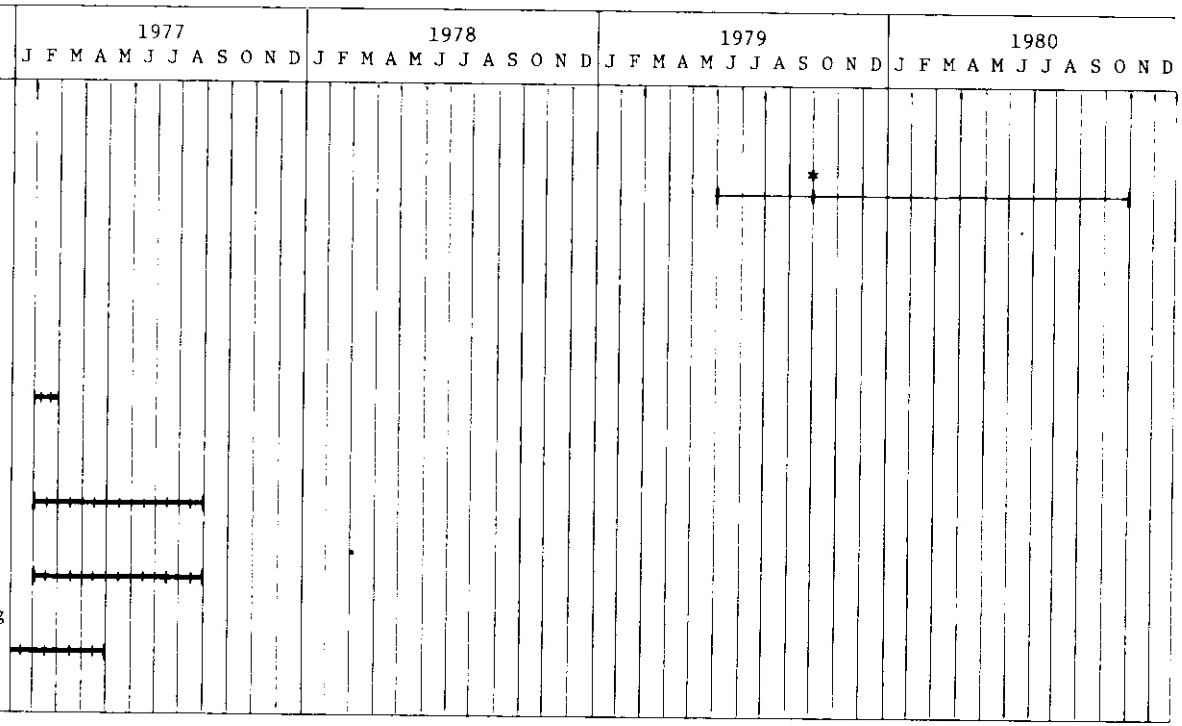

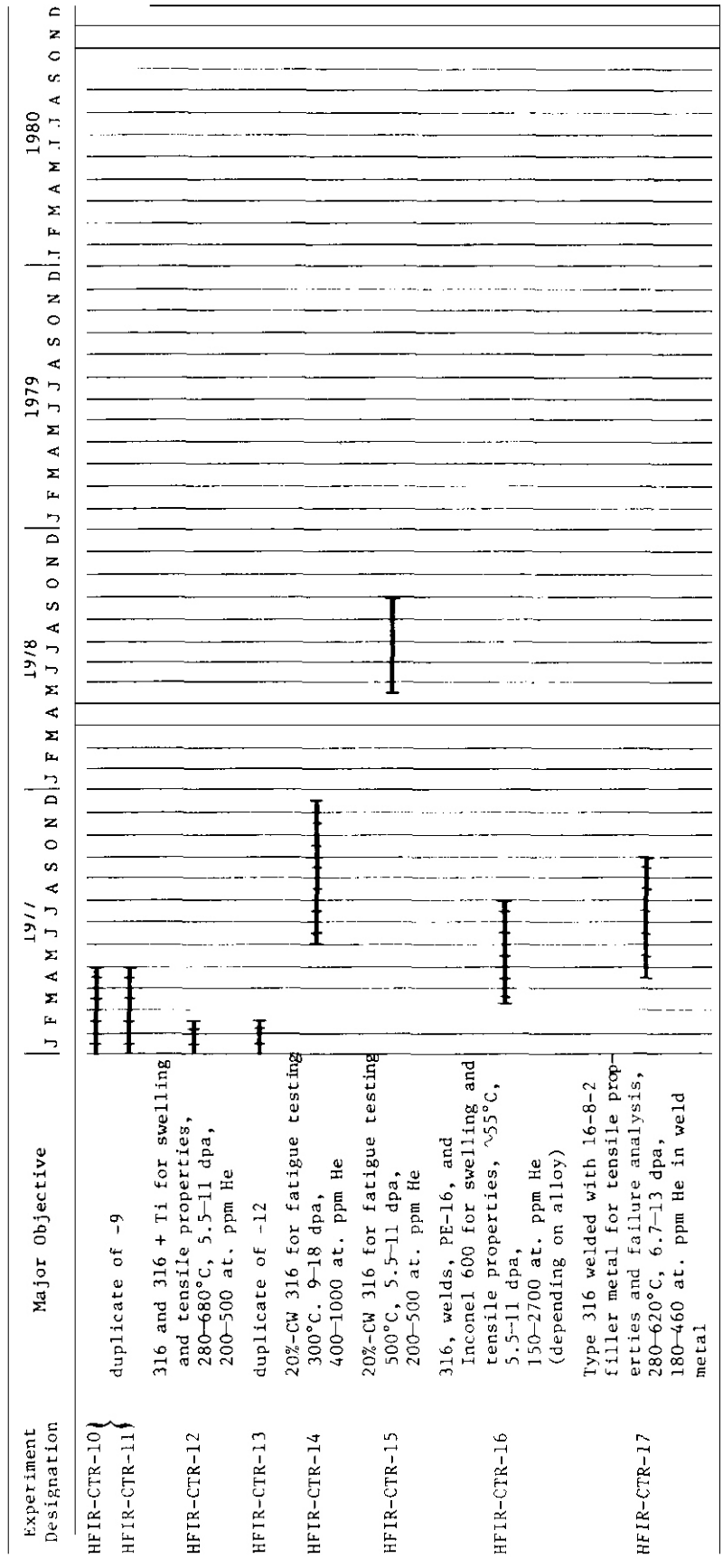
Experiment Designation
Major Objective
1977
1978
1979
1980
J F M A M J J A S O N D J F M A M J J A S O N D J F M A M J J A S O N D J F M A M J J A S O N D
HFIR-CTR-10
HFIR-CTR-11
duplicate of -9
316 and 316 + Ti for swelling and tensile properties, 280–680°C, 5.5–11 dpa, 200–500 at. ppm He
HFIR-CTR-12
HFIR-CTR-13
duplicate of -12
20%-CW 316 for fatigue testing 300°C. 9–18 dpa, 400–1000 at. ppm He
HFIR-CTR-14
20%-CW 316 for fatigue testing 500°C, 5.5–11 dpa, 200–500 at. ppm He
HFIR-CTR-15
316, welds, PE-16, and Inconel 600 for swelling and tensile properties, ~55°C, 5.5–11 dpa, 150–2700 at. ppm He (depending on alloy)
HFIR-CTR-16
Type 316 welded with 16-8-2 filler metal for tensile properties and failure analysis, 280–620°C, 6.7–13 dpa, 180–460 at. ppm He in weld metal
HFIR-CTR-17

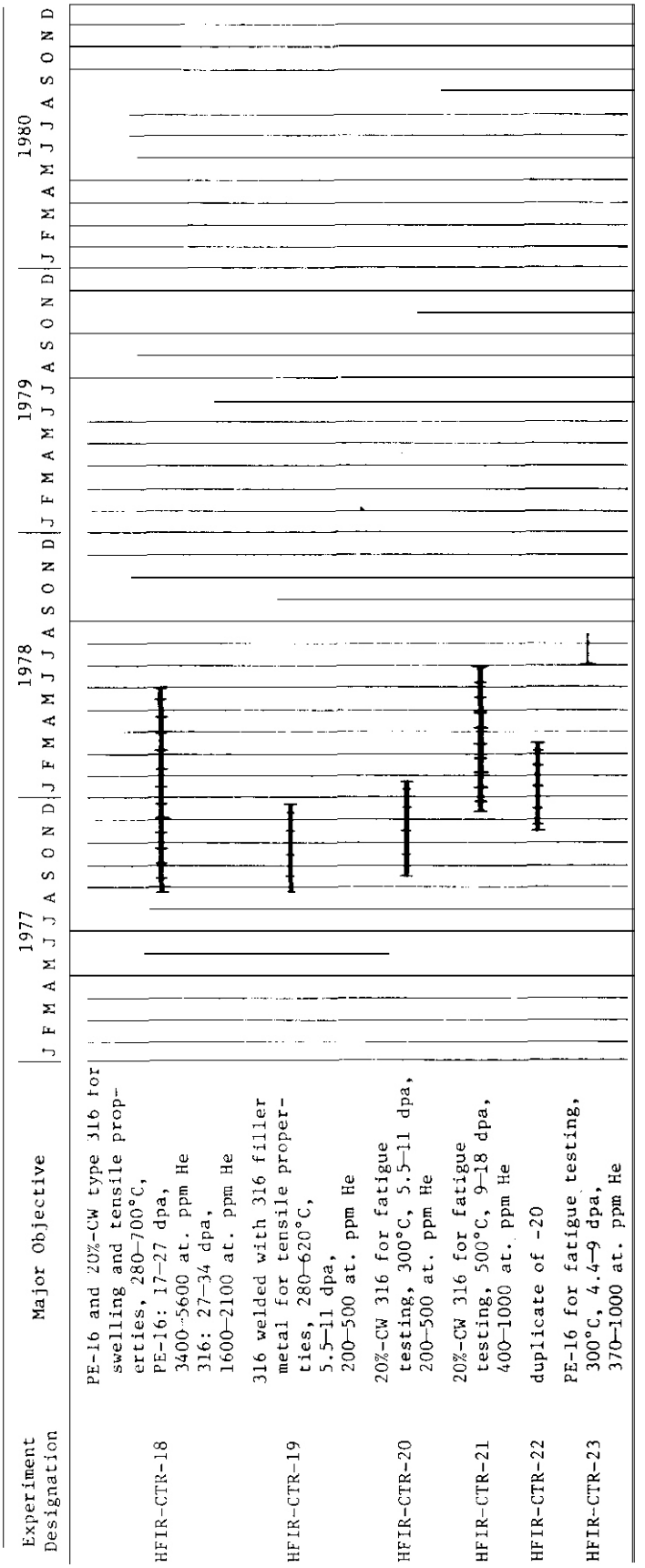
Experiment Designation
Major Objective
1977
1978
1979
1980
J F M A M J J A S O N D J F M A M J J A S O N D J F M A M J J A S O N D J F M A M J J A S O N D
HFIR-CTR-18
PE-16 and 20%-CW type 316 for swelling and tensile properties, 280–700°C,
PE-16: 17–27 dpa, 3400–5600 at. ppm He
316: 27–34 dpa, 1600–2100 at. ppm He
HFIR-CTR-19
316 welded with 316 filler metal for tensile properties, 280–620°C, 5.5–11 dpa, 200–500 at. ppm He
HFIR-CTR-20
20%-CW 316 for fatigue testing, 300°C, 5.5–11 dpa, 200–500 at. ppm He
HFIR-CTR-21
20%-CW 316 for fatigue testing, 500°C, 9–18 dpa, 400–1000 at. ppm He
HFIR-CTR-22
duplicate of -20
HFIR-CTR-23
PE-16 for fatigue testing, 300°C, 4.4–9 dpa, 370–1000 at. ppm He

Experiment Designation	Major Objective	1977 J F M A M J J A S O N D	1978 J F M A M J J A S O N D	1979 J F M A M J J A S O N D	1980 J F M A M J J A S O N D
(2 future expts.)	Path A PCA for phase stability, swelling, tensile properties, 280–620°C, 10 dpa, 570 at. ppm He (max)				
(2 future expts.)	Path A PCA for phase stability, swelling, tensile properties, 280–620°C, 34 dpa, 2400 at. ppm He (max)				
(4 future expts.)	Path B base research alloys various conditions				
(4 to 6 future expts.)	Path C Ti alloys, various conditions				

8. CORROSION TESTING AND HYDROGEN PERMEATION STUDIES

Corrosion, erosion, and mass transfer are processes that may degrade mechanical properties, alter heat transfer characteristics of heat transport systems, and present maintenance problems when radioactive nuclides are involved. The importance of hydrogen permeation and the behavior of hydrogen in the alloy systems under development is clear from consideration of tritium inventory, containment, etc. In the early stages of the development program, base-line information is required to define compatible or noncompatible alloy systems and coolants. As optimized alloys are developed, more detailed data on effects of adjustments in alloy composition or structure may be required. Extensive engineering compatibility data will be required on the final optimized alloys.

8.1 CAPSULE TESTS OF IRON–BASE ALLOYS IN LITHIUM — P. F. Tortorelli and J. H. DeVan (ORNL)

8.1.1 ADIP Task

ADIP Task 1.A.3, Perform Chemical and Metallurgical Compatibility Analyses.

8.1.2 Objective

The purpose of this program is to determine the chemical compatibility of iron-base alloys with metallic lithium. Structural steel specimens are exposed to static lithium containing selected solute additions to identify the kinetics and mechanisms that govern the corrosion of steels by lithium. Specific program objectives are (1) to determine the effects of N, C, H, and O on apparent solubilities of stainless steel components in lithium; (2) to determine the C and N partitioning coefficients between stainless steels and lithium; (3) to determine the effects of soluble (Ca, Al) and solid (Y, Zr, Ti) active metal additions on corrosion of stainless steels by lithium; and (4) to determine the tendencies for dissimilar-metal mass transfer between stainless steel and Mo, Nb, and Co.

8.1.3 Summary

Data are reported on the compatibility at 500 to 700°C between type 316 stainless steel and liquid lithium that contained either O, C, H, Al, Ti, Zr, Si, or Pb additions. Additions of Al and Si resulted in continuous and potentially inhibiting reaction layers on the stainless steel surfaces. Additions of Pb, Zr, and Ti produced no significant effects compared with base-line tests. The presence of O or H in the liquid lithium had very little influence on the corrosion of type 316 stainless steel under static conditions. On the other hand, the addition of C altered the near-surface microstructure with corresponding weight gains. The comparative corrosion resistance of a variety of 300 series stainless steels was determined in purified lithium. Only small

differences in corrosion response occurred among the steels tested. Types 310 and 321 stainless steel exhibited the largest and smallest weight losses and surface degradations, respectively.

8.1.4 Progress and Status

Static capsules of the type described last quarter[1] are being used to study impurity-induced reactions of austenitic stainless steels in lithium. The tests are conducted in the temperature range 500 to 700°C for 1000 to 10,000 h. A sheet specimen is contained in each capsule and is weighed before and after test.

The capsule test matrix is shown in Table 8.1.1 and included additions of 2-5 wt % Al and about 9.5 wt % Si, which are relatively soluble in lithium and can potentially form intermetallic compounds with the principal elements of austenitic stainless steels. Aluminum prevented weight loss of type 316 stainless steel in lithium, as shown in Fig. 8.1.1. The sheet insert gained weight at all test temperatures (500, 600, and 700°C), while after-test analyses showed that the lithium had been depleted of aluminum. (For example, at 700°C, a 5000-h test reduced the aluminum concentration in the lithium from 2.3 to 0.2 wt %.) Silicon additions to the lithium resulted in similar behavior (*see* Fig. 8.1.2). On the other hand, insoluble (interstitial-gettering) additives such as Ti and Zr, added to the capsules as small sheet specimens, did not cause significant weight or metallographic changes (see Table 8.1.1 and Fig. 8.1.3). Lead was also investigated as an addition to lithium because of its neutron-multiplying ability. An addition of about 50 wt % Pb did not significantly change the corrosion of type 316 stainless steel from its behavior in purified lithium.

The effect of interstitial impurities in lithium on the corrosion of type 316 stainless steel was studied using additions of Li_2O, LiH, and C. The addition of 0.05 wt % O and 0.87 wt % H in the liquid lithium did not promote corrosion (*see* the weight changes in Table 8.1.1). The microstructures of the near-surface regions of specimens tested in Li + Li_2O and Li + LiH showed not alteration. This is in contrast to another investigation,[2] which reported metallographic

Table 8.1.1. Effects of Additives to Lithium on the Corrosion of Type 316 Stainless Steel

Additive (wt %)	Test Temperature (°C)	Test Time (h)	Weight Change (g/m^2)	Metallographic Results
Al-2.3	500	500	+0.8	no attack
Al-2.3	500	2000	+1.2	no attack
Al-2.4	500	5000	+1.6	2 μm reaction layer
Al-2.3	600	500	+5.1	6 μm reaction layer
Al-2.4	600	2000	+3.8	6 μm reaction layer
Al-2.2	600	5000	+7.3	10 μm reaction layer
Al-2.3	700	500	+9.3	14 μm reaction layer
Al-2.3	700	2000	+11.4	34 μm reaction layer
Al-2.3	700	5000	+13.2	42 μm reaction layer
Al-5.0	500	2000	+1.1	no attack
Al-4.8	600	2000	+6.5	reaction layer
Al-4.9	700	2000	+19.3	reaction layer
Si-9.8	500	2000	+68.4	80 μm reaction layer
Si-9.4	600	2000	+52.2	160 μm reaction layer
Si-9.3	700	2000	+34.8	150 μm reaction layer
Ti-4.9	500	2000	+0.1	no attack
Ti-5.0	600	2000	+0.6	no attack
Ti-5.0	700	2000	−0.7	no attack
Zr-5.1	500	2000	+0.6	no attack
Zr-5.4	600	2000	0.0	no attack
Zr-5.3	700	2000	−0.7	no attack
Ph-49.5	500	2000	+0.7	no attack
Pb-50.2	500	5000	+1.4	slight reaction
Ph-48.8	600	2000	+1.1	no attack
Pb-48.4	600	5000	0.0	slight attack
Pb-49.6	700	2000	−1.8	slight attack
Pb-47.6	700	5000	−4.1	slight attack
c-0.9	500	2000	+0.5	slight attack
c-0.9	600	2000	+4.4	dense ppt. to depth of 70 um
C-0.8	700	2000	+8.0	very dense ppt. to depth of 85 um
Li_2O-0.1	500	2000	+0.3	very small reaction layer
Li_2O-0.1	600	2000	0.0	particles on surface
Li_2O-0.1	700	2000	+0.4	particle on surface
LiH-6.6	500	2000	0.0	no attack
LiH-6.4	600	1000	+0.3	very slight grain boundary attack
LiH-6.9	600	2000	+0.6	no attack
LiH-6.9	700	1000	−0.4	no attack
LiH-6.8	700	2000	−0.1	no attack

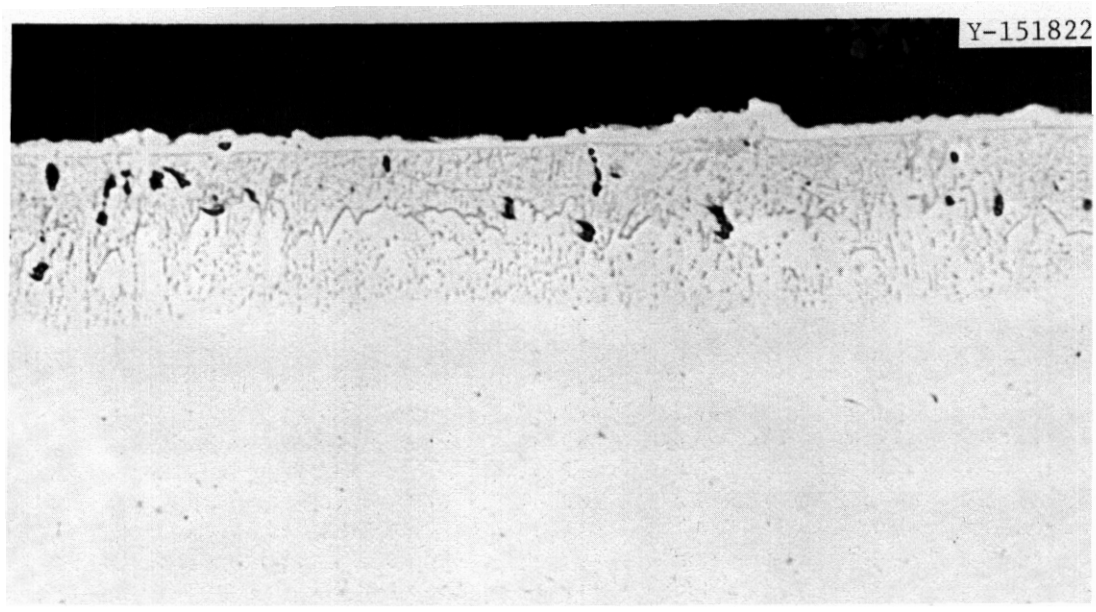

Fig. 8.1.1. Type 316 Stainless Steel Exposed to Li–2.3 wt % Al for 5000 h at 700°C. 500×.

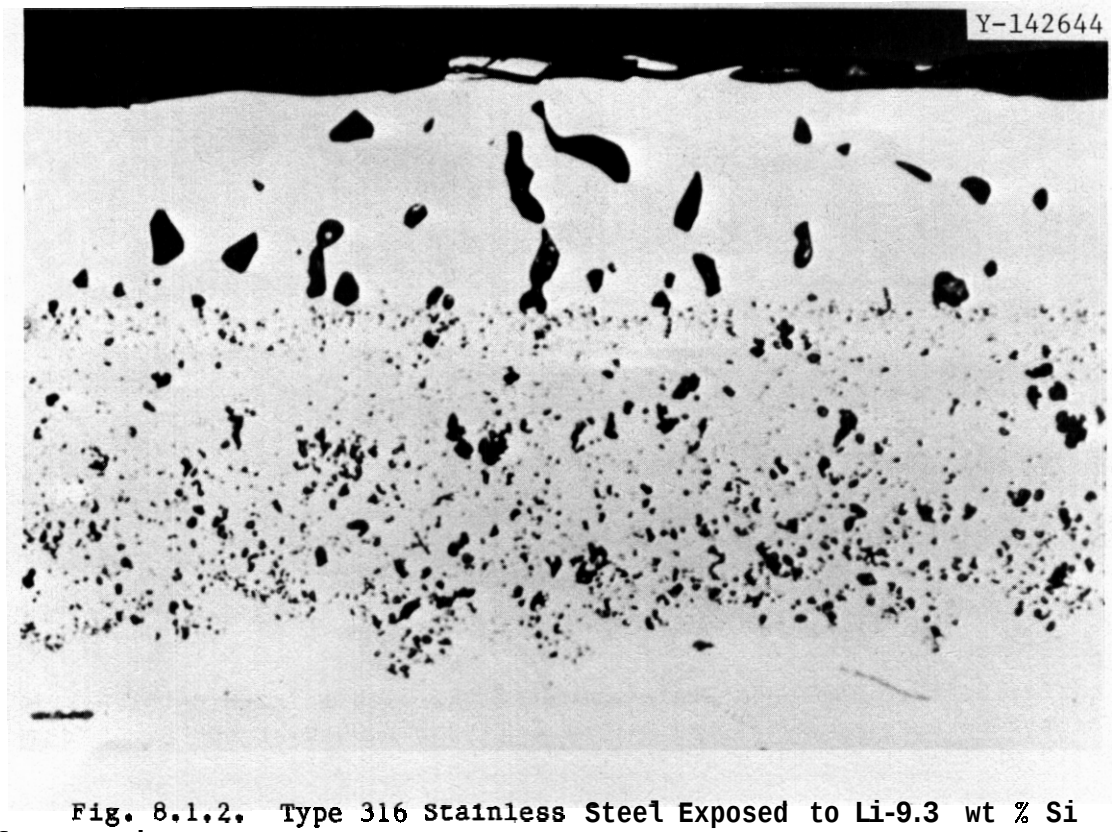

Fig. 8.1.2. Type 316 Stainless Steel Exposed to Li-9.3 wt % Si for 2000 h at 700°C. 500×.

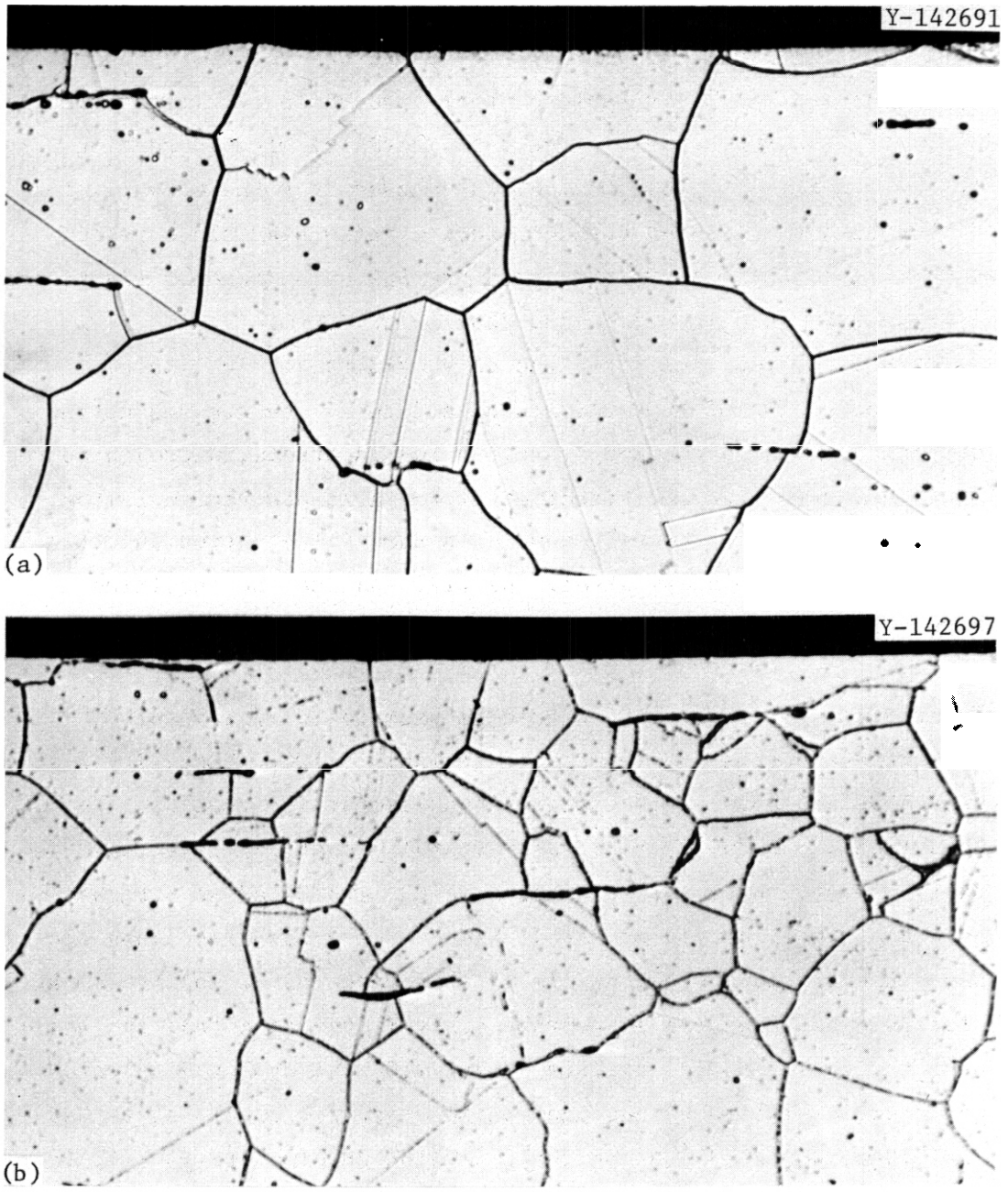

Fig. 8.1.3. Type 316 Stainless Steel Exposed to Lithium with Insoluble Getters. 500×. (a) 5.0 wt % Ti for 2000 h at 600°C. (b) 5.3 wt % Zr for 2000 h at 700°C.

changes in the near-surface layers when hydrogen was added to lithium. The discrepancy is not readily explainable at this time but may be due to differences in experimental techniques. However, the negligible weight changes measured by Coen et al.[2] in association with hydrogen additions are in general agreement with the present results.

Specimens of type 316 stainless steel exposed in static capsules to Li—0.9 wt % C showed weight gains that increased with increasing temperature. Metallographic examinations showed that the weight gains were accompanied by enhanced carbide precipitation near the exposed surfaces. Figure 8.1.4 shows that such precipitation becomes significant at 600°C and increases in extent and density at 700°C.

As previously reported,[1] the presence of nitrogen in lithium accelerates corrosion of type 316 stainless steel. We are conducting a more extensive characterization of this alloy in static, nitrogen-containing lithium in order to find the effect of nitrogen concentration in the lithium and to evaluate the differences in the Li + N corrosion between types 316 and 316L stainless steel. We will analyze the resulting microstructures by Auger electron spectroscopy and scanning electron microscopy.

The results of comparative static lithium tests of several 300 series stainless steels are summarized in Table 8.1.2. The weight changes at 500 and 600°C were insignificant except for type 310 stainless steel. At 700°C, a microstructurally distinct layer was present on type 316L, while the type 310 specimen exhibited an attacked surface and a higher corrosion rate. Figure 8.1.5 compares types 310, 316, and 316L stainless steel specimens that were tested in lithium at 700°C for 5000 h. Electron microprobe analysis revealed that the near-surface layer shown in Fig. 8.1.5(a) (type 310) was depleted in chromium and nickel relative to the unperturbed matrix. On the other hand, the precipitate-depleted zone on the type 316L specimen [Fig. 8.1.5(c)] has approximately the same Cr/Fe and Ni/Fe ratios as the underlying matrix. It does contain, however, a greater amount of molybdenum. The small deposit on top of the reaction zone of type 316L was found to be

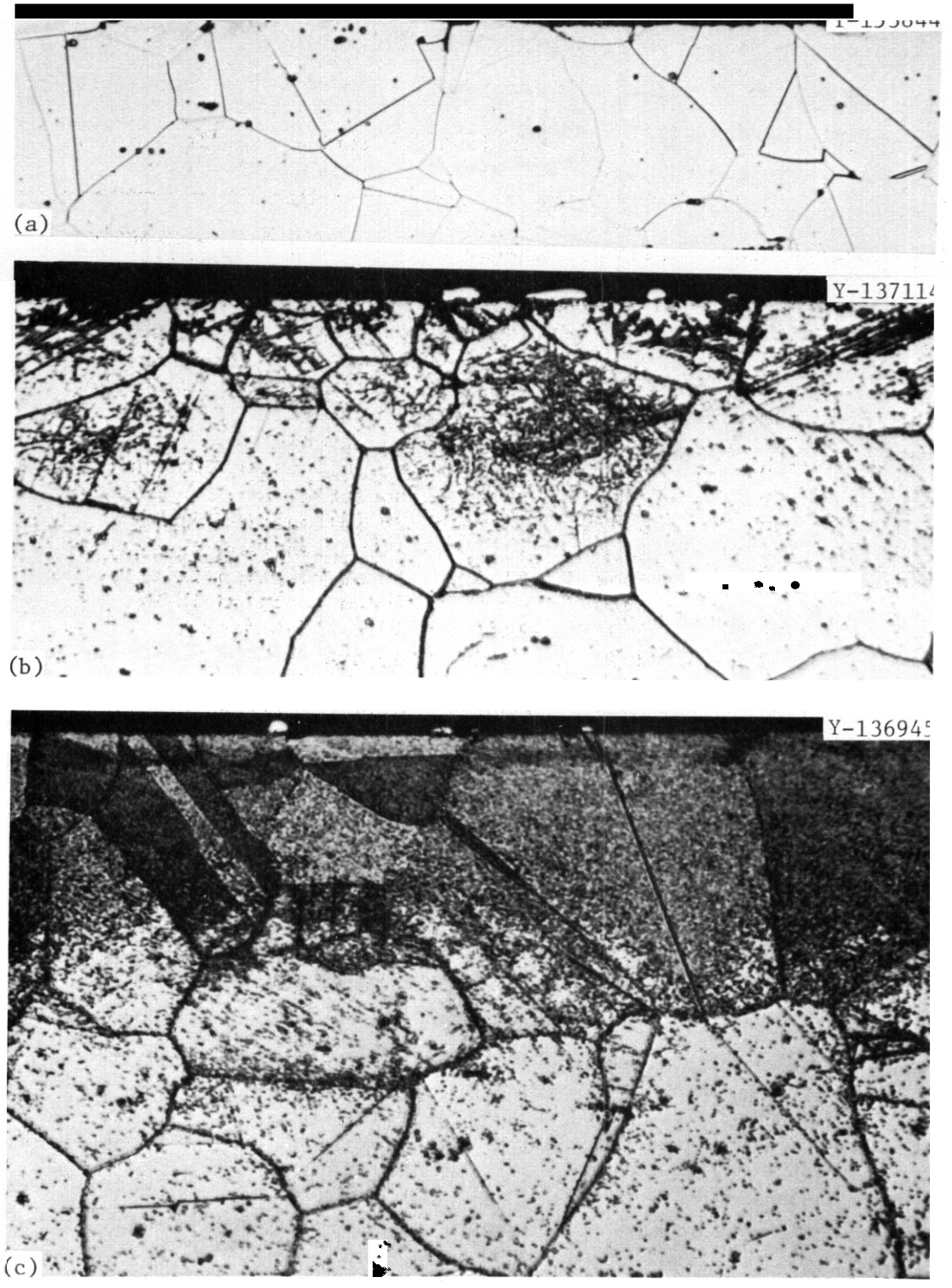

Fig. 8.1.4. Type 316 Stainless Steel Exposed to Li-0.9 wt % C for 2000 h at (a) 500, (b) 600, and (c) 700°C. 500×.

Table 8.1.2. Corrosion of Various 300 Series Stainless Steels

Alloy	Test Temperature (°C)	Test Time (h)	Weight Change (g/m^2)	Metallographic Results
304L	500	2000	+0.1	no attack
304L	500	5000	+0.3	no attack
304L	600	2000	+0.1	slight surface roughening
304L	600	5000	0.0	no attack
304L	700	2000	−0.8	no attack
304L	700	5000	−1.2	slight surface roughening
310	500	2000	+0.3	no attack
310	500	5000	+0.4	20 μm reaction layer
310	600	2000	+0.1	30 μm reaction layer
310	600	5000	−11.5	35 μm reaction layer
310	700	2000	−0.8	20 μm reaction layer
310	700	5000	−11.8	40 μm of attack
316	500	2000	0.0	no attack
316	500	5000	−0.2	
316	600	2000	−0.1	slight surface roughening
316	600	5000	0.0	no attack
316	700	2000	−0.4	very slight grain boundary attack
316	700	5000	−0.7	surface roughening
316L	500	2000	+1.0	20 μm reaction layer
316L	500	5000	+0.7	30 μm reaction layer
316L	600	2000	+1.5	slight roughening
316L	600	5000	+1.4	55 μm reaction layer
316L	700	2000	0.0	30 μm reaction layer
316L	700	5000	−0.8	40 μm reaction layer
321	500	2000	+0.1	slight attack
321	500	5000	+0.4	no attack
321	600	2000	+0.3	no attack
321	600	5000	0.0	no attack
321	700	2000	−0.8	no attack
321	700	5000	−0.3	no attack

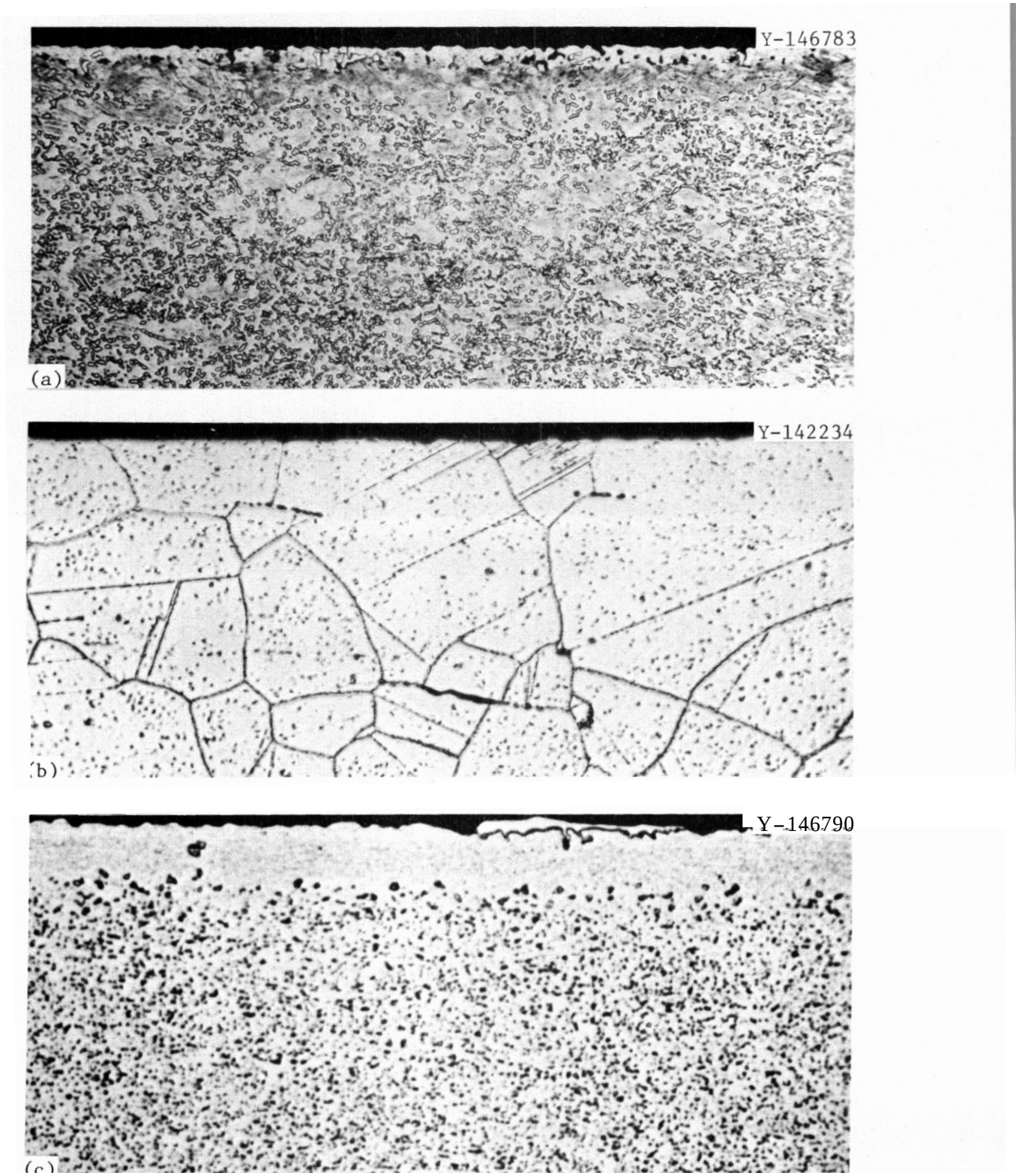

Fig. 8.1.5. **Stainless Steels Exposed to Lithium** for 5000 h **at 700°C. (a) Type 310,** 250×. (b) **Type 316,** 500×. (c) 316L, **250×.**

enriched in chromium and molybdenum relative to the base material. Types 304L and 321 were similar to type 316 in that they showed very little attack. Overall, type 321 was the most stable stainless steel with respect to corrosion by static liquid lithium.

8.1.5 Conclusions

1. Additions of Al, Si, and C to lithium result in reaction layers on the type 316 stainless steel and thus inhibit corrosion.

2. Oxygen and hydrogen additions to lithium do not adversely affect the corrosion of type 316 stainless steel.

3. Type 321 stainless steel had the best compatibility with pure lithium.

8.1.6 References

1. J. H. DeVan and J. R. DiStefano, "Capsule Tests of Iron-Base Alloys in Lithium," *ADP Quart.* ***Prog. Rep. March 31, 1978,*** DOE/ET-0058/1(78), pp. 190–99.

2. V. Coen et al., "Influence of Hydrogen on the Lithium Compatibility of A.I.S.I. 316 and 304 Type Stainless Steels," pp. 1501–05 in ***Proc. 7th*** *Symp. Engineering Problems in Fusion* ***Research*** (held at Knoxville, Tenn., Oct. 25–28, 1977), vol. II, Institute of Electrical and Electronic Engineers, New York, 1977.

8.2 THERMAL-CONVECTION LOOP TESTS OF STAINLESS STEEL IN LITHIUM — P. F. Tortorelli and J. H. DeVan (ORNL)

8.2.1 ADIP Task

ADIP Task I.A.3, Perform Chemical and Metallurgical Compatibility Analyses.

8.2.2 Objective

The purpose of this task is to evaluate the corrosion resistance of possible first-wall materials to flowing lithium in the presence of a temperature gradient. Corrosion rates (in terms of both dissolution and deposition) are measured as functions of time, temperature additions to the lithium, and flow conditions. These measurements are combined with chemical and metallographic examinations of specimen surfaces in order to establish the mechanisms and rate-controlling processes for dissolution and deposition reactions.

8.2.3 Summary

Corrosion results are reported for two types of thermal-convection loops that circulate liquid lithium. A type 316 stainless steel loop yielded weight change results similar to those from types 304L and 321 stainless steel loops, all of which operated for 3000 h at a maximum temperature of 600°C. Weight losses of type 316 stainless steel at 600°C were measured between 500 and 5000 h, and the rate of loss decreased with time. The operating status of the loops and future test plans are discussed.

8.2.4 Progress and Status

As described previously,[1] two types of thermal-convection loops (TCLs) are being used to evaluate the compatibility of austenitic stainless steels with lithium. The first type is in the form of a 0.46-m by 0.64-m parallelogram that contains interlocking tab specimens of the same material as the loop. The loop is operated without interruption for 3000 to 10,000 h and is then cut open to remove tab

specimens for analysis. (The procedure is described in more detail in the previous quarterly report,[1]) The second type of TCL is larger (0.48 m by 0.76 m) and is designed so that tab specimens can be withdrawn and inserted without altering the loop operating conditions.[1] In this way, corrosion rates can be monitored at selected time intervals for a given set of test specimens.

As discussed last quarter,[1] nine small TCLs have been successfully completed. Data from this series of loop tests indicate that, under similar operating conditions (a 600°C maximum temperature), types 316, 304L, and 321 stainless steel show equivalent weight losses after 3000-h exposures to lithium:

Stainless Steel Type	304L	321	316
Corrosion, g/m^2	−36.1	−30.6	−33.6

Metallographic examination of a type 316 stainless steel tab specimen located near the hottest point (600°C) of the loop revealed a distinct altered near-surface layer [Fig. 8.2.1(a)]. This layer is produced by the selective corrosion of nickel and chromium, as observed by x-ray fluorescence. This process results in a surface enriched in iron such that a ferritic structure can be detected by magnetic susceptibility measurements. Similar layers are formed on types 304L and 321 stainless steel specimens exposed at the same operating conditions[2] [see Fig. 8.2.1(b)].

Recently, a small type 316 stainless steel TCL was put into operation to [illegible] he lithium) [illegible] a 600°C maximum temperature with 500 wt ppm of nitrogen added to the lithium. Additionally, three large type 316 stainless steel loops are presently in operation. The status of the four loops is given in Table 8.2.1. Loops 2 and 3 are being operated under base-line conditions (a 600°C maximum lithium temperature and a ΔT of 150°C) to study corrosion rate as a function of time and to check the reproducibility of data among loops at longer exposures to flowing lithium. After an initial period

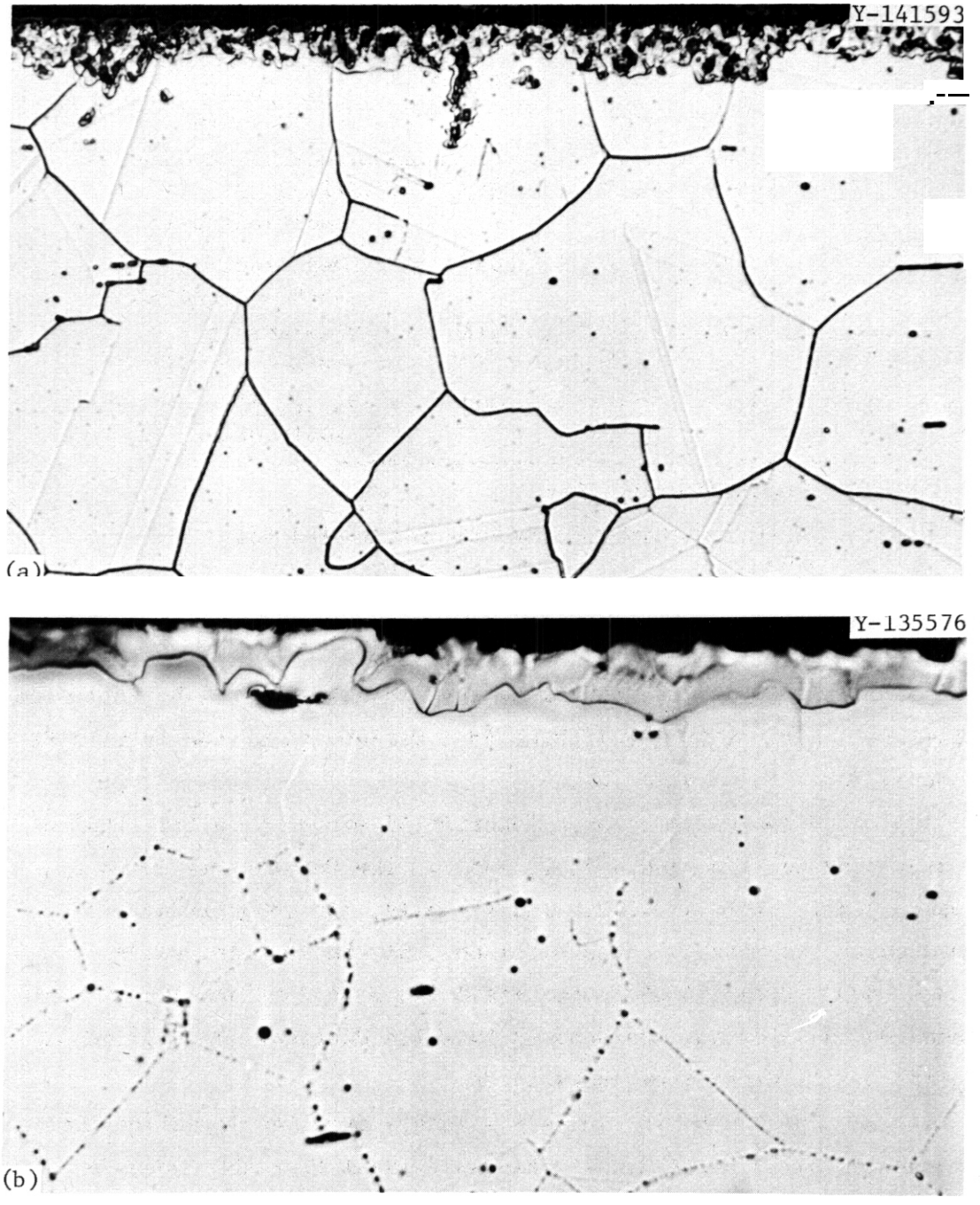

Fig. 8.2.1. Specimens from the Hot Legs of 600° Loops that Operated Uninterrupted for 3000 h. (a) Type 316 stainless steel loop. $HCl-HNO_3$ etch. 500×. (b) Type *304L* stainless steel loop. Magnetic etch. 1000×.

Table 8.2.1. Present Status[a] of Operating Thermal Convection Loops

Loop	T_{max} (°C)	ΔT (°C)	Operating Time (h)	Test Variable
1[b]	600	175	528	Effect of Li_3N addition to Li
2[c]	600	150	5528	Long exposure base-line data
3[c]	600	150	1216	Time effect base-line data
4[c]	600	150	500	Future Al additions to Li

[a] As of May 31, 1978.

[b] Small, uninterrupted loop (scheduled for 3000 h).

[c] Large loops with accessible specimens.

(about another 500 h), loop 4 will be used to investigate the influence of aluminum additions to the lithium as a refinement of the experiment previously done[1] in a small TCL.

Data on corrosion rates as a function of exposure to the lithium have been obtained from loops 2, 3, and 4. The results are shown by the open symbols of Fig. 8.2.2. Additionally, for comparison, maximum corrosion weight losses obtained from the smaller, uninterrupted 600°C type 316 stainless steel loops at 3000 and 10,000 h are included on the plot and are denoted by solid circles. The following summarize the findings from these tests:

1. The reproducibility in weight losses from one large loop to another seems to he quite good. This is evident from the two data points at 500 h in Fig. 8.2.2 (loops 3 and 4). They represent specimens at similar positions in the respective loops, and their weight losses are equivalent.

2. Corrosion rates at 600°C measured in the larger loops are significantly greater than those measured in the smaller loops. We believe that the difference is caused by a slower rate of cooling and

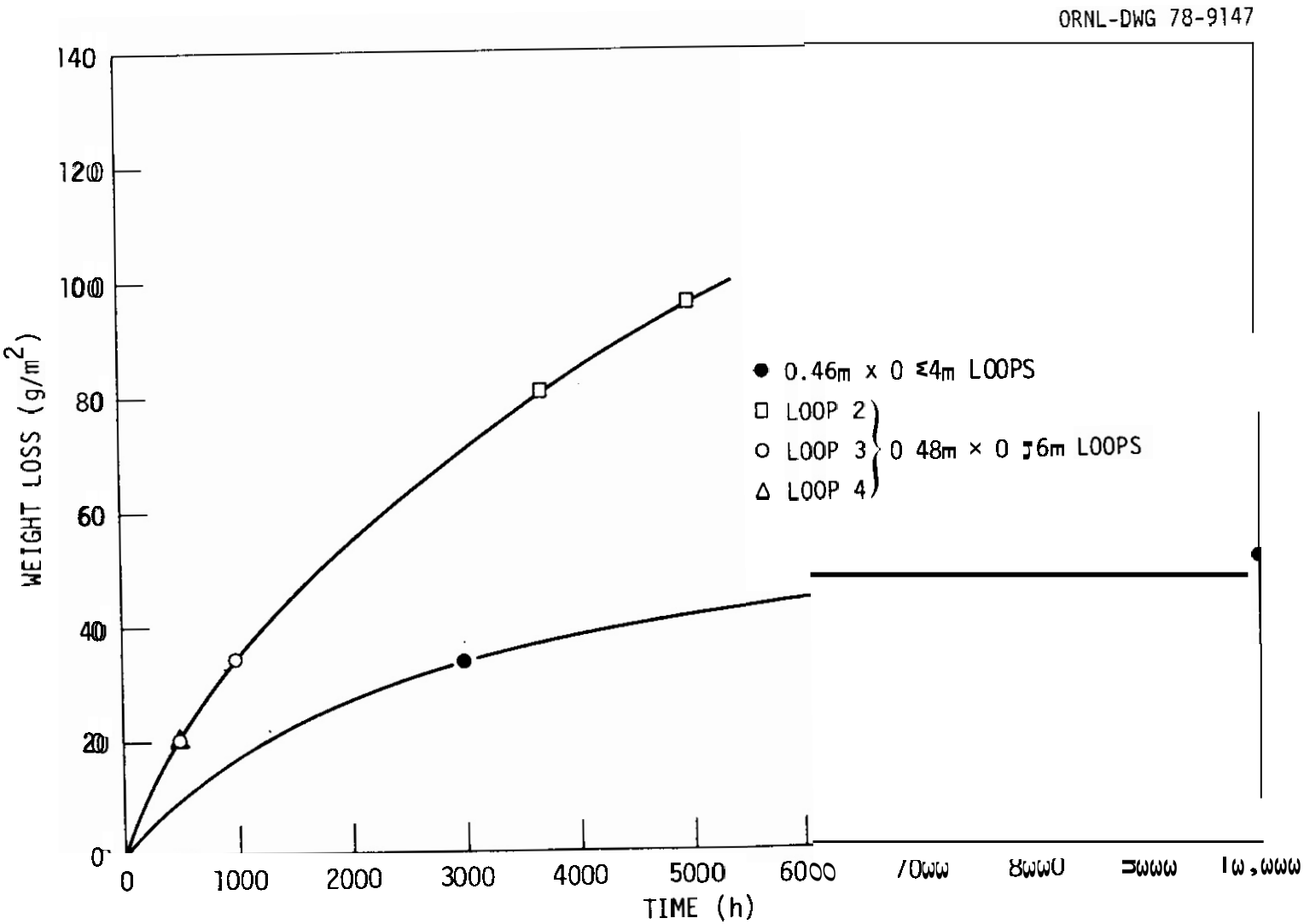

Fig. 8.2.2. Maximum Weight Losses Versus Exposure Time for Type 316 Stainless Steel Thermal Convection Loops. Open symbols represent larger, accessible thermal-convection loops while the solid circles are the results from two smaller uninterrupted loops.

a longer cold leg in the larger loops than in the smaller loops. This slower rate in the cold leg is the result of the somewhat faster lithium velocity in the larger loops (about 30 versus 20 mm/s) and a smaller ΔT (150°C as opposed to 200°C). Because of the reduced rate of cooling and the longer cold leg, a larger relative surface area of metal is available for deposition reactions in the 500 to 550°C range in the larger loop.

3. The corrosion rate in the larger loop appears to be still decreasing with time after 1000 h. Test data beyond 5000 h will be required to establish whether a constant corrosion rate has been reached by 3000 h.

Other TCLs are in either the planning or fabrication stages. Table 8.2.2 is a list of loops that are scheduled to be put into operation within a year.

Table 8.2.2. Planned Loops

Alloy	T_{max} (°C)	Test Variable
Inconel 600[a]	≤500	material
Alloy 718[a]	≤500	material
Alloy 800[a]	600	material
Ti alloy[a]	600	material
316 SS[b]	600	N additions to Li

[a]Small, uninterrupted loops.

[b]Large loop with accessible specimens.

8.2.5 Conclusions

1. Types 316, 304L, and 321 stainless steel show equivalent weight losses after 3000 h exposure to flowing lithium at 600°C.

2. The rate of material loss in the larger loops decreases with time up to several thousand hours.

8.2.6 References

1. J. H. DeVan and J. R. DiStefano, "Thermal Convection Loop Tests of Type 316 Stainless Steel in Lithium," *ADIP Quart. Prog. Rep. March 31, 1978*, DOE/ET-0058/1(78), pp. 200–08.

2. J. E. Selle, "Corrosion of Iron-Base Alloys by Lithium," pp. 453–61 in *Proc. Int. Conf. Liquid Metal Metal Technology in Energy Production, May 3–6, 1976*, CONF-760503-P2, ed. by M. H. Cooper.

8.3 COMPATIBILITY OF BLANKET, COOLANT, AND TRITIUM-PROCESSING SALTS — J. R. Keiser and H. D. Upton (ORNL)

8.3.1 ADIP Task

ADIP Task I.A.3, Perform Chemical and Metallurgical Compatibility Analyses.

8.3.2 Objective

A nitrate-based heat transfer salt (HTS) is a possible coolant for a fusion reactor in which a solid or static liquid breeding blanket is used. The purpose of this work has been to determine the heat released upon mixing HTS with lithium.

8.3.3 Summary

We have reacted controlled amounts of HTS salt (KNO_3-$NaNO_2$-$NaNO_3$, 44-49-7 mol %) with lithium. A rapid, highly exothermic reaction occurred spontaneously on heating a mixture of lithium and salt to about 180°C.

8.3.4 Progress and Status

A nitrate-based heat transfer salt (HTS) (KNO_3-$NaNO_2$-$NaNO_3$, 44-49-7 mol %) is being considered as a possible coolant for a fusion reactor in which a solid or static liquid breeding blanket is used. Since the purpose of the coolant would be to transfer heat from the blanket to a power generating system, the coolant must be liquid or gaseous at operating temperatures and must have good heat transfer capabilities. Other requirements are compatibility with the container material, compatibility with the blanket (in the event of a failure of the container), and adequate stability under neutron irradiation.

Last quarter[1] we discussed our studies of the compatibility of type 316 stainless steel and Hastelloy N with HTS. These studies are continuing, but at higher temperatures than were described previously.

We have recently completed a study of the compatibility of HTS with lithium. The purpose of this srudy was to measure qualitatively

the effect of mixing HTS with lithium, as might occur if the fusion reactor structural member separating the two should develop a leak. The reactions that might occur are:

$$2Li + KNO_3 \rightarrow Li_2O + KNO_2 \ , \qquad (1)$$

$$6Li + 2NaNO_2 \rightarrow 3Li_2O + Na_2O + N_2 , \text{ and} \qquad (2)$$

$$2Li + NaNO_3 \rightarrow Li_2O + NaNO_2 \ . \qquad (3)$$

Another oxide of lithium, Li_2O_2, exists, but its formation is not expected in the presence of Li, $NaNO_2$, or KNO_2. Thermodynamic calculations based on room-temperature heats of formation give the heats of reaction listed in Table 8.3.1. Realizing each of these values has a possible error of about 4 kJ/mol (1 kcal/mol), we see that we cannot choose between reactions (2) and (3) as the more probable.

Table 8.3.1. Heats of Reaction

Eq.	ΔH_{298}	
	(kJ/mol Li)	(kcal/mol Li)
(1)	−237	−56.6
(2)	−247	−59.1
(3)	−244	−58.4

Our experimental measurements consisted of heating 10 g HTS and 0.3 g Li in a vessel for which we could closely monitor the temperature and pressure. The vessel was 38 mm OD and 150 mm high, had thermocouples on the outside and in a center well, had facilities for collecting a gas sample, and had a pressure transducer to measure the gas pressure. The vessel was assembled in an argon-containing glove box to prevent reaction of the lithium with air. The actual experiment was performed by placing the vessel in a furnace and then slowly raising the temperature while monitoring the temperature and pressure.

Two experimental runs were made. The first allowed us to determine if a reaction would occur, and at what temperature and rate if it did occur. We found a rapid exothermic reaction around 200°C. In the more carefully monitored second run, the measured conditions are given in Table 8.3.2. Quite likely the reaction started when the lithium melted and could easily mix with the HTS. Rough calculations of the heat released are in the range of the values of Table 8.3.1. At the same time that the temperature increased, the pressure increased from 0.13 to 0.22 MPa (19 to 32 psi). Subsequent analysis of a gas sample indicated that some nitrogen had been produced, and x-ray analysis of the solid residue in the capsule indicated that Li_2O had also been produced. This should serve as evidence in favor of reaction (2); however, the thermal decomposition reaction

$$5\ NaNO_2 \rightarrow 3\ NaNO_3 + Na_2O + N_2\ , \qquad (4)$$

which is known to occur in HTS at temperatures above 400°C, has to be considered as a possible source of the nitrogen.

The conclusion that can be drawn from this simple study is that molten lithium and HTS undergo a rapid, highly exothermic reaction with production of Li_2O and N_2. No evidence of a reaction between solid lithium and molten HTS was observed.

Table 8.3.2. Measurements During Second Reaction Run[a]

Measurement Location	Temperature, °C		Time to Reach Maximum Temperature (min)
	Reaction Start	Maximum	
Thermocouple well	163	299	<1
Capsule outer surface	177	201	7

[a]HTS melting point 142°C, Li melting point 179°C.

Other molten salt studies now in progress include the operation of a type 316 stainless steel thermal convection loop with the fluoride mixture $LiF-BeF_2$. The loop has completed over 21,000 h at a maximum temperature of 650°C. Another type 316 stainless steel loop has been readied for operation with LiF-LiCl-LiBr tritium-processing salt, which is being supplied by Argonne National Laboratory.

8.3.5 Reference

1. J. H. DeVan and J. R. Keiser, "Compatibility Studies of Type 316 Stainless Steel and Hastelloy N in $KNO_3-NaNO_2-NaNO_3$," *ADIP Quart. Prog. Rep. March 31, 1978*, DOE/ET-0058/1(78), pp. 209–14.

8.4 HYDROGEN PERMEATION CHARACTERISTICS OF PATH A, PATH B, AND PATH C ALLOYS - E. H. Van Deventer and V. A. Maroni (Argonne National Laboratory).

8.4.1 ADIP Task

I.E.1. Hydrogen Dissolution and Permeation Effects. This task was added to the ADIP program plan during the first quarter of FY-1978. The results presented in this section contribute to Subtask I.E.l.l, Milestones I.E.1.a and I.E.1.b. The above title and assigned numbering are tentative, pending approval by the ADIP Task Group.

8.4.2 Objective

The objective of the work described in this section is to provide base-line hydrogen permeation data for Inconel-718 and titanium alloy 5621. In addition, it is expected that the work on the titanium alloy will also yield quantitative information on the hydrogen dissolution and out-gassing characteristics of this class of structural materials. The resulting data will (1) provide a basis for determining the consequences of hydrogen interactions with these representative Path B and Path C alloys under fusion reactor operating conditions and (2) serve as a bench mark in evaluating the effectiveness of permeation barrier methods developed for applications using these materials.

8.4.3 Summary

The hydrogen permeability of a certified sample of Inconel-718 was measured at temperatures in the range 100 to 800°C using hydrogen driving pressures from 10^{-1} to 10^{4} Pa. The results were in excellent agreement with published data collected at hydrogen pressures greater than 10^{5} Pa. Below 13 Pa, evidence of a near-to-first-power dependance on hydrogen pressure was observed, presumably due to the onset of an oxide-film barrier stabilized by the ~0.5 wt % Al present in Inconel-718. Methods of preparing permeation assemblies for titanium-base alloys have been investigated. An approach that appears to be working in preliminary tests involves machining of knife edges into both surfaces of disc-shaped specimens then locking the discs between Varian-

type conflat flanges using a nickel gasket on each side of the specimen. One such assembly has been holding vacuum in the permeation apparatus for ~900 hours at 470°C.

8.4.4 Progress and Status

This section reports the results of extensive hydrogen permeation tests on a certified sample of Inconel-718. Also, a description is presented of the method currently being used to prepare hydrogen permeation assemblies for titanium-base alloys.

8.4.4.1 Hydrogen Permeation Studies on Inconel-718

The hydrogen permeation investigation of Inconel-718 was carried out using the apparatus and procedures described in previous publication~.'-~ Measurements were made in the temperature range from 100 to 800°C using hydrogen driving pressures that ranged from 10^{-1} to 10^{4} Pa. The data obtained in this study for driving pressures greater than 3 Pa are plotted in Fig. 8.4.1 together with the permeability curve reported by Robertson[4] for Inconel-718. Also included in Fig. 8.4.1 is Robertson's permeability curve for pure nickel.[5] The measurements upon which Robertson's curve for Inconel-718 were based, were made using hydrogen driving pressures in the range 10^{5} to 3×10^{5} Pa. The combined results of our work and his are, therefore, in excellent agreement for hydrogen pressures which span the range 3 to 3×10^{5} Pa. Although final refinements to our data remain to be made, a preliminary analysis of our data (as given in Fig. 8.4.1) has yielded the permeation equation

$$\Phi_{\text{Inconel-718}} = 0.059 \exp(-13{,}373/RT) \qquad (1)$$

where Φ is in the units $cm^3(STP)/m \cdot s \cdot kPa^{\frac{1}{2}}$, R is equal to 1.987, and T is the Kelvin temperature. Robertson reports a range of preexponential and activation terms for Inconel-718 which depend on the heat treatment used for selected Inconel-718 specimens in his work. His preexponential and activation terms (in the units used in equation 1) varied from 0.043 to 0.096 and 12,710 to 14,110 respectively. These ranges bracket the values given in equation 1.

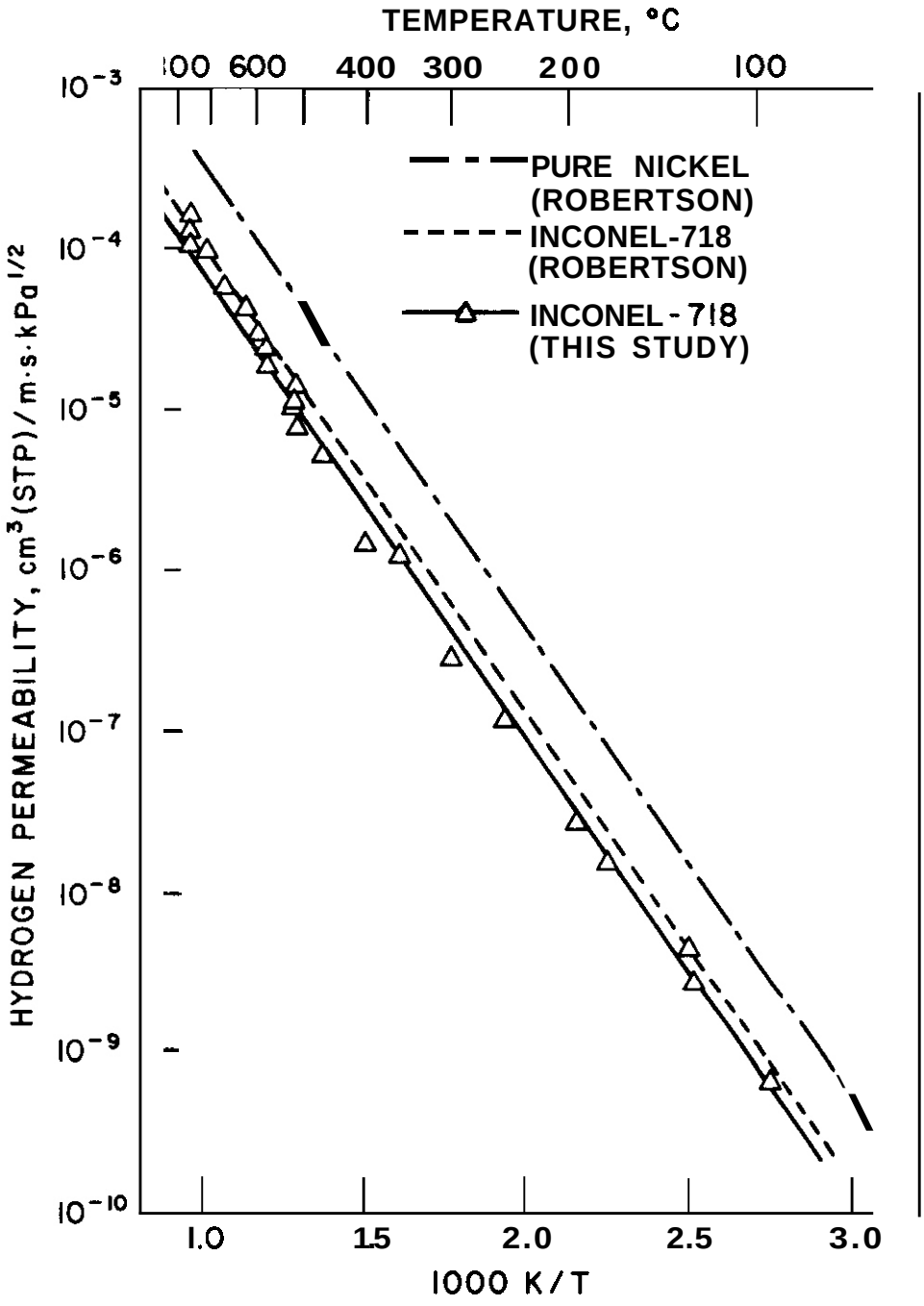

Fig. *8.4.1* Hydrogen permeation data for Inconel–718.

At hydrogen driving pressures below 3 Pa we observed the onset of departures from a square-root-of-pressure dependence in isothermal permeation experiments. In fact, log-log plots of permeation rate *versus* hydrogen pressure yielded slopes closer to 1.0 than to 0.5 for data collected in the 10^{-1} to 3 Pa range. This positive evidence of an oxide-film-limited region[6] below ~3 Pa (under our experimental conditions) is most probably the result of surface oxide scales that are stabilized by the aluminum (~0.5 wt %) present in Inconel-718. Microscopic and microprobe analyses of the studied Inconel-718 specimen (to characterize the surface and bulk microstructure) are underway and will be reported on in a subsequent progress statement.

8.4.4.2 Hydrogen Interactions with Titanium-Base Alloys

In the face of current interest' in titanium-base alloys as fusion reactor construction materials, we have initiated a series of studies with selected titanium alloy compositions to determine their hydrogen uptake, diffusion, and permeation characteristics. Early efforts are focusing on the *64 (6%* Al, *4%* V) and *5621* (5% Al, *6%* Sn, 2% Zr, 1% Mo) alloys. The preparation of a reliable permeation assembly compatible with our permeation apparatus has proven not to be a straightforward matter. The method that has been successfully used in all prior studies (which include stainless steels, nickel-base alloys, vanadium, niobium, copper, and rhenium) involves electron beam welding of a thin disc of the sample material between two stainless steel couplings.' This method did not work with either the *64* or *5621* alloys in that a ductile weld could not be formed. Subsequent correspondence with J. A. Davis at McDonnell Douglas (MDAC) confirmed that a ductile weld of titanium alloy to stainless steel would be difficult if not impossible to achieve. The idea of making the couplings out of a niobium or vanadium alloy (to test a SS/Nb/Ti or SS/V/Ti weld configuration) was considered, but it was reasoned that these strong hydride forming alloys (Nb or V) would complicate the attainment of stable hydrogen pressures in the upstream and downstream compartments of the permeation apparatus. An attempt to seal a *64* alloy specimen between two

Varian conflat flanges was expectedly unsuccessful.

A method which appears to be working at the time of writing involves machining knife edges into both sides of the titanium alloy disc and then locking the disc between two 2-3/4-inch-diameter Varian conflat flanges using a nickel gasket on each side of the disc. In this configuration, four knife edge seals are made simultaneously. Accordingly, knife edges were machined into a 60-mil sample of the 5621 alloy (supplied by J. A. Davis, MDAC) and an assembly was constructed. This assembly has held vacuum in the hydrogen permeation apparatus for ~900 hours at 470°C. Out-gassing of the sample is progressing but at a slower than normal rate, due in part to the hydrogen already in the titanium and the other coupling hardware and in part to the fact that 470°C is a lower temperature than is normally used to out-gas all-welded assemblies (*i.e.*, ~800°C).

d.4.5 Conclusions

Hydrogen permeation through Inconel-718 is controlled by bulk diffusion in hydrogen environments typical of those expected for fusion plasma chambers (*i.e.*, >98% hydrogen). Some sensitivity of permeation rate to impurities in the gas phase is observed at low pressures (<3 Pa in our studies), and this is tentatively attributed to surface-oxide films involving the ~0.5 wt % aluminum present in Inconel-718. A method of fabricating permeation assemblies. which involves the preparation of machined knife edges on the specimen surfaces and the use of nickel gaskets, appears to be suitable for the study of titanium alloys.

8.4.6 References

1. E. H. Van Deventer, "Hydrogen Permeability of Raynes Alloy-188," *J. Nucl. Mater.* 66(3): 325-328 (1977).
2. E. H. Van Deventer, T. A. Renner, R. H. Pelto, and V. A. Maroni, "Effects of Surface Impurity Layers on the Hydrogen Permeability of Vanadium," *J. Nucl. Mater.* 64(3): 241-248 (1977).
3. V. A. Maroni and E. H. Van Deventer, *Hydrogen Permeation of Type-316 Stainless Steel,* Alloy Development for Irradiation Performance

Progress Report for the Period Ending March 31, 1978, U. S. Department of Energy Report DOE/ET-0058/1(78), p. 215.

4. W. M. Robertson, "Hydrogen Permeation and Diffusion in Inconel 718 and Incoloy 903," *Metall. Trans.* 8A(11): 1709-1712 (1977).
5. W. M. Robertson, "Hydrogen Permeation, Diffusion, and Solution in Nickel," *Zeit. Metallkunde* 64: 436-443 (1973).
6. R. A. Strehlow and H. C. Savage, "The Permeation of Hydrogen Isotopes Through Structural Metals at Low Pressures and Through Metals With Oxide Film Barriers," *Nucl. Technot.* 22: 127-137 (1974).
7. J. A. Davis and G. L. Kulcinski, *Assessment of Titanium For Use in the First Wall/Blanket Structure of Fusion Power Reactors,* Electric Power Research Institute, EPRI ER-386, 1977. See also: J. A. Davis, *Selection of Titanium Alloys for the Path C Scoping Studies,* Alloy Development for Irradiation Performance Progress Report for the Period Ending March 31, 1978, U. S. Department of Energy Report DOE/ET-0058/1(78), p. 109.

*U.S. GOVERNMENT PRINTING OFFICE : 1979 0-281-704/45